ESTIMATION OF BURIAL TEMPERATURE IN THE LOMA DE LAS CAÑAS REGION EAST OF SOCORRO, NEW MEXICO, BY X-RAY DIFFRACTION

By

Frank Marshall Craig, Jr.

Report submitted to Jacques Renault in fullfillment of the requirements for an directed study

New Mexico Institute of Mining and Technology

Socorro, New Mexico

November, 1991

ABSTRACT

Pennsylvanian cherts from the Loma de las Cañas region were analyzed using silica crystallite geothermometry to determine burial temperatures. Although this is a structurally complex area, and this complexity most likely has affected the temperatures, the data are consistent with the idea of an increase in temperature with depth. This data, when combined with a burial depth of 5812 m, produces a geothermal gradient of 34 °C/km ([212] data) and 47 °C/km ([104] data), which is higher than the commonly cited 25 °C/km for a stable craton. Of course, this area is far from stable and this is probably being reflected in these gradients.

ACKNOWLEDGEMENTS

I would like to thank Dr. Jacques Renault for sparking an interest in the subject of x-ray diffraction and for providing financial support through the New Mexico Bureau of Mines and Mineral Resources. Many helpfull insights regarding the subject of the substructure of crystals has been gained through numerous discussions with Jacques Renault. Also, many long discussions with Jacques Renault and Gus Armstrong concerning the diagenesis of microcrystalline silica have improved the quality of this report and are greatly appreciated by the author.

I would like to thank Drs. Bob Carnein and Jaques Renault for critically reviewing the manuscript. Their suggestions regarding grammer and context have immensely improved the readability of this report as well as clarifing theories and conclusions presented.

I would like to thank Chris McKee, of the New Mexico Bureau of Mines and Mineral Resources X-ray Lab, for instruction in the use of the Rigaku X-ray Diffractometer and related computer software. Also, Ed Fry helped in supplying a couple references on the Permian Basin

Last, but certainly not least, I'd like to thank my parents, Frank and Jean Craig, without whose moral and financial support this study would not have been possible.

Table of Contents

List of Figures

List of Tables

INTRODUCTION

The Loma de las Cañas region is located along the east side of the Rio Grande rift within the Socorro constriction (Fig. 1) – a narrow link between the wider expressions of the rift, the Albuquerque-Belen Basin to the north and the San Marcial Basin to the south (Smith, 1983). While the Socorro constriction is considered to be part of the rift (Kelley, 1982), some of the stuctures exposed within this region are older than the rift and do not represent crustal extension. Detailed mapping by Rejas (1965), Maulsby (1981), Bauch (1982), Fagrelius (1982), Colpitts (1986), Linden (1990), Cabezas (1991), Smith et. al. (1991) and preliminary work by the writer has documented the presence of open, upright to tightly, overturned folds as well as thrust and décollement structures (low-angle normal faults). The existence of thrust and décollement structures was first suggested by C. T. Smith in the early 1960's (Smith, personal commun., 1990) and later confirmed by Maulsby (1981), Bauch (1982) and Fagrelius (1982). The presence of such structures (not neccessarily the décollements. the origin of which is still debated) suggests a shortening event prior to the onset of rift extension. This event most likely relates to the Laramide orogeny; however, some of the tight, overturned folds are believed to result from an event that occurred during the Early to late Middle Triassic (Smith, personal comm., 1990).

The origin of the décollement structures has not been well established; suggestions include: thrusting, gravity slides or thrust surfaces reactivated as gravity slides. Linden (1990) has presented a mechanical model, supported by available field evidence, which utilizes gravity as a mechanism of emplacement. Aquisition of the gravitational potential energy resulted from either (1) vertical movement associated with transpression in the vicinity of the Montosa fault zone (Fig. 2), or (2) the development of a northeast-trending anticline located just south of the area (Linden, 1990; p. 30). Colpitts (1986) also considered a gravity mechanism as the mode of emplacement by providing an explanation through the application of Kehle's (1970) mechanical model in his field area. Based on available field evidence, emplacement

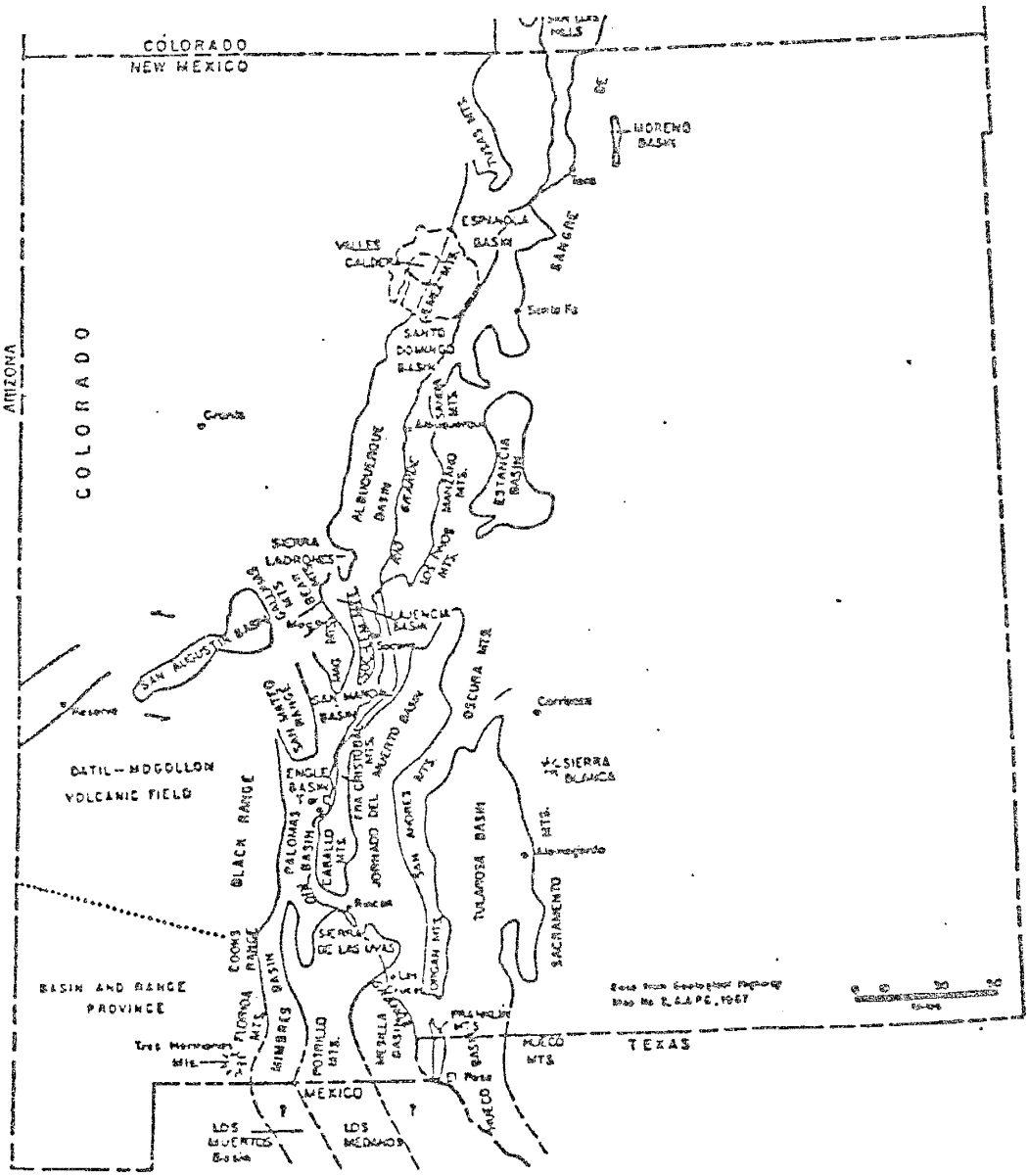

Figure 1. Generalized map of the Rio Grande rift in New Mexico (after Chapin, 1971)

and deformation probably occurred during the early Laramide (Late Cretaceous to Late Paleocene; Colpitts, 1986, p. 69). Linden (1990, p. 81) was able to further constrain the deformation to the Paleocene Epoch.

The application of mechanical models in explaining the deformation of rock requires knowledge of the prevailing temperature/pressure conditions at the time of deformation. The lithostatic pressure can be calculated from density data obtained from wireline logs of units confining the deformation (Colpitts, 1986) or from estimates of density based on lithology and by use of the equation:

$$\sigma_v = \rho g z, \tag{1}$$

where ρ is the density of the overburden, g is the acceleration due to gravity and z is the depth. Using this method, Colpitts (1986) calculated a confining pressure of 24 MPa. Whereas, Linden (1990, p. 40) calculated a confinning pressure of 25 MPa, however he does not mention how overburden density was obtained. The usual procedure for estimating temperature is to assume a geothermal gradient equal or similar to the present day average. In tectonically active regions the present geothermal gradient could be much higher than that in the past. For the Socorro region Colpitts (1986, p. 75) assumed a pre-rift gradient of 34.5 to 39.1 °C/km; Linden (1990, p. 40) assumed a pre-rift gradient of 30 °C/km. Neither Colpitts nor Linden specified the basis for choosing these gradients, although Colpitts (1986) assumed "a normal geothermal gradient". Oddly enough, the area in which Linden (1990) did his mechanical analysis includes Colpitts' (1986) study area (Fig. 2). Because of the uncertainties involved in estimating geothermal gradients, the primary purpose of this study will be to utilize silica crystallite geothermometry – a method developed by Renault (1980) to aid in petroleum exploration – to provide a quantitative basis on which to estimate a geothermal gradient or at least to provide a constraint on the temperature at the level of deformation.

The application of silica-recrystallization to paleo-temperature determination requires that the starting material have a very small crystallite size, the chemical composition is

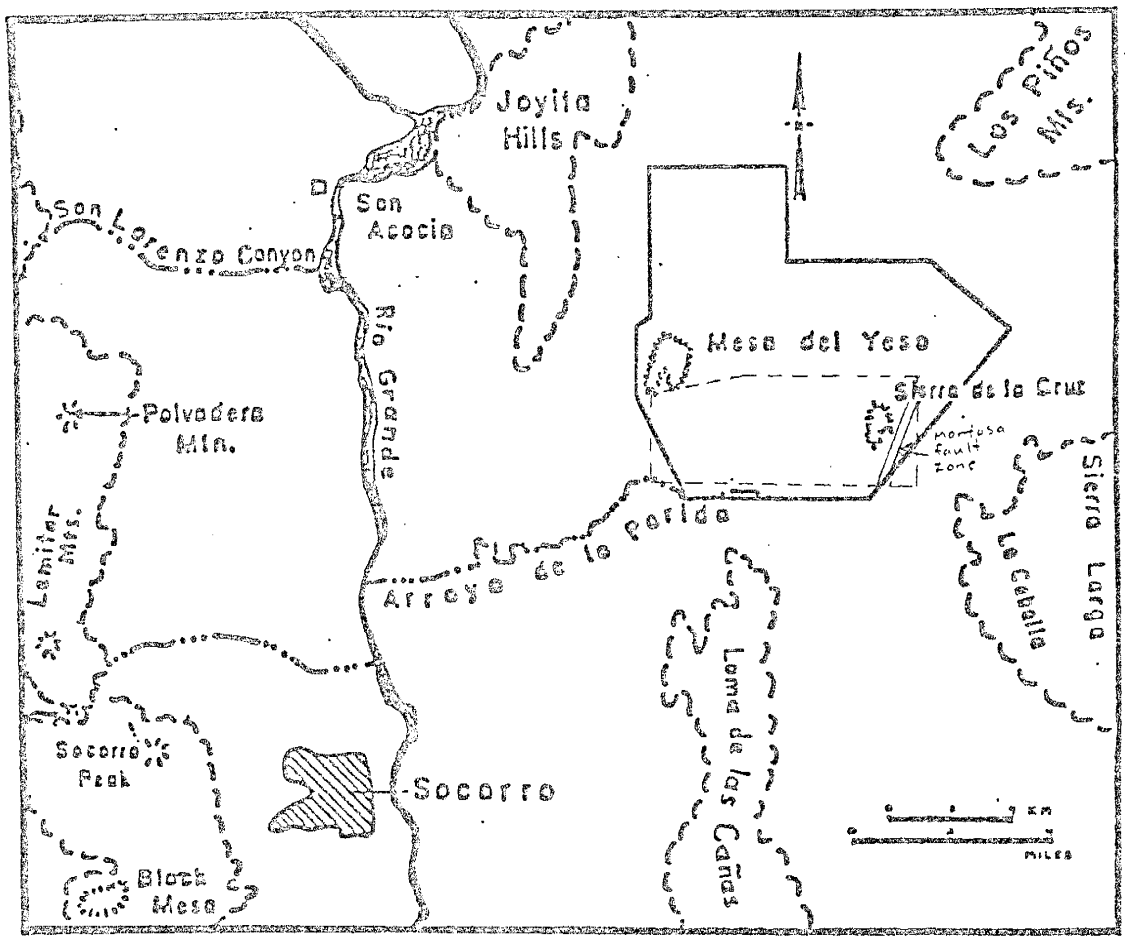

Figure 2. Generalized map of the Socorro region showing the location of Linden's (1990) field area (solid outline), Colpitts' (1986) field area (dashed outline), and the Montosa Fault Zone (modified from Linden, 1990).

uniform, and that heating times be long enough to obtain equilibrium; such conditions are easily met by sedimentary chert (Renault, 1980). Ideally, if a chert originates as a siliceous ooze or mud, or forms by replacement during early diagenesis and has not been affected by secondary recrystallization, it should record the maximum burial temperature. Given an estimate of the amount of overburden a geothermal gradient can be established for the section. This, in turn, would provide an accurate estimate of the prevailing temperature conditions at the time of deformation. If chert meeting the above specifications can be found above and below the level of deformation, then the two temperatures can be used to constrain the temperature at the level of deformation. Because the origin and history of the chert are important, the secondary purpose of this study will be to examine the chert in thin section and in the field to determine the possible origin.

The silica crystallite geothermometry method assumes that growth of the chert began as a silica gel or opaline silica. Local thermal effects such as the circulation of hydrothermal solutions, shearing and exothermic reactions can complicate the interpretation of the data. In addition, the opening of the Rio Grande rift has had a profound effect on heat flow in central New Mexico. Upwelling of asthenospheric mantle has significantly modified the geothermal gradient. For example, heat flows in the Jornada del Muerto basin (see Fig. 1) range from 90 mW m^{-2} in the northern part of the basin to approximately 125 mW m^{-2} in the southern part (Reiter and Barroll, 1990). High heat flows are typical of tectonically active regions (Reiter and Barroll, 1990; Barroll and Reiter, 1990) and can be explained by either crustal thinning (the present crustal thickness under the Jornada del Muerto Basin is about 31 km compared to approximately 50 km under geologically stable regions (Reiter and Barroll, 1990)) or massive intrusions at the base of the crust (a magma body exists at a depth of about 20 km and 5 km under Socorro, which would explain the high heat flows measured by Barroll and Reiter (1990) in the area). In order to appraise this effect in the rift, two samples from a drill core outside the rift (in the Permian Basin) will be analyzed.

CHAPTER 1: X-ray Diffraction Technique

Introduction

X-rays are a type of electromagnentic radiation produced in an x-ray tube (Fig. 3) when electrons, accelerated by a voltage, strike a metal target (Cullity, 1978). The x-rays produced consist of a mixture of different wavlengths whose intensities depend upon the tube voltage. This type of radiation is usually referred to as polychromatic, continuous, or white radiation because it is made up of many wavelengths. When the voltage across the x-ray tube is raised above a certain critical value, characteristic of the target metal ($\frac{12.4}{\lambda}$ kV) , sharp intensity maxima appear at certain wavelengths, superimposed on the continuous spectrum (Fig. 4) (Cullity, 1978). This type of radiation is referred to as the characteristic spectrum because the wavelengths are characteristic of the target metal ($\lambda = 1.5425$ Å for Cu$K\alpha$).

Upon entering a crystal, x-rays are scattered in all directions by the atoms of the crystal (Fig. 5a). In a perfect crystal there are certain directions in which the scattered rays are completely in phase and reinforce one another (constructive interference). In all other directions the rays will be out of phase and thus cancel each other (destructive interference). The reinforcement of rays produces a strong beam known as the diffracted beam (Fig. 5b). The directions within the crystal at which diffraction occurs is governed by the Bragg law:

$$\lambda = 2d \sin\theta \quad , \tag{2}$$

where λ is the wavelength of incident radiation, θ is the angle of incident radiation, and d is the spacing between lattice planes.

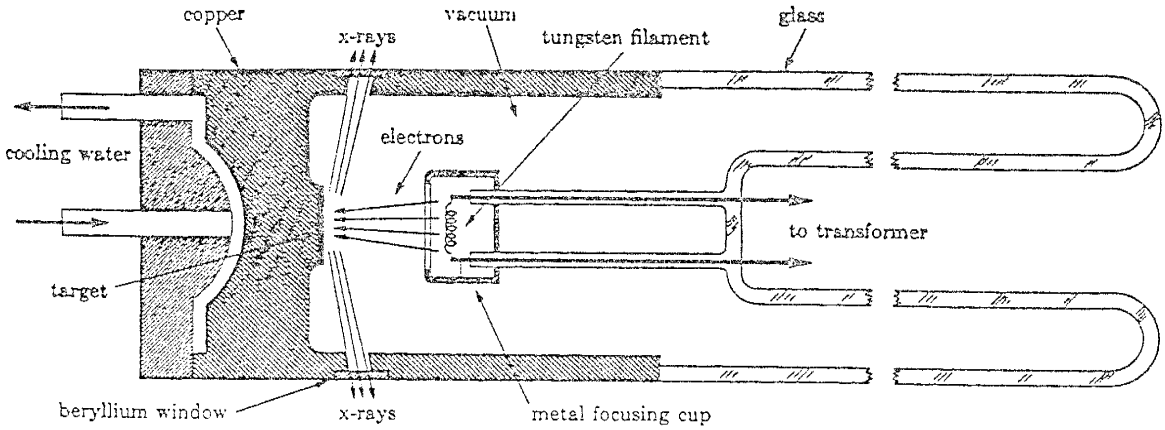

Figure 3. Diagram of an X-ray tube (from Cullity, 1978).

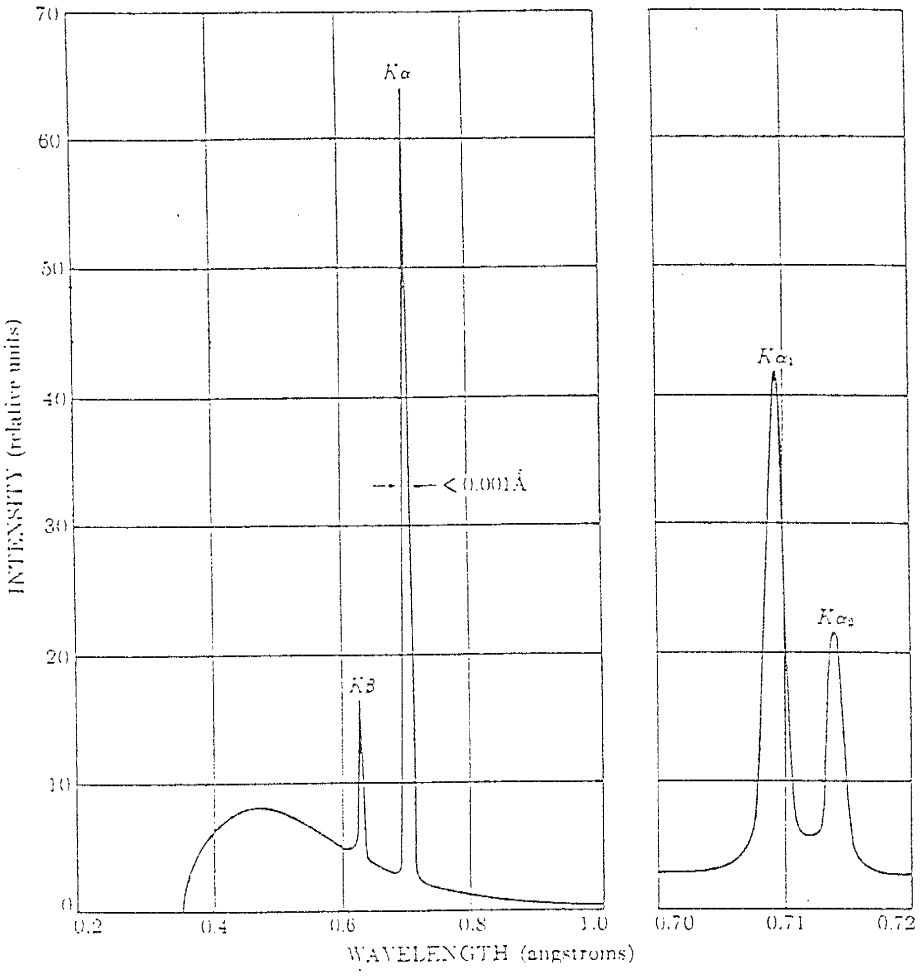

Figure 4. Spectrum of Mo at 35 kV showing continuous and characteristic radiation. Not to scale (after Cullity, 1978).

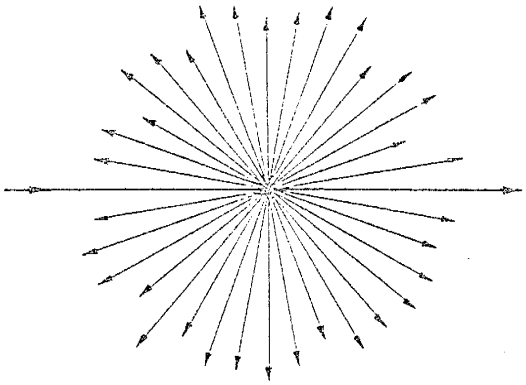

(a)

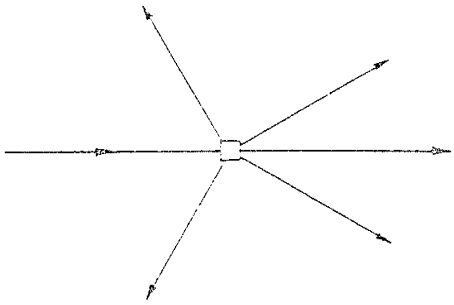

(b)

Figure 5. (a) Scattering by an atom. (b) Diffraction by a crystal (after Cullity, 1978).

Theory

Most naturally occurring crystals are imperfect and consist of what has been called a mosaic (Cullity, 1978; Renault, 1980) or crystallite (see Renault, 1980; Klug and Alexander, 1974) structure. The atoms in such a crystal are not arranged in a perfectly regular lattice extending from one side of the crystal to the other; instead, the lattice is broken up into a number of domains, each slightly misoriented with respect to the others (Fig. 6). Individual domains have dimensions that range in size up to several thousand angstroms (1Å = 10^{-8} cm), while the maximum angle of disorientation (Cullity, 1978) between them may vary from a very small value to as much as one degree, depending on the crystal. The effect of the mosaic structure is to broaden the diffraction profile. This broadening component (pure diffraction broadening) is separated from components resulting from mechanical aspects of the diffractometer (see Klug and Alexander, 1974) by x-ray line deconvolution methods (see Renault, 1980). Pure diffraction broadening increases both with decreasing crystallite size and increasing internal strain (Renault, 1980). Because most micro-crystalline quartz samples have little natural of artificially induced internal strain (Klug and Alexander, 1974; J. Renault, personal communication, 1991) its observed pure diffraction broadening is attributable almost wholly to the size of the individual domains. Domain size can be calculated from the Scherrer formula (Klug and Alexander, 1974):

$$D = \frac{K\lambda}{\beta \cos\theta} \quad , \tag{3}$$

where D is the size of the domain, K is a constant which can be taken as unity in this application, λ is the wavelength of x-radiation, θ is the Bragg angle, and β is the pure diffraction line broadening.

Prior to the availability of the electron microscope, the idea of the mosaic structure within crystals was based on indirect evidence from theoretical and experimental work (Cullity, 1978). The electron microscope showed that single crystals, or individual grains in a

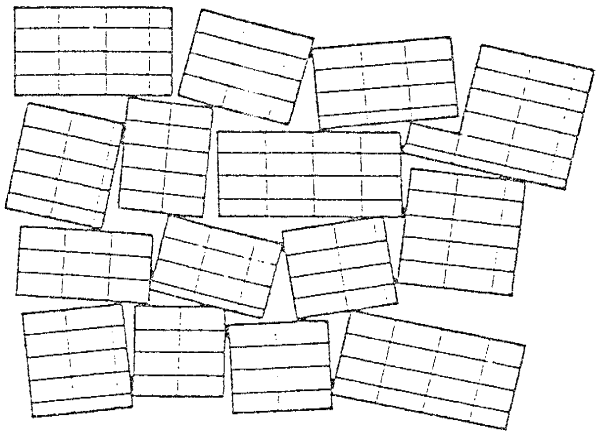

Figure 6. The Mosaic structure of a real crystal (after Cullity, 1978).

polycrystalline aggregate, have substructures defined by the dislocations present (Fig. 7). The density of these dislocations is not uniform; they tend to group themselves into walls surrounding small volumes having a low dislocation density (*domains*). In this respect the growth of a domain can be compared with the growth of discrete subgrains. However, growth of a domain progresses by the healing of dislocations and the alignment of adjacent lattice planes. Growth is driven by processes that seek to minimize surface free energy and that are strongly temperature dependent; as temperature increases, domain size increases (Renault, 1980). As applied to chert, this variation in domain size with temperature is called the "silica crystallite geothermometer" (Renault, 1980). Calibration data has been determined for both the (212) and (104) peaks for sedimentary chert (Tables 1 & 2). The data from both sets have been plotted on Arrehenius diagrams (Fig. 8 & 9) from which the equations for temperature can be obtained by regression analysis:

$$T_{[212]} = \frac{2832}{12.33 - \ln D} - 273 \quad , \tag{4}$$

$$T_{[104]} = \frac{2231}{10.5 - \ln D} - 273 \quad , \tag{5}$$

where T is the temperature and D is the size of the domain (crystallite size). Calibration data obtained from the (212) peak gives a correlation factor of 0.96, while that from the (104) peak gives a correlation factor of 0.98. Since the accuracy of the geothermometer is dependent on the best fit of the calibration data, both equations will give valid temperature determinations. However, because of the shallow slope of the [104] calibration curve, temperature varies too much with very small crystallite size for the sensitivity to be good.

Table 1. Calibration data for the sedimentary (104) peak for the silica crystallite geothermometer (after Renault, unpub.).

Temperature Method	T (°C)	D (Å)	Temperature Reference
Metamorphic Equilib.	450 410	1278 1268	Budding and Broadhead (1977)
Metamorphic Equilib.	425 350	1272 1272	Keller, et. al. (1985)
Metamorphic Equilib.	425 350	1125 1125	Hoersch (1981)
H′ carbon Maturation	290 250	877 715	Ewing and Thompson (1977)
Opal-CT Heating	125 125	106 142	Renault (unpub.)
Opal-CT oxy Isotope	35 40	20 50	Hein, et. al. (1978)

Table 2. Calibration data for the sedimentary (212) peak for the silica crystallite geothermometer (after Renualt, unpub.).

Temperature method	T(°C)	D (Å)	Source
Metamorphic Equilib.	410 450	6383 7013	Budding and Broadhead (1977)
Metamorphic Equilib.	350 425	3106 3106	Keller, et al. (1985)
Metamorphic Equilib.	350 425	1844 1844	Hoersch (1981)
CAI	300 350	1327 3199	Renault (unpub.)
H′ carbon Maturation	250 290	932 1129	Ewing & Thompson (1977)
Fluid Inclusion	235 285	926 1360	Iovenitti (1977)
CAI	190 300	759 886	Renault (unpub.)
Opal-CT heating	125 125	106 142	Renault (unpub)
Opal-CT oxy Isotope	35 40	20 50	Hein et. al. (1978)

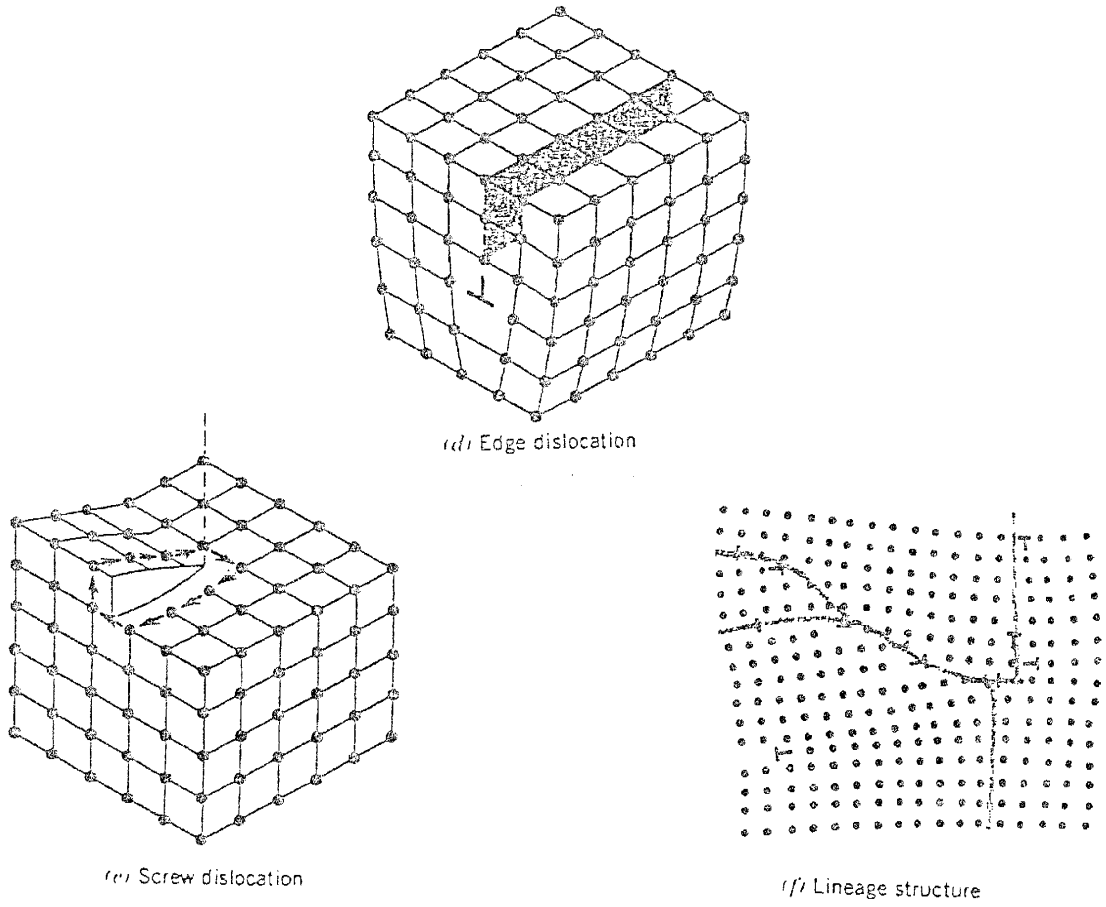

Figure 7. Diagram of the types of dislocations present in a crystal (from Klein and Hurlbut, 1985).

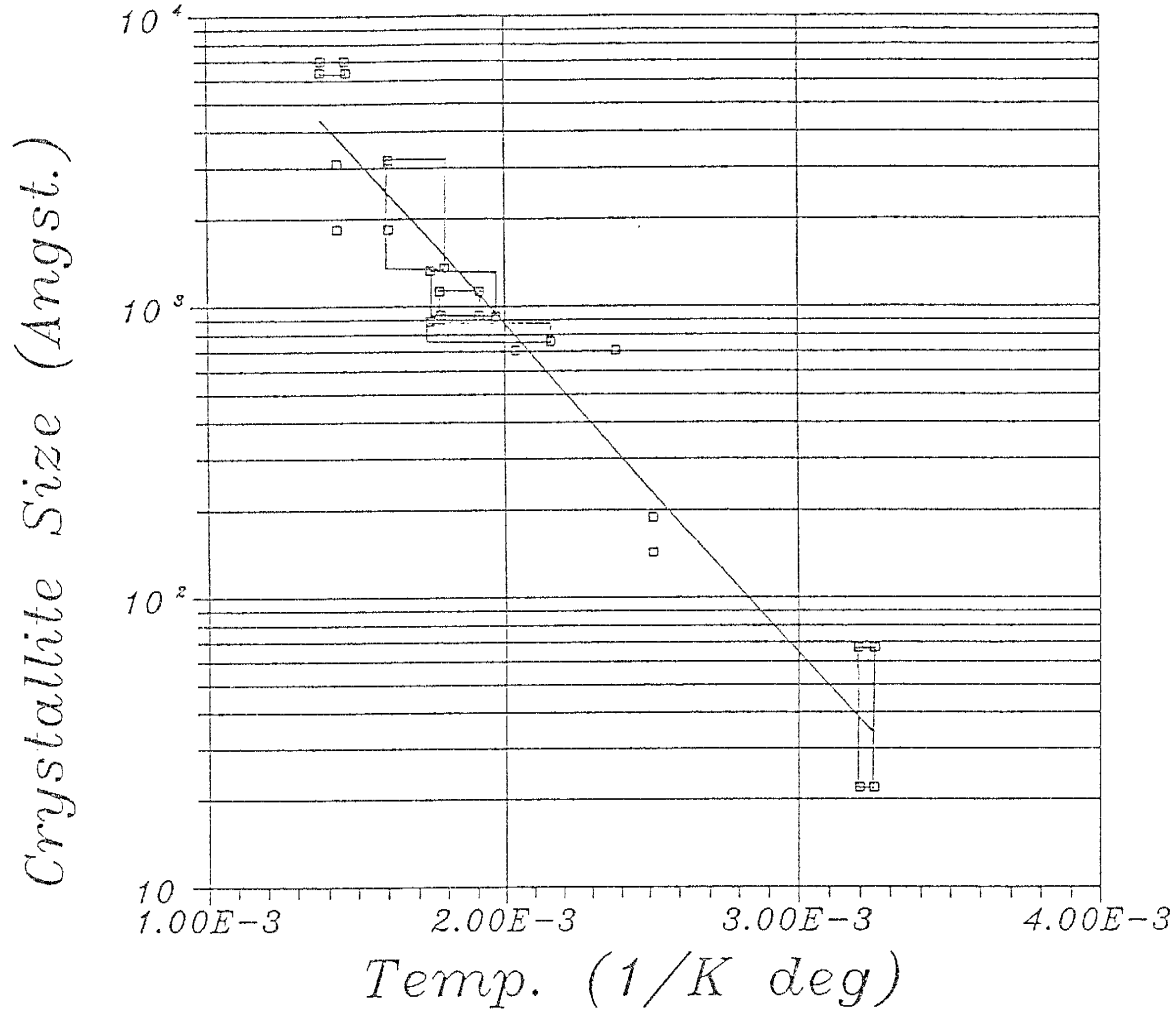

Figure 8. Variation of the (212) silica crystallite size with temperature (after Renault, unpub.).

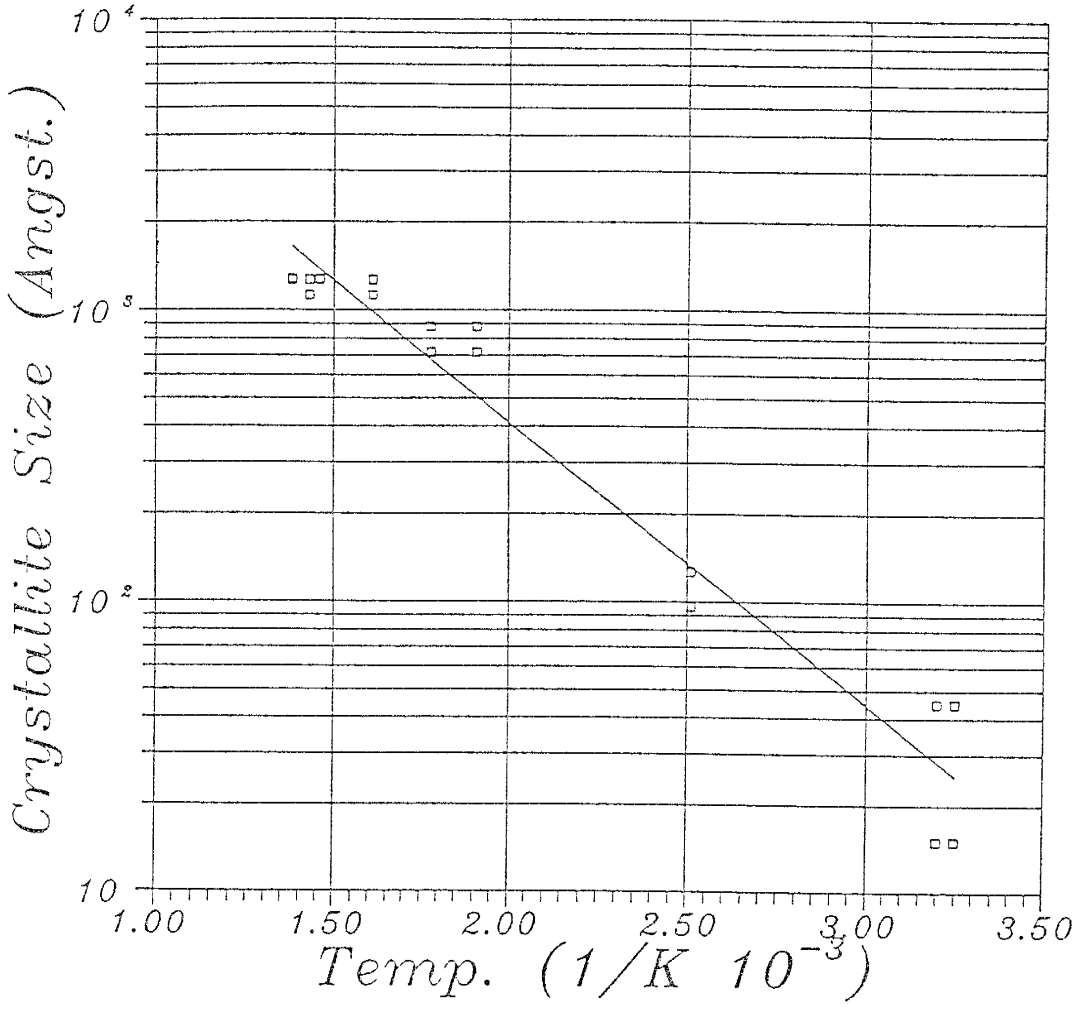

Figure 9. Variation of (104) silica crystallite size with temperature (after Renault, unpub.)

Diffraction Method

With monochromatic radiation, an arbitrary setting of a single crystal in a beam of x-rays will not in general produce any diffracted beams; the Bragg law puts very stringent conditions on λ and θ for any crystal (Cullity, 1978). Thus, in order for diffraction to occur either λ or θ must be varied during the experiment. The three major methods which accomplish this (Cullity, 1978) are the Laue, rotating crystal, and powder methods (Table 3). The New Mexico Bureau of Mines and Mineral Resources x-ray lab employs a Rigaku Diffractometer (Fig. 10), which analyzes powdered samples [powder diffraction]. For this reason (and also to save time and space), only the powder method will be discussed.

Table 3. Diffraction methods (after Cullity, 1978).

Method	λ	θ
Laue method	Variable	Fixed
Rotating-crystal method	Fixed	variable (in part)
Powder method	Fixed	Variable

In the powder method, the sample is ground to a fine powder ($15\mu m$ to $60\mu m$; Renault, 1980) and placed in a beam of x-radiation. Each particle of sample in the powder acts like a tiny crystal, or assemblage of smaller crystals, oriented at random with respect to the incident beam. Just by chance, some of the crystals will be correctly oriented so that their (100) planes, for example, can reflect the incident beam. Other crystals will be correctly oriented for (110) reflections, and so on. The result is that every set of lattice planes within the crystal as a whole is capable of reflecting the incident beam. If a fine powder is not used or the sample is unevenly ground, then the sample presented to the x-ray beam will contain a mixture of grain sizes (Fig. 11a). The larger grains will have fewer different planes with orientations that satisfy the Bragg law, but reflections from the favorably oriented planes will have disproportionately high intensities. (Fig. 11b). In figure 11b, the intensities of the

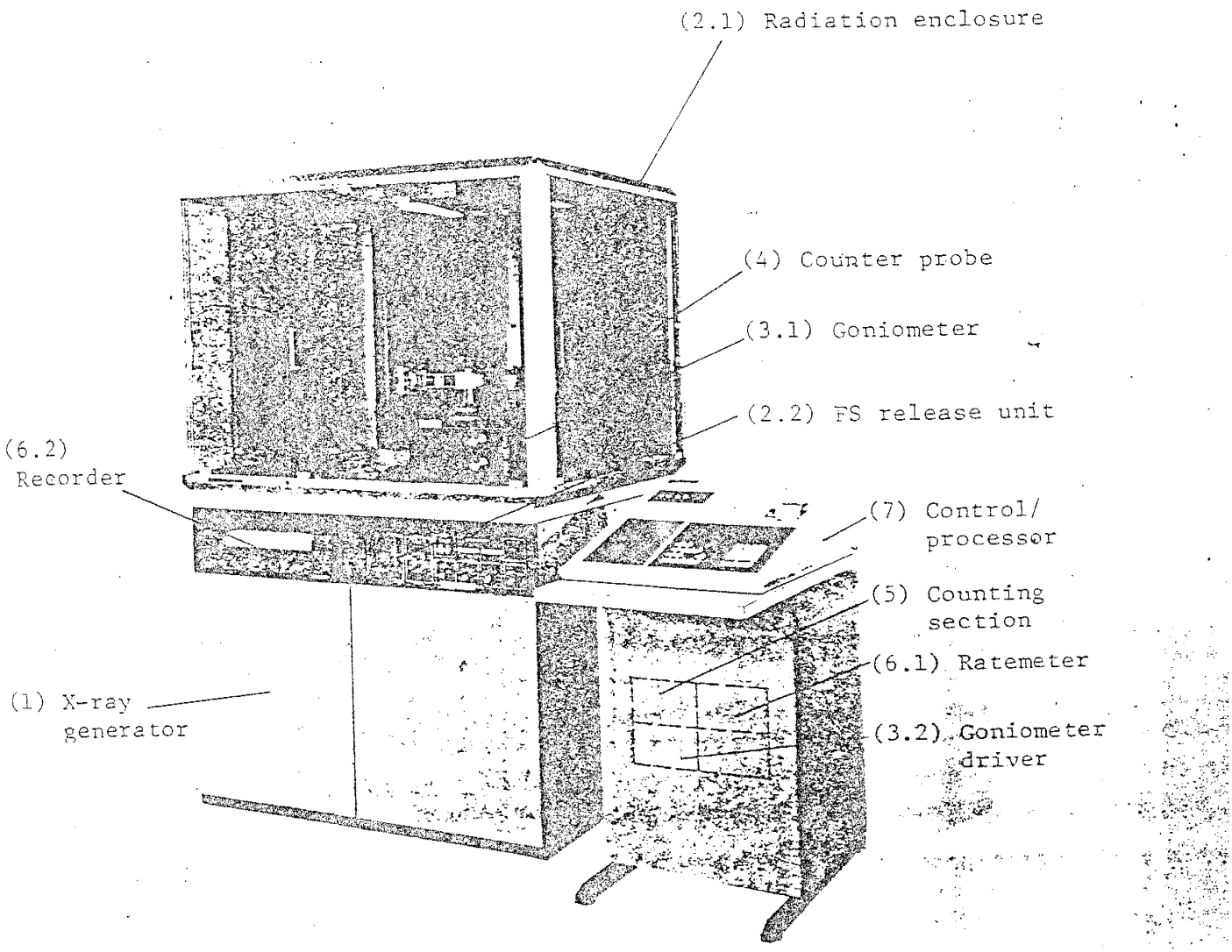

Figure 10. Photograph of Rigaku Diffractometer.

a

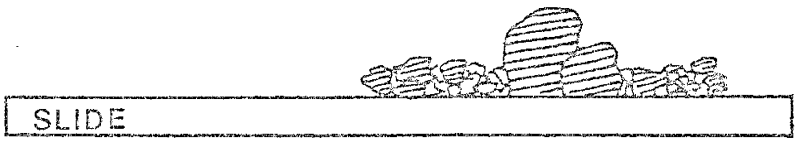

b

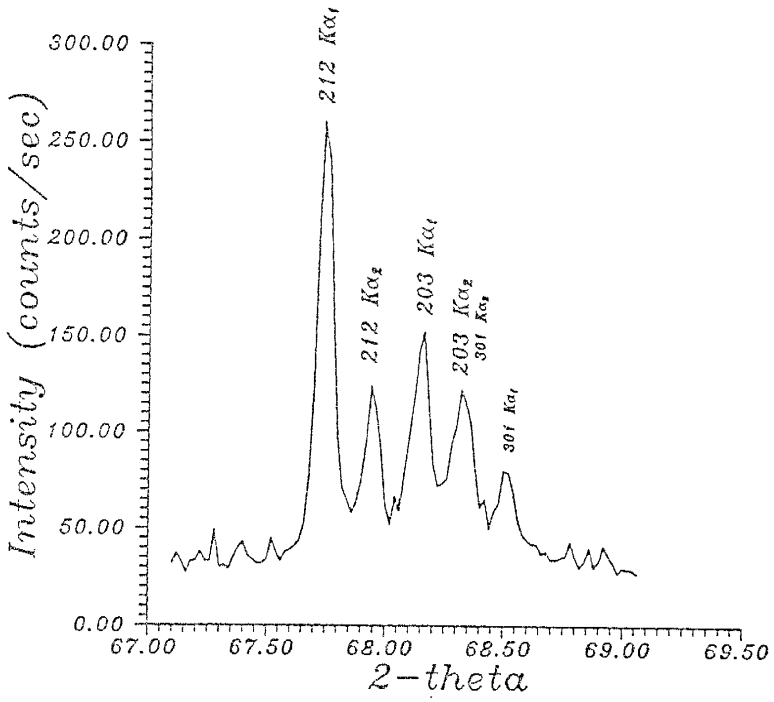

Figure 11. (a) Mounted sample containing a mixture of grain sizes (exaggerated). (b) Diffractogram of a (212) reflection showing an increase in the intensity of the 212 Kα. Other peaks show normal intensities.

212 $K\alpha_1$ and $K\alpha_2$ peaks are increased relative to the 203 peaks (compare with Fig. 13). The 212/203 intensity ratio will be increased, thus decreasing the observed broadening (Fig. 14) and decreasing the crystallite size. In many cases, the broadening cannot be determined because the 212/203 intensity ratio is beyond the range given in figure 14. It is especially important that the standard be a uniform fine powder because it is used to eliminate the broadening resulting from the mechanical aspects of the diffractometer. If standard intensities are suspect they should be compared with known intensities (or previous run standards known to be correct).

Sample Preparation

The procedure for preparing samples for x-ray diffraction is outlined below.

[1] 6.4 mm thick slabs, cut from chert specimens, are analyzed under a binocular microscope for areas containing no secondary quartz growth or contamination from other minerals and marked (3 to 6 are sufficient).

[2] Marked areas are cored using an ultrasonic disk cutter (Fig. 12). The micro cores (3 mm in diameter) are then crushed in a porcelain morter (optional: submerged in acetone to prevent pieces from flying out).

[3] The chert is then leached in 10% hydrochloric acid to remove any calcite (the most common contaminant). After any reaction is complete the hydrochloric acid is discarded and the sample washed in acetone.

[4] Grains which are not contaminated and do not show secondary recrystallization are selected (with the aid of a binocular microscope) for x-ray diffraction.

[5] The sample chosen for x-ray diffraction is ground to a fine powder and mounted on a glass slide which fits into the diffractometer sample holder. Scotch 3M 9500 Pc high performance

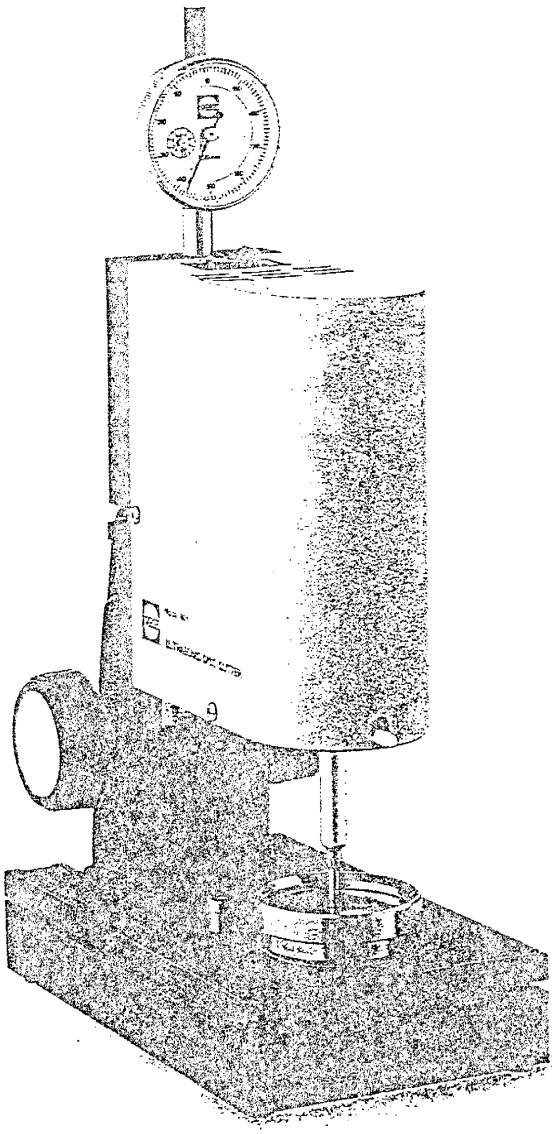

Fig 12.

gatan

Model 601
Ultrasonic Disc Cutter

double coated polyester w/polycoated line works well to secure the sample on the slide.

Procedure

Because the breadth of the most intense peak varies as $1/\cos\theta$, the broadening caused by small crystallite sizes is most conspicuous at large Bragg angles (Klug and Alexander, 1974). In this study, reflections from the (212) plane ($67.76°2\theta$) and the (104) plane ($73.48°2\theta$) were analyzed. The slits used are: .5° Divergent Slit; .5° Scatter Slit; .15° Recieving Slit; and .15° M (slit between monochronometer and counter).

(212) REFLECTION

The steps necessary to determine temperature from the 212 reflector of chert and other forms of microcrystalline silica are as follows (Renault, 1980):

[1] Determine the percent resolution (sharpness of the quartz quintuplet) of the 212 $K\alpha_1$ and 212 $K\alpha_2$ peaks (Fig. 13) of the sample and of a quartz standard (sample with a very large domain size; preferably greater than 10,000 angstroms) from the equation:

$$R = \frac{P - V}{P} \times 100 \quad , \tag{5}$$

where R is the percent resolution, P is the peak height above backround, and V is the valley height above backround.

[2] Determine the 212 $K\alpha_1$/203 $K\alpha_1$ intensity ratio (P/H;Fig. 13) of the sample and the standard.

[3] Determine the instrument broadening, b, and the sample broadening, B, from figure 14.

[4] Determine β/B from figure 15 and calculate β.

[5] Calculate the domain size, D, from eqn. 3.

[6] Calculate temperature from eqn. 4 or 5.

(104) REFLECTION

The steps necessary to determine temperature from the (104) reflector are as follows:

[1] Run sample and quartz standard from 72.5° to 74.5°2θ (Figure 16 is an example of (104) x-ray diffraction profile). Data are stored on magnetic tape under a *.raw* file name (i.e. z03278.raw).

[2] Data files are converted to ASCII files (*.asc*) and alfa removed files (*.MA2*) using the Rigaku software "CONVRT" and "PEAKS", respectively. *.MA2* files are converted to *.alf* files using the program "CONALF".

[3] Transfer *.asc* and *.alf* files from main frame to diskette (at same time converting from CP/M to MS-DOS).

[4] Deconvolute sample and quartz standard using "Deconorm.bas" (modified by Renault (unpub.) after Wiedman et. al., 1987).

[5] Calculate crystallite size and temperature using "Sizetemp".

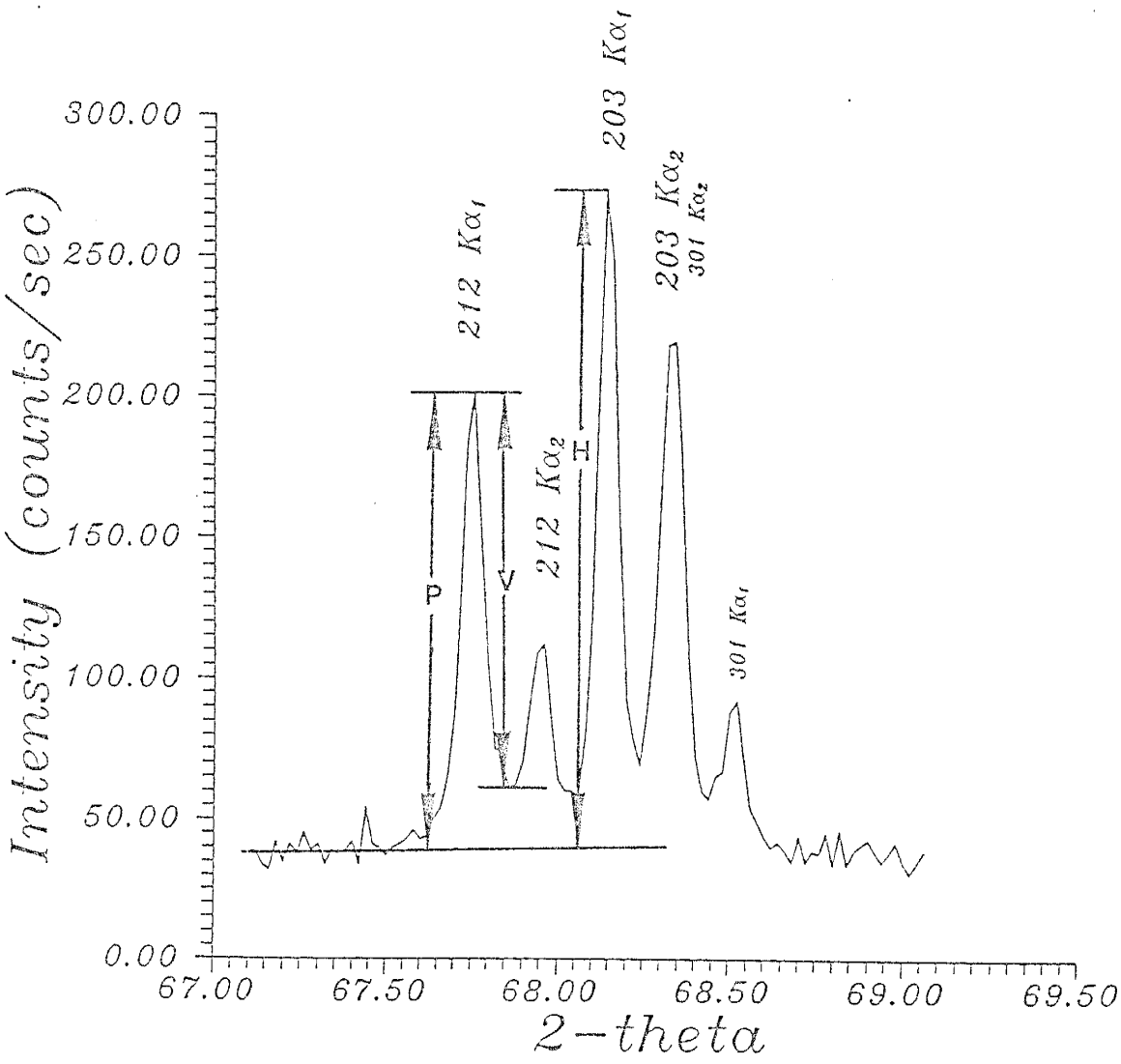

Figure 13. Quartz diffraction profile for (212) reflector (after Renault, 1980).

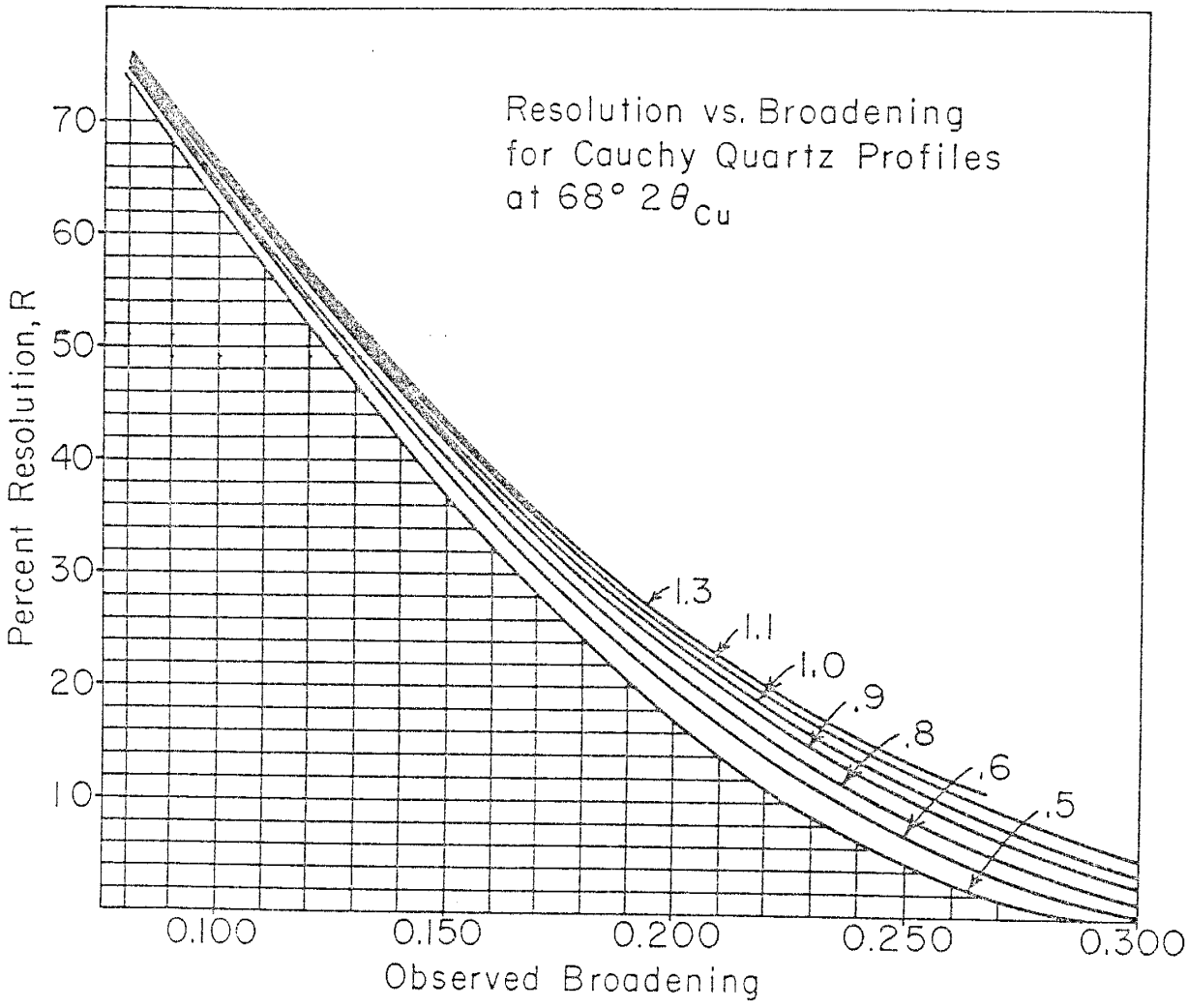

Figure 14. Resolution as a function of broadening for various (212)/(203) intensity ratios (after Renault, 1980).

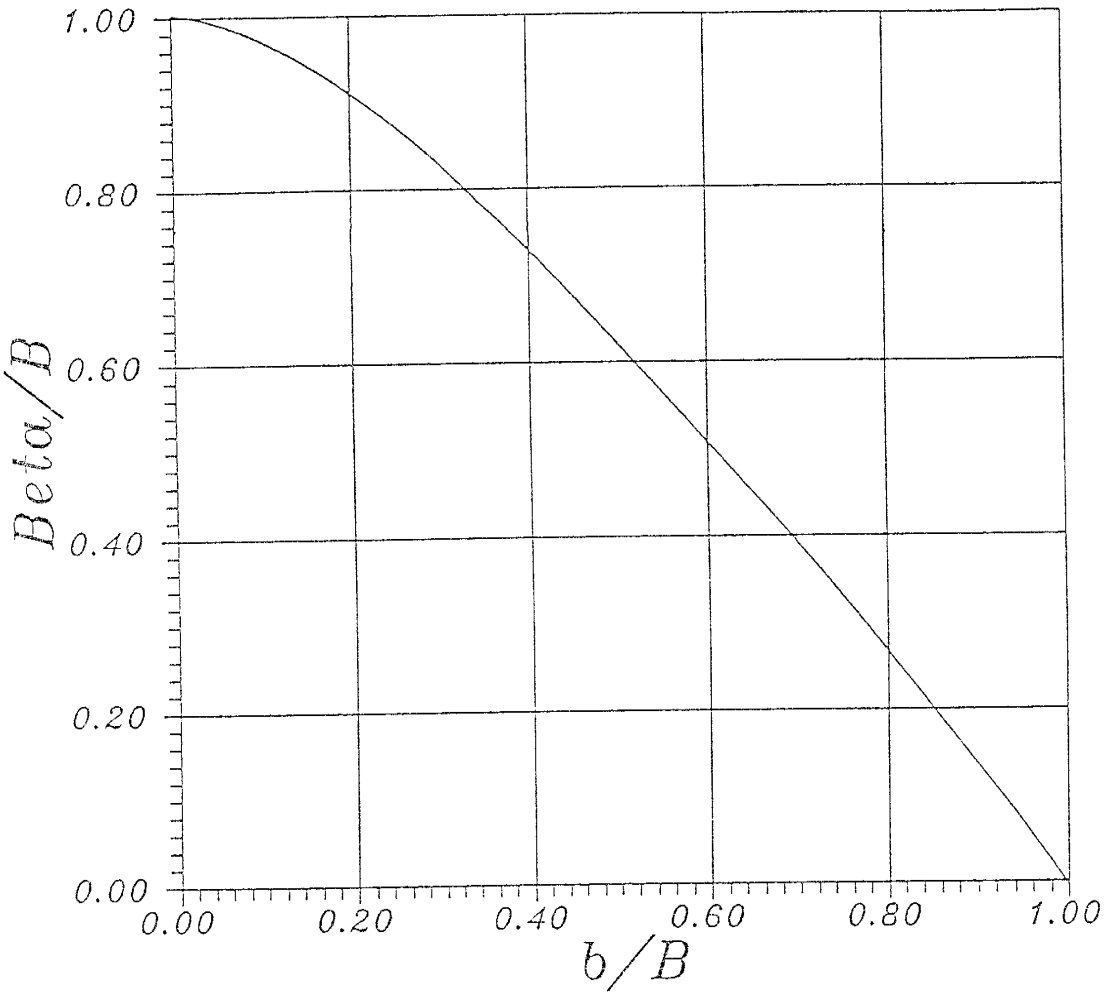

Figure 15. Jones Diagram (after Klug and Alexander,1974). b is the instrumental braodening; B is the sample broadening; and beta is the pure diffraction line broadening.

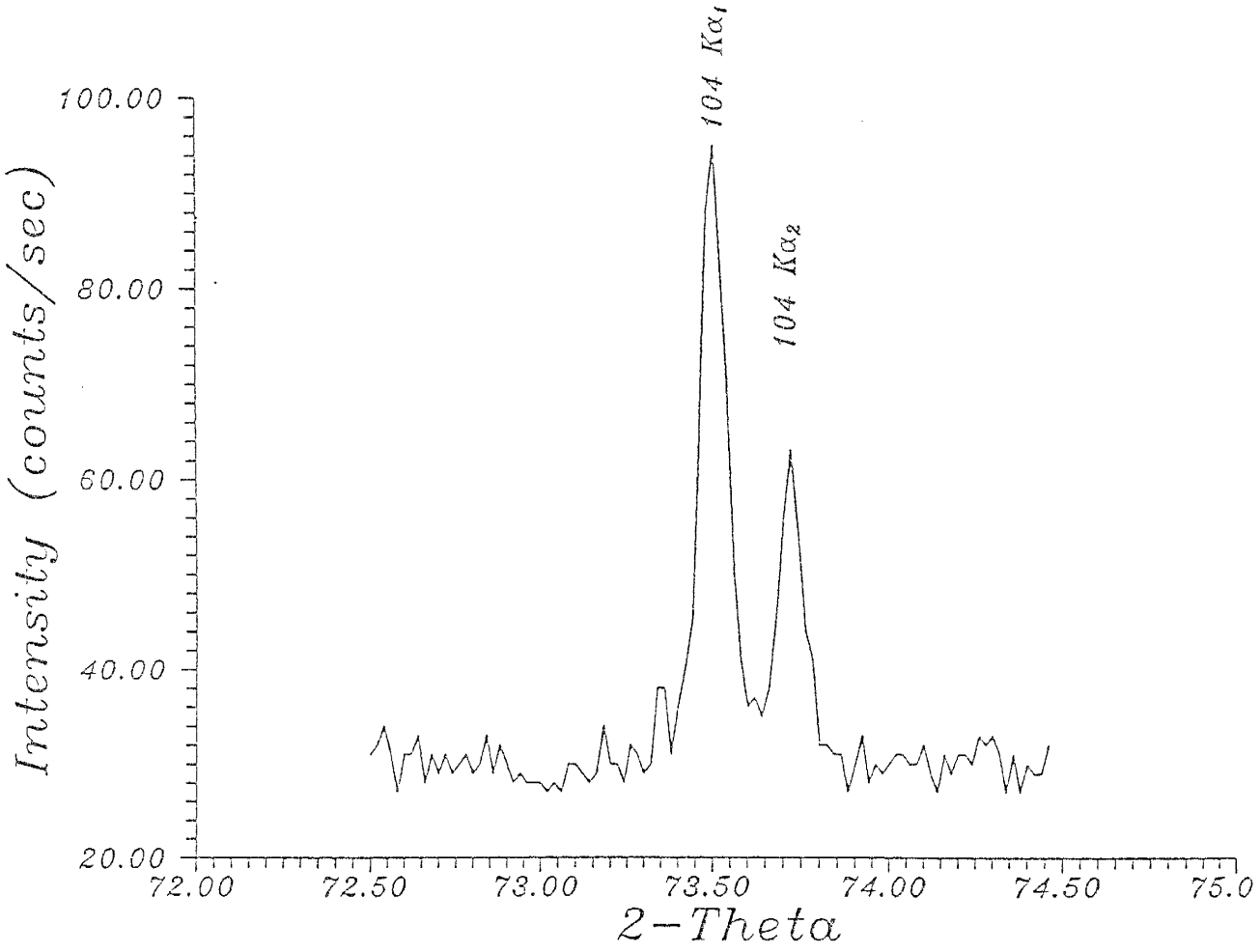

Figure 16. Quartz diffraction profile for the (104) reflector.

CHAPTER 2: Origin of Chert

Introduction

In the past, there has been much controversey surrounding the origin of chert. The basic problem has been three-fold (Hesse, 1990a): 1) the source of the silica; 2) the depositional environment of siliceous sediments and 3) the diagenesis of chert and chert bearing rock. During the past few decades a large body of experimental data (Williams, et. al., 1985; Williams and Crerar, 1985; Mizutani, 1970, 1977; Kolodny, et. al., 1980; Kastner, et. al., 1977; Stein and Kirkpatrick, 1976; Ernst and Calvert, 1969; Isaacs, 1982; Krauskopf, 1959; and others) along with observational data from cores of the Deep Sea Drilling Project (Heath and Moberly, 1971; Heath, 1973; Lancelot, 1973; Holdsworth and Harker, 1975; Keene, 1975; Kelts, 1976; von Rad, et. al., 1978; Riech, 1979, 1981; Grechin, et. al., 1980; Calvert, 1971; and others) and studies of chert in outcrop (Maliva and Siever, 1989; Jenkyns and Winterer, 1982; Meyers, 1977; Folk and McBride, 1976; McBride and Folk, 1977; Loope and Watkins, 1989; Keller, et. al., 1985; Folk, 1973; Robertson, 1977; and others) have advanced the knowledge of chert genesis considerably.

Three sources of non-detrital silica have been recognized (Hesse, 1990a): 1) siliceous tests and skeletal elements of organisms; 2) weathering solutions in semi-arid climates; and 3) silica supplied in solution by hydrothermal-volcanic systems. Throughout the Phanerozoic, the primary source of silica has been biogenic in origin with only minor amounts being derived from the other two sources (particularly hydrothermal). Today, the total silica production by diatoms, radiolarians, silicaflagellates and siliceous sponges is estimated to be (see Hesse, 1990a) $2.5 \times 10^{16}\ g \cdot a^{-1}$ (grams per annum), which is about 25 times the input of silica to the ocean ($11.7 \times 10^{14}\ g \cdot a^{-1}$; Fig. 17). However, this discrepency does not present a problem when internal recycling is considered. It has been estimated (see Hesse, 1990a) that 90% – 99% of the silica extracted from the surface seawater is redissolved before burial.

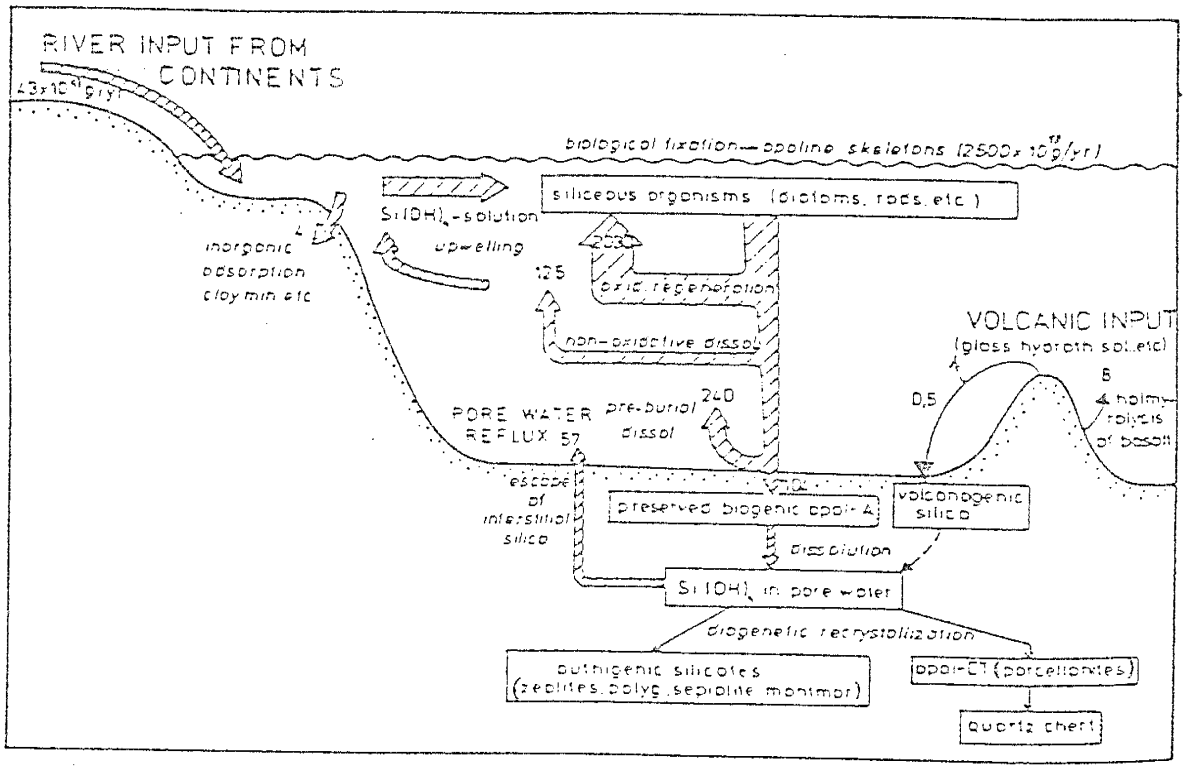

Figure 17. Global dissolved silica budget of the oceans. All numbers are in 10^{13}g SiO_2 per annum (from Hesse, 1990a).

Dissolution of the skeletons starts after death while settling through the water column, and continues after deposition and burial. This considerable amount of redissolution prior to burial suggests that before chert can form there must be a large deposit of silica (siliceous ooze). This requires that chert form in environments where there is high production of opal-A in the surface waters. Today, (and presumably in the geologic past) this occurs in zones of oceanic upwelling; where nutrients dissolved at some depth are returned to the surface. Siliceous oozes are found in peri-equatorial zones, the subarctic and Antarctica and in certain continental-margin regions (Fig. 18) (Jenkyns, 1986).

A number of nomenclature systems, based on texture or mineralogy, have been devised and used in the literature to designate diagenetic concentrations of silica. Because there is no set nomenclature, terms used in this report are defined below.

Silica: Solid form of SiO_2 which occurs naturally in at least nine different polymorphs, which include tridymite and cristobalite (all forms), coesite and stishovite, high (β) and low (α) quartz. These forms are characterized by distinctive crystallography, optical characteristics, physical properties, pressure-temperature stability ranges (Fig. 19), and occurrances. (Parker, 1988)

Siliceous ooze: Fine-grained pelagic deposit of the deep ocean floor with more than 30% siliceous material of organic origin. Radiolaria and diatom remains are the major constituents of the siliceous oozes, which tend to occur at depths in excess of 4500 m. (Allaby and Allaby, 1990)

Chert: A hard, compact, cryptocrystalline, varicolored sedimentary rock with semi-vitreous luster and consisting dominantly of silica. It has a splintery to conchoidal fracture and may contain minor amounts of other minerals (Glossary of Geology).

Porcelanite: A siliceous rock that is less hard and less compact than chert. It has a dull luster and adheres to the tongue when licked. It usually consists of either opal and quartz or quartz together with clays. carbonate, zeolites, or iron and manganese minerals.

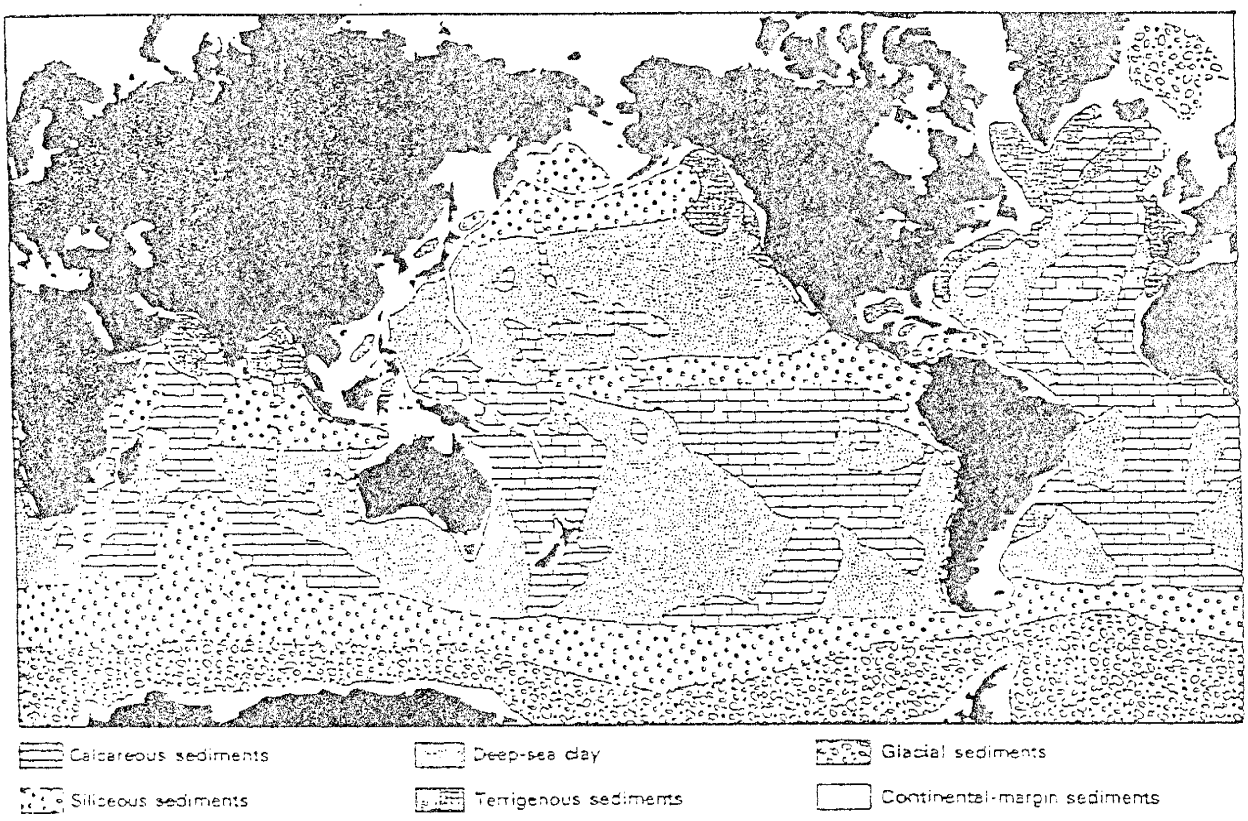

Figure 18. Global distribution of principal types of pelagic and other sediments on the ocean floors (from Jenkyns, 1986).

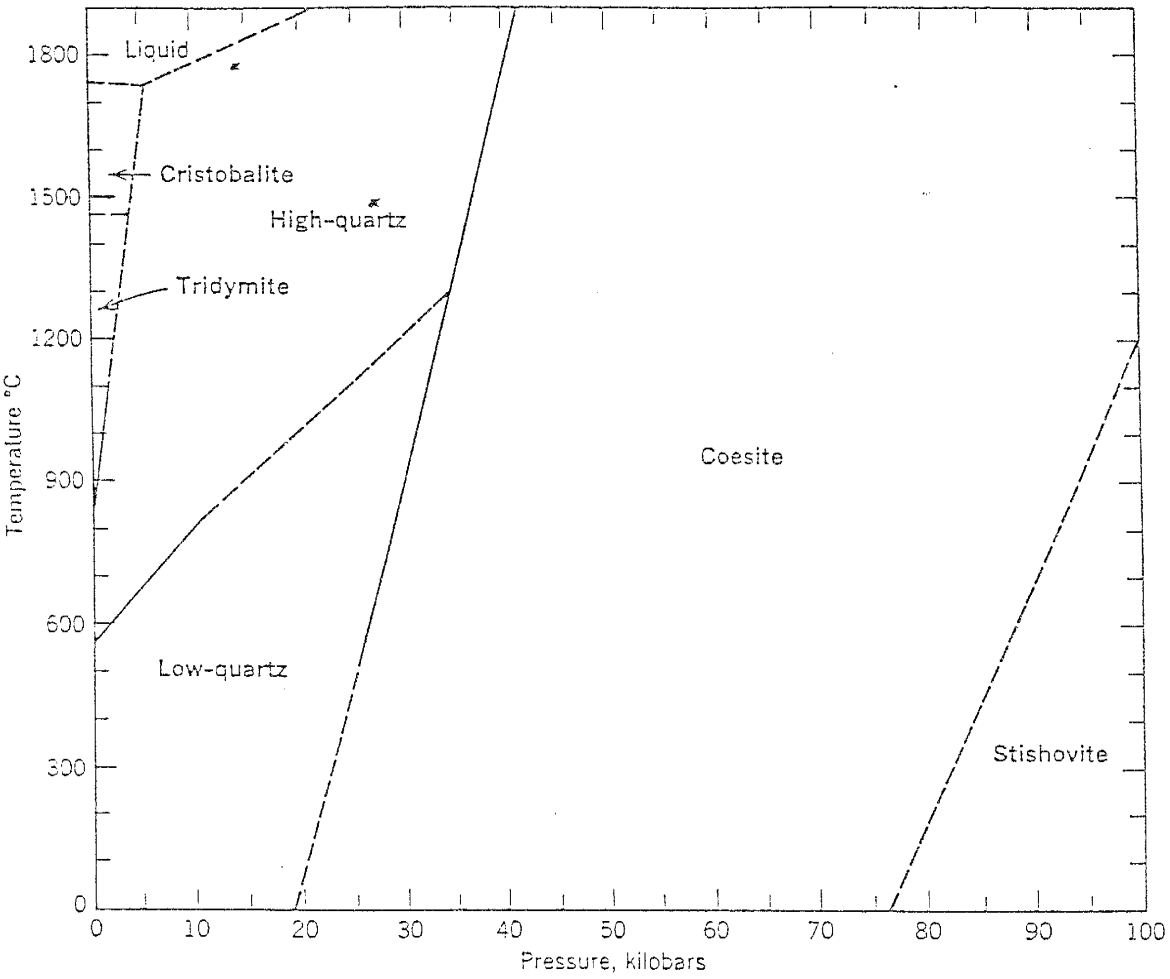

Figure 19. Stability relations of SiO_2 polymorphs (from Klein and Hurlbut, 1985).

It includes what otherwise may be called siliceous claystone/ siltstone/ mudstone. (Glossary of Geology).

The classification of opal will follow that of Jones and Signet (1971):

Opal-A: X-ray amorphous silica commonly found in the tests of siliceous micro-organisms. A typical diffractogram shows only a very broad bulge between 18° and 30° 2θ (Fig. 20).

Opal-CT: The *"CT"* stands for cristobalite/tridymite and thus represents a more ordered silica structure than opal-A. A typical diffractogram shows broad peaks at 21° and 22.5° 2θ (Fig. 21). **Opal-CT lepisphere:** Small spheres of opal-CT less than $5\mu m$ in diameter which consist of an interpenetrative growth of tiny cristobalite/tridymite blades (Fig. 22) (Hesse, 1990a). The ultrastructure of the lepisphere is not an arbitrary cluster of spherulitic, fibrous, radiated, or randomly intergrown crystallites but governed by the complex (3034) and (1016) twinning laws of tridymite (Fig. 23) (von Rad, et. al. 1978).

Chert diagenesis in deep water environments

The formation of chert through the diagenetic transformation of biogenic opal was introduced by Bramlette (1946). Studies of Deep Sea Drilling Project cores (Heath and Moberly, 1971; Lancelot, 1973; and others) confirmed that chert forms by the following transformation:

$$\text{Opal-A} \rightarrow (\text{Opal-A}') \rightarrow \text{Opal-CT} \rightarrow \text{quartz}$$

This progressive diagenetic transformation follows a dissolution- reprecipitation pathway (Williams and Crerar; 1985, Hesse, 1990a). The most obvious lines of evidence which suggest this pathway are listed here (Williams et. al., 1985). **First, texture.** As burial progresses, diatom and radiolarian tests fragment and begin to dissolve followed by the precipitation of opal-CT within the tests and pore spaces as cements, lepispheres, and blades. **Second, retention of fabric.** This has been used as evidence for solid-state transformation of opal-CT

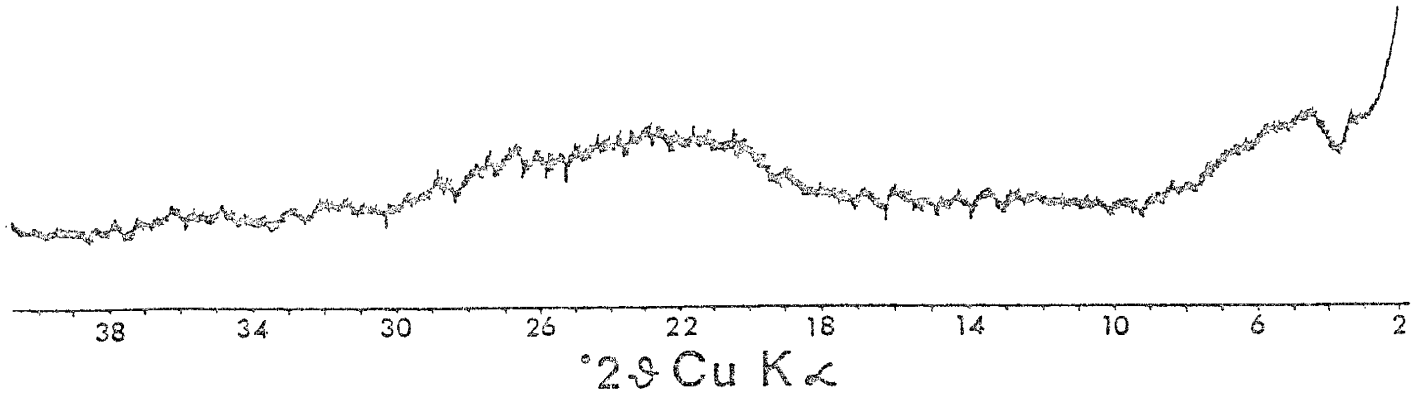

Figure 20. X-ray diffraction pattern of a radiolarian ooze (after Lancelot, 1973).

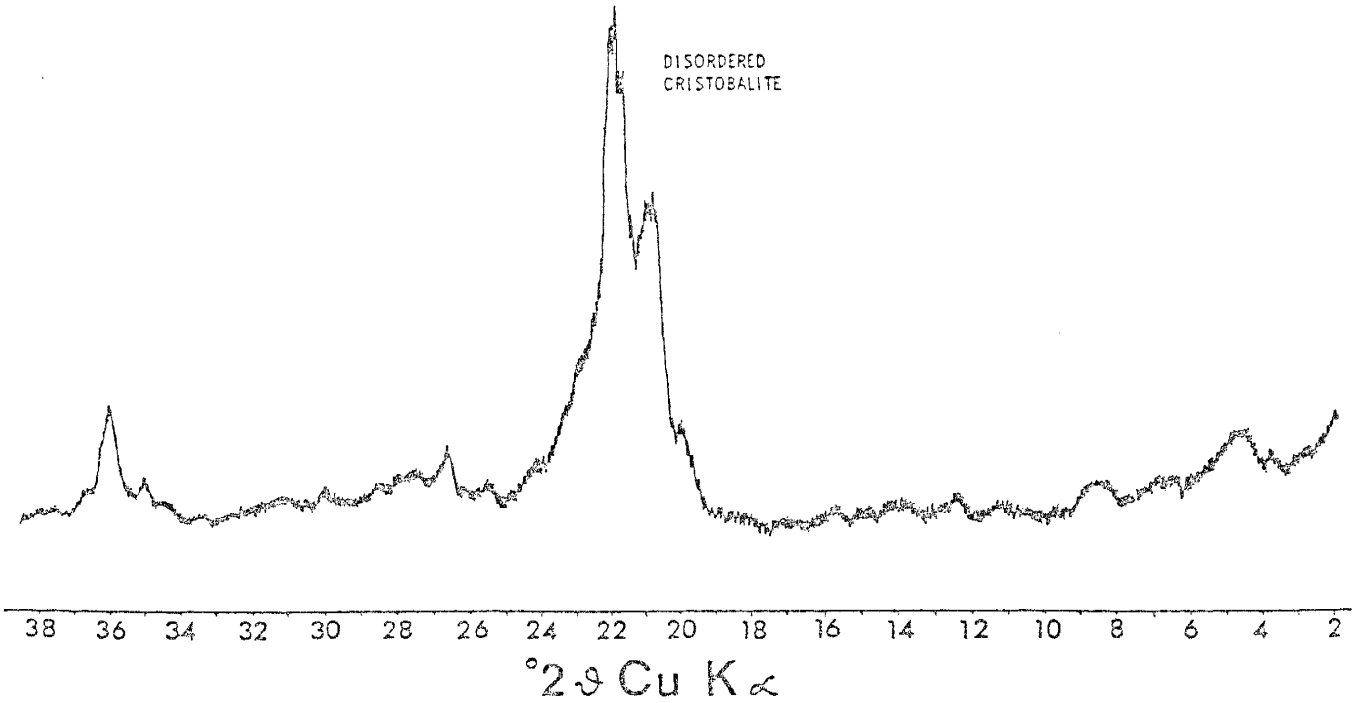

Figure 21. X-ray diffraction pattern of a porcelanitic chert (after Lancelot, 1973).

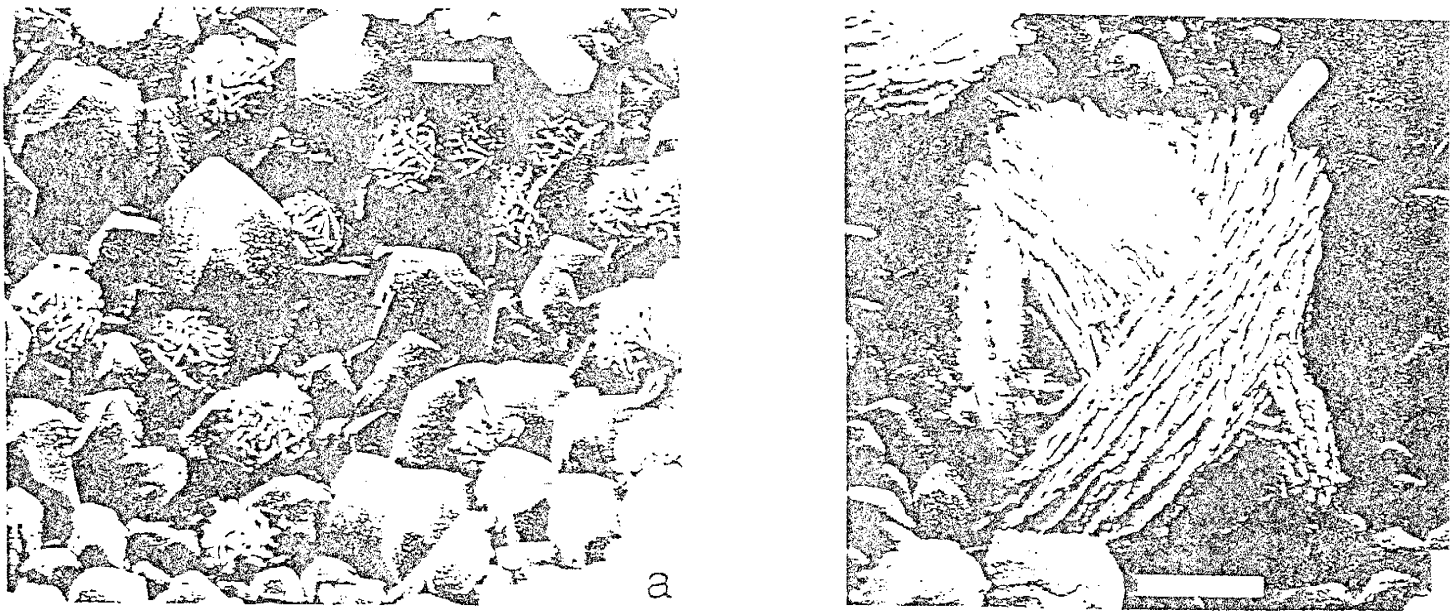

Figure 22. (a) Small opal-CT lepispheres (2-3 um in diameter) growing on euhedral calcite crystals in a cavity in partially silicified Maestrichtian chalk, DSDP 14-144-3-2, 103-104 cm. (b) Opal-CT blades of a "juvinile" lepisphere displaying twinning angle of 70° corresponding to the intersection angle of the faces of a cristobalite octahedron as shown in figure 23 (from Hesse, 1990a)

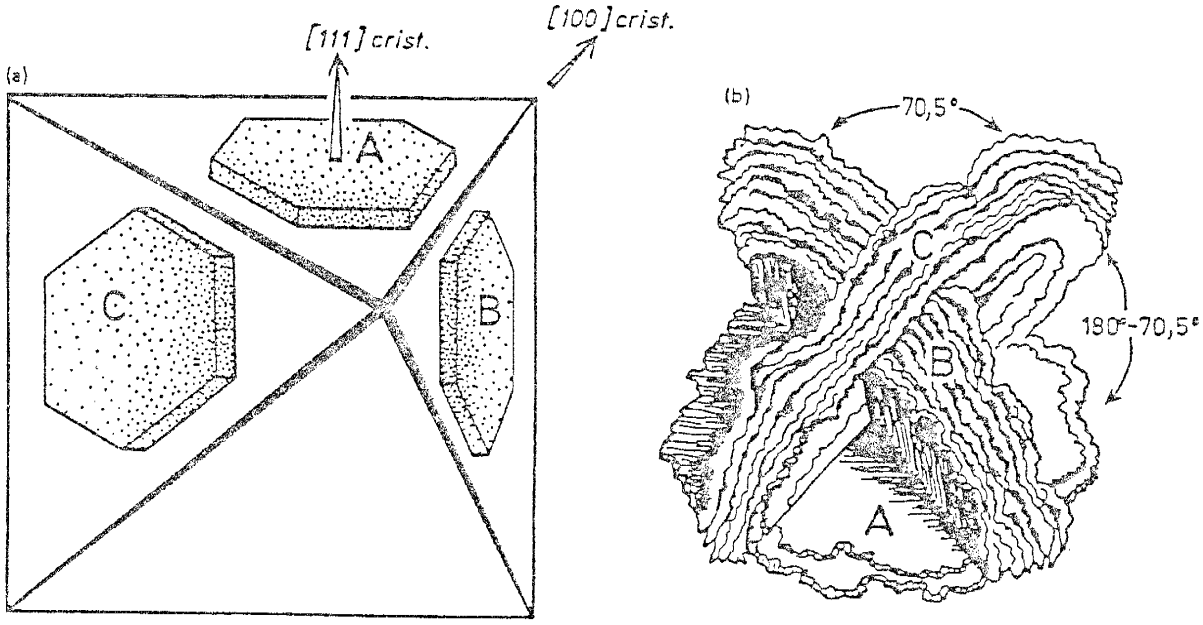

Figure 23. Ultrastructure of opal-CT lepispheres. (a) three hexagonal tridymite plates (basal/pinacoids) on a cristobalite octahedron, indicating tridymite type twinning of opal-CT. (b) Schematic sketch of "incipient" lepisphere with subparallel opal-CT blades (rounded, ragged edges) oriented parallel to the three directions of the tridymite plates (A,B,C) in (a) (after von Rad et. al., 1978).

to quartz (Heath and Moberly, 1971; Ernst and Calvert, 1969). However, fabrics can be retained by a grain-by-grain replacement mechanism with slow rates of dissolution and immediate local reprecipitation. **Third, $^{18}O/^{16}O$ ratios in the Monterey Formation (Miocene, California).** $\delta^{18}O$ decreases abruptly at the opal-A/opal-CT and opal-CT/quartz boundries but remains relatively constant within each zone. This suggests dissolution-reprecipitation and isotopic fractionation between each silica phase and interstitial waters at ambient temperatures. **Fourth, the strength of the SiO_2 bond.** If the transformation is to occur in the solid state, SiO_2 bonds must be broken which would require an activation energy at least equal to the bond strength of 89 kcal/mole. Measured activation energies are much lower: 17.0 kcal/mole and 14.3 kcal/mole for the opal-A $\rightarrow$ opal-CT and opal-CT $\rightarrow$ quartz transformations, respectively, in KOH solutions (see Williams, et. al, 1985). In pure water, Ernst and Calvert (1969) measured an activation energy of 23.2 kcal/mole.

Because of this dissolution-reprecipitation mechanism, the diagenetic pathway of silica is controlled by the aqueous solubility of the individual phases (Williams and Crerar, 1985). The aqueous solubility of silica parallels the diagenetic sequence with amorphous silica > cristobalite > quartz (Williams et. al., 1985) and is dependent upon temperature, pressure (to a lesser extent), pH, crystal structure, and particle size and shape (Fig. 24).

Temperature (Williams et. al., 1985): The solubiltiy of all forms of silica increases with temperature (Fig. 24a). The primary effects of temperature are to decrease the relative degree of supersaturation while increasing the concentration, and to increase rates of diagenetic reactions.

Pressure (Williams et. al., 1985): An increase in pressure will increase silica solubility (Fig. 24c) but the change is small compared to temperature (except at high temperatures) and can usually be ignored.

pH (Hesse, 1990a): In solutions of pH < 9, dissolved silica is present predominantly in the

form of monomeric silicic acid (H_4SiO_4):

$$SiO_2(s) + H_2O \rightarrow H_4SiO_4(aq).$$

In solutions of pH > 9, H_4SiO_4 dissociates in a first step to $H_3SiO_4^-$ and at higher pH values in a second step to $H_2SiO_4^=$ (Fig. 24d). These dissociations raise the solubility significantly because the total dissolved silica concentration is the sum of the dissociated and undissociated species (Hesse, 1990a). At higher temperatrues the solubility of silica increases at lower pH values (The curve shifts toward lower pH values).

Surface area (Williams et. al., 1985): Normally, surface area will not significantly alter the chemical behavior of a substance, but when the surface to volume ratio is large (as is the case for micro-organisms) solubilities are altered significantly. As specific surface area increases the solubility increases (Fig. 24b).

Opal-A to Opal-CT transformation:

As mentioned earlier, 90% – 99% of biogenic opal-A is redissolved before reaching the sea floor due to the undersaturated nature of seawater. Continued dissolution of opal-A in the sediment during burial is the result of slowly increasing temperature and pressure (see Fig. 24) (Hesse, 1990a; Williams, et. al., 1985; Williams and Crerar, 1985). In contrast with the former dissolution, dissolution during sediment burial occurs in a more or less closed system (Hesse, 1990a). Therefore, this process raises the concentration level of dissolved silica in the interstitial fluid. When the amount of dissolved silica reaches 20 - 30 ppm (@ 25°C; Williams, et. al., 1985) the solution will be supersaturated with respect to cristobalite, at which point opal-CT lepispheres will begin to precipitate within the chambers of the shell (Fig. 25). In the event supersaturation is reached before opal-A dissolution has gone to completion, dissolution will be interupted by the reprecipitation of a less soluble substance with a slightly more ordered structure than opal-A (Hesse, 1990a). This precipitate is commonly referred to as opal-A′ and is redissolved prior to the precipitation of opal-CT. Although it is a relatively

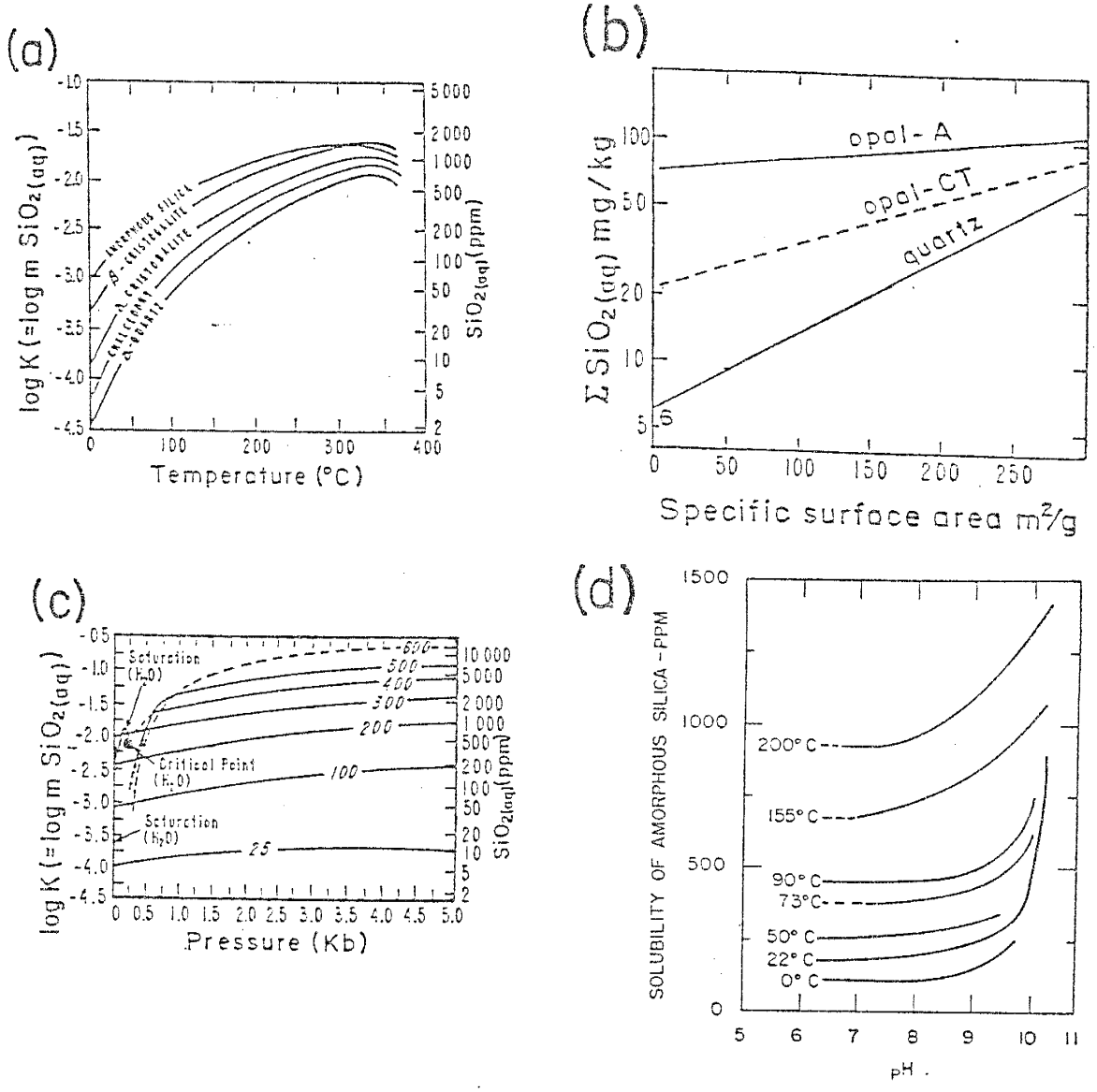

Figure 24. Solubility diagrams for various silica phases as a function of (a) temperature, (b) specific surface area, (c) pressure (contours are temperature (°C) and (from Hesse, 1990a). (d) solubility of amorphous silica versus pH at different temperatures (from Iler, 1979).

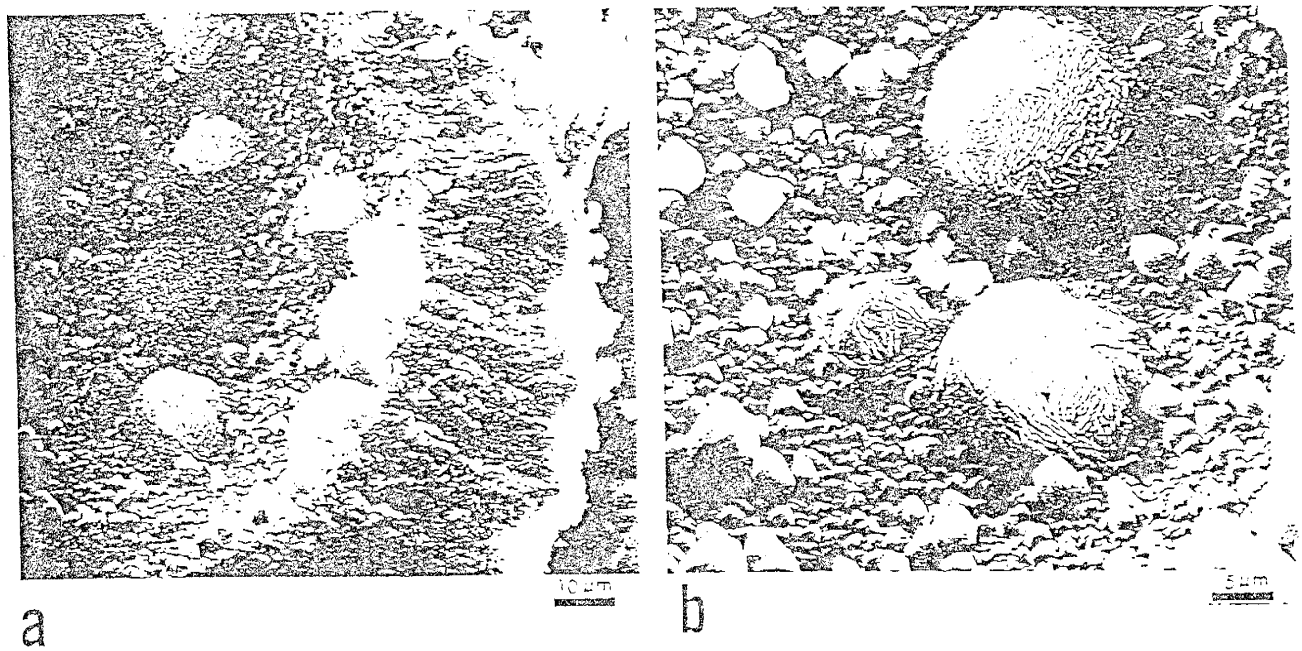

Figure 25. a) Seven silica lepispheres within a foram chamber. Wall is lined by a forest of euhedral, blocky secondary calcite crystals and has been partially recrystallized. b) Detail of a). (after Kelts, 1976).

short lived form, the occurrance of opal-A′ has been documented in Deep Sea Drilling Project cores (Lancelot, 1973).

Opal-Ct to quartz transformation:

The transformation of opal-CT to quartz was originally thought to be a solid state process by Ernst and Calvert (1969) and Heath and Moberly (1971). The low activation energy of the transformation (23 kcal/mole; Ernst and Calvert, 1969) suggested that unless a high heat source existed, this transformation would procede very slowly. The reported existance of opal-CT in Cretaceous age porcelanites was evidence for this (Kelts, 1976). Stein and Kirkpatrick (1976) analyzed the experimental products of Ernst and Calvert (1969) under the Scanning Electron Microscope and found needles and hexagonal doubly terminated prisms of quartz. They concluded that the size and morphology of the quartz crystals formed according to a nucleation and growth model rather than a solid-state transformation (Stein and Kirkpatrick, 1976). In addition, the cristobalite undergoes a shift in the (101) diffraction peak from 4.1 Å to 4.05 Å with increasing burial (Hesse, 1990a; Mizutani, 1977). This shift is most likely the result of progressively increasing crystallinity due to continuous crystal growth; tridymite layers preferentially dissolving and cristobalite layers preferentially precipitating (Williams and Crerar, 1985). When the (101)-spacing is approximately 4.04 Å, the opal-CT redissolves. Clays and/or carbonates, plus increasing burial temperatures, act to keep the degree of silica saturation in the pore waters low, providing the conditions best suited for slow quartz precipitation from a monomeric solution (Williams and Crerar, 1985).

At low temperatures and pressures, quartz is the thermodynamically stable phase (see Fig. 19). Why, then, should cristobalite precipitate as a metastable intermediate step? It is probably due to the internal structure of opal-A. In supersaturated solutions, dissolved silica polymerizes forming first oligomers (dimers, tetramers and ring structures) and later

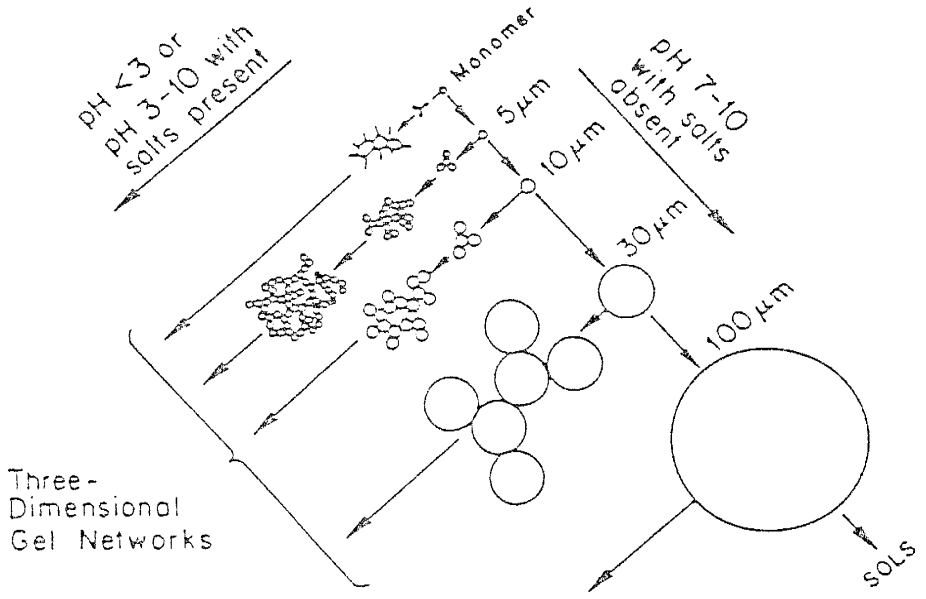

Figure 26. Polymerization behavior of dissolved silica as a function of pH and ionic strength of the solution (from Hesse, 1990a).

higher molecular weight polymers (Fig. 26) (Hesse, 1990a). The faces of any embryonic quartz crystal would be crowded by silanol groups (oligomers) which would not have time to be properly fitted into the crystal lattice (Hesse, 1990a). Quartz growth will be blocked and opal-CT will precipitate instead. This is a good example of the Ostwald step rule (or Ostwald ripening) which basically states that crystallization progresses from the phase of highest entropy to the phase of lowest entropy (Hesse, 1990a; Williams and Crerar, 1985). The Ostwald ripening process also lowers the equilibrium solubility of silica counterbalancing the increase in solubility as temperature increases, which is an essential condition for the precipitation of quartz (Hesse, 1990a; Williams et. al., 1985; Williams and Crerar, 1985).

Rates of diagenetic transformations

During the analysis of DSDP cores, it was found that silica diagenesis proceeds faster in certain horizons than others. The transformation of opal-A to opal-CT is slower in detrital rich rocks than in detrital poor rocks (Fig. 27). It has been shown experimentally (see Williams et. al., 1985; Williams and Crerar, 1985) that in silica enriched fluids, clay minerals remove silica, presumably by adsorption. This will lower the amount of dissolved silica below the equilibrium solubility. Therefore, the rate of opal-CT precipitation will be retarded. By the same reasoning, the presence of clay minerals tend to enhance the transformation of opal-CT to quartz.

Studies of DSDP cores also revealed that silica occurring in carbonates or carbonaceous oozes was quartz, while silica within overling clastic units was predominantly opal-CT. This lead some investigators to believe that, in carbonates, opal-A was converted directly to quartz (Lancelot, 1973; Heath and Moberly, 1971). Direct transformation of opal-A to quartz is possible, but only in an environment where the silica concentration is below the equilibrium solubility of opal-CT (Fig. 24a; cristobalite curve) (Kastner et. al., 1977; Williams et. al., 1985). However, in interstitial waters of most siliceous oozes, the concentration of silica is above the equilibrium solubility of opal-CT (Kastner et. al., 1977). Therefore, the rate of

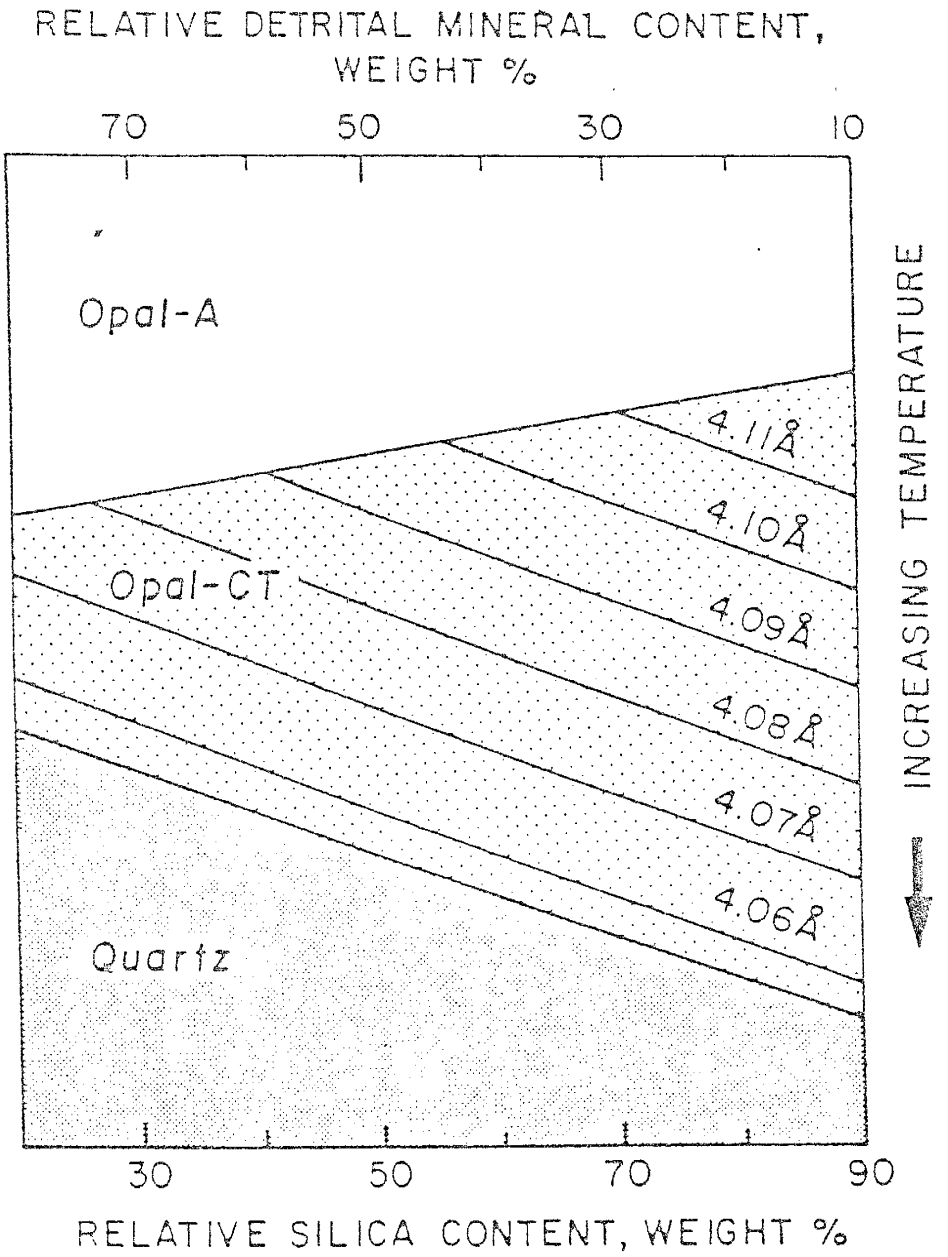

Figure 27. Schematic summary of relation between detrital mineral content and apparent rate of silica phase changes (From Williams et. al., 1985).

transformation within carbonates must be accelerated. This may have something to do with carbonates having little or no detrital content, but most likely results from the chemical environment. Experimental work by Kastner et. al. (1977) has shown that in the Mg-enriched environment of carbonates, a compound nucleates with an Mg:OH ratio approximately 1:2 (i.e. $Mg(OH)_2$; Brucite) which provides nucleation sites for opal-CT lepispheres. The Mg is supplied by seawater and the hydroxyl groups are believed to be supplied by the dissolution of calcium carbonate (Hesse, 1990a). When the hydroxyl groups have been used up, the rate of nucleus formation declines and the existing opal-CT embryos grow to well developed lepispheres, provided continued opal-A dissolution supplies the required silica.

Rates of silica diagenetic reactions are also dependent on temperature (Grechin et. al., 1980; Heath and Moberly, 1971; Lancelot, 1973; Riech, 1980). The temperature at which opal-A converts to opal-CT has been estimated, based on bottom hole temperatures in DSDP cores, to be 35 °C to 51 °C off the coast of Baja, California (Grechin et. al., 1980), and in the Bering sea (see Hesse, 1990a). In the Temblor Range, California, the conversion temperature ranges from 41 °C to 56 °C based on oxygen isotope data (see Hesse, 1990a). The temperature for the conversion from opal-CT to quartz is less well constrained, ranging from 31 °C to 165 °C (Williams et. al., 1985).

Time also has a significant role in the conversion of opal-A to quartz and is also dependent on tempearture. In the presence of an elevated heat source, the minimum time for the appearance of opal-CT is 10 m.y. (Hesse, 1990a). If no elevated heat source is present then the conversion will take longer. With age and increase in temperature (burial), opal-CT undergoes the progressive ordering of internal structure. At a depth of 500m opal-CT will begin to convert to quartz.

Chert diagenesis in shallow water environments

Chert diagenesis in shallow water environments follows a similar pathway as in deep water environments. Biogenic opal-A is supplied through the dissolution of sponge spicules (see

Land, 1976), and, along the western margins of continents, of siliceous micro-organisms and inorganically by the circulation of alkaline meteoric waters (Hesse, 1990b; Kolodny, 1980). The transformation to chert in shallow water environments is considered to be essentially the same but may involve deviations from the expected path.

CHAPTER 3: Results

Within the Loma de las Cañas region two areas were chosen for sampling (Fig. 28): the Cerros de Amado area, and an area south of Arroyo de las Cañas. Samples collected from limestones in the Cerros de Amado area and south of Arroyo de las Cañas will be used in an attempt to establish a paleogeothermal gradient. In each area, great care was taken to extract samples from the least disturbed strata; this proved to be difficult. Faults from every group (strike-slip, normal, reverse/thrust) are more than adequately represented; sampling undisturbed strata almost always meant that area furthest from a known fault. Both areas have also experienced periods of intense folding. Fortunately, these periods are confined to certain sections or formations and are not laterally continuous making them easily avoided when sampling. This structural complexity will almost certainly complicate the interpretation of temperatures due to the increased possibility of either recrystallization of the chert by hydrothermal processes or tectonic (adiabatic) heating; both processes will increase the temperature. There are a few deposits of hydrothermal barite-fluorite located in this region, the Gonzales Precambrian block is one such deposit. Chert and other forms of microcrystalline silica from the Gonzales Precambrian block were sampled to determine the temperature of mineralization. These temperatures will be compared with temperatures from the other areas to determine if burial temperatures could have been affected by hydrothermal processes.

Cerros de Amado

Detailed mapping of the Cerros de Amado area was first done by Rejas (1965). Within the area a complete section of Pennsylvanian Sandia Formation and Madera Group is exposed (refer to fig. 29 for stratigraphy). Two isolated blocks of Precambrian granite were also mapped, the eastern most block is the Gonzales Precambrian block (detailed mapping of

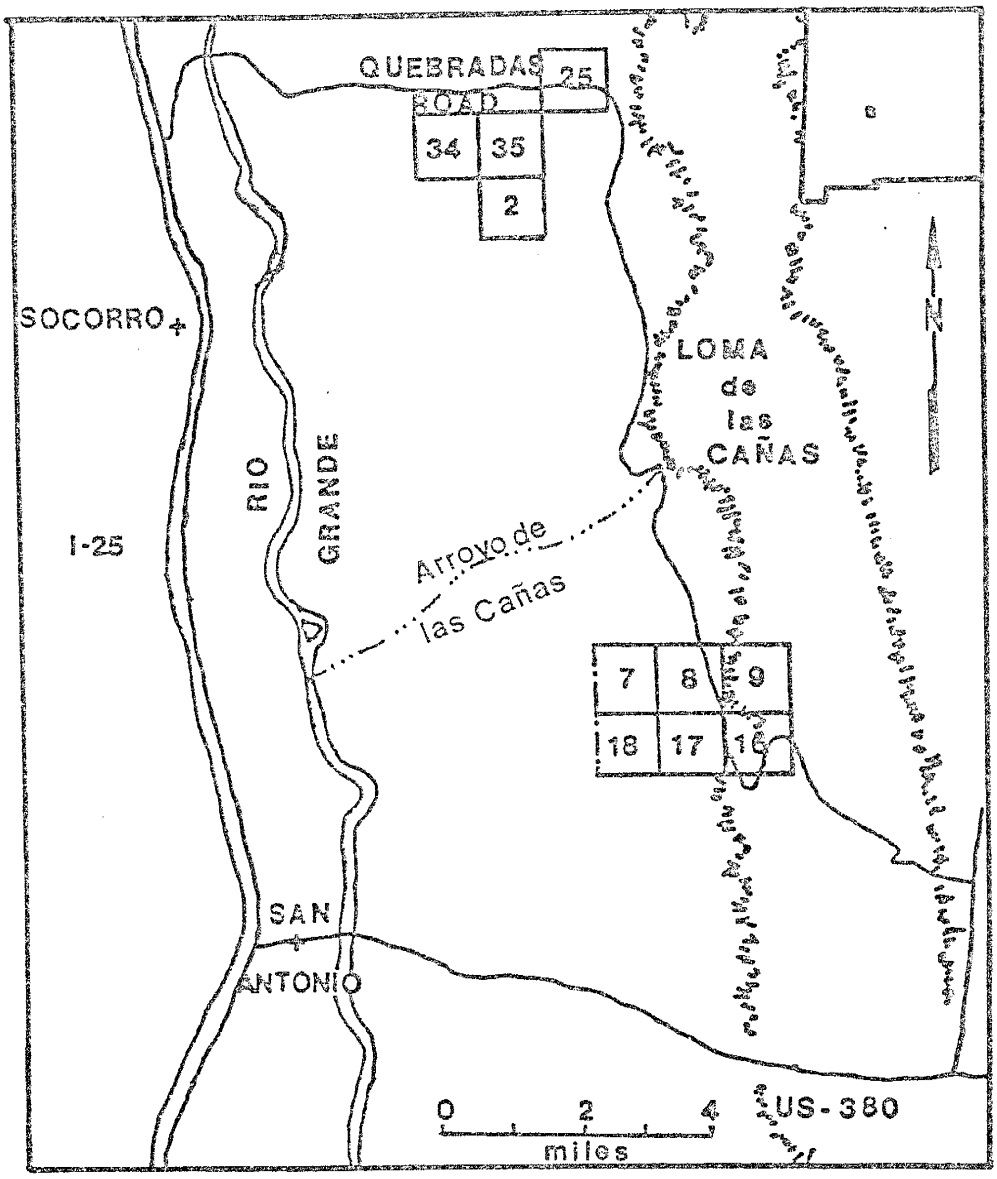

Figure 28. Map showing the location of the Cerros de Amado area and area south of Arroyo de las Canas.

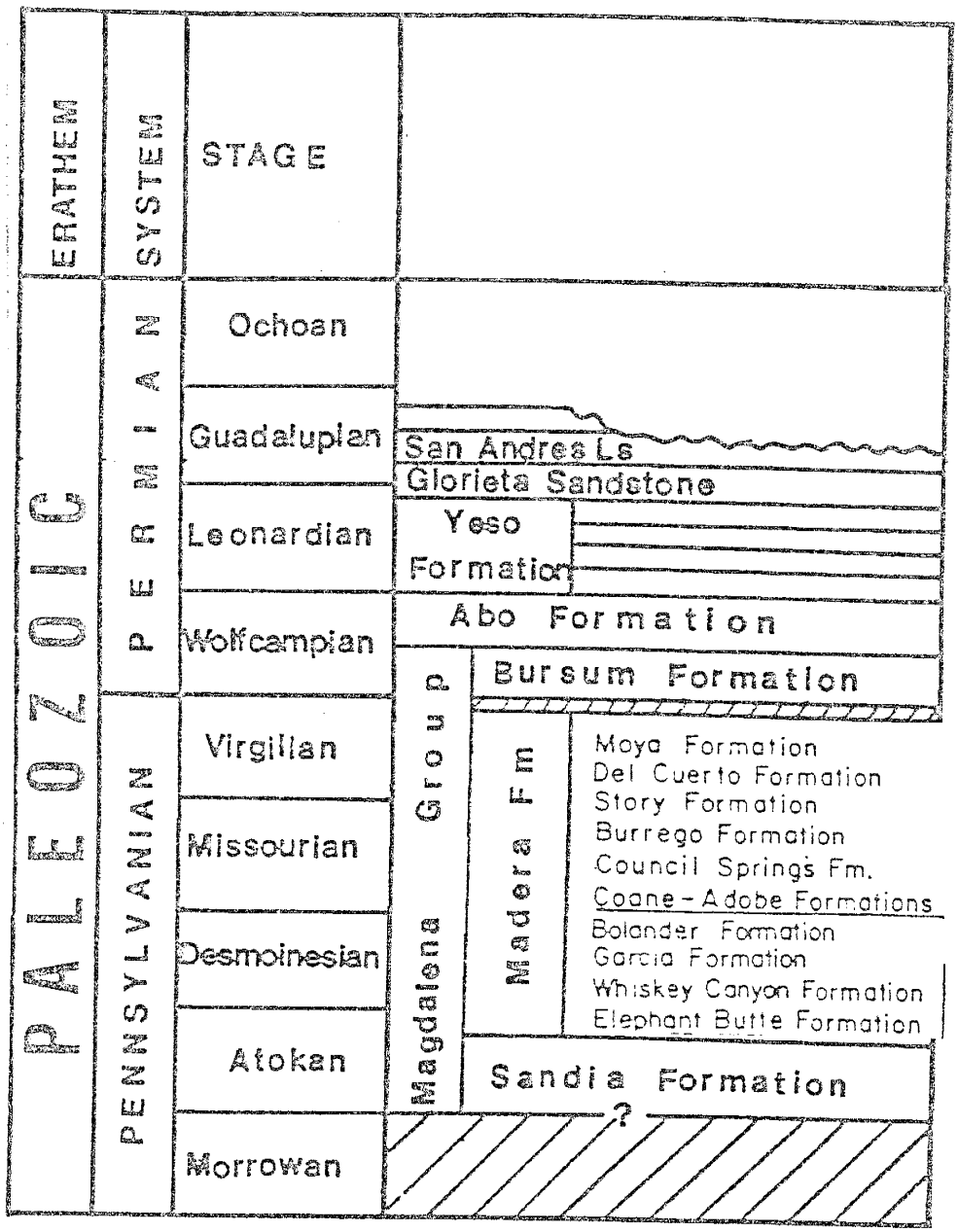

Figure 29. Generalized stratigraphic section of Atokan through Guadalupian age rocks in the Socorro region (after Osburn and Lochman-Balk, 1983).

this block was updated at a scale of 1in = 100ft by Smith et. al, 1991). The main structural feature of this area is the Cerros de Amado Fault Zone (Fig. 30), which trends approximately N40E (Rejas, 1965). Rejas reported the occurrance of chert in the Whiskey Canyon, upper member of the Garcia, and Council Springs Formations of the Madera Group. Samples were collected from outcrops of the Council Springs Formation in Sec. 25, T. 2 S.,R. 1 E.; and from outcrops of the Coan-Adobe Formation SE$\frac{1}{4}$ Sec. 27, T. 2 S., R. 1 E. of the Loma de las Cañas 7.5 min. quadrangle (Fig. 30). The Madera Formation is subdivided into these members based of fusilinids (Thompson, 1942). It should be noted that these subdivisions are not well constrained lithologically and therefore are not commonly used. The Gonzales Precambrian block is located in the NE$\frac{1}{4}$ Sec. 2, T. 3 S., R. 1 E. of the Loma de las Cañas quad. and consists of qtz monzanite hosting barite, fluorite mineralization.

Coan-Adobe Formation

Nodular chert was found to occur on limestones interbedded with clastics approximately 25 m below the Council Springs Limestone. Two samples (91C23A and B) were collected 6 m north of an subsidary arroyo to Arroyo del Piño. Sample 91C23C was collected approximately 31 m northeast (upsection) of 91C23A and B. Cores were cut from 91C23B and C

Council Springs Formation

Three outcrops located in central Sec. 25, T. 2 S., R. 1 E. (labled A to C in Fig. 30) were sampled. Chert collected from the base of the formation at sites A and B occurred as gray (A) and white (B) nodules flattened in the plane of bedding. Bedded chert occurs at site C near the middle of the formation. The contact with the limestone is wavy, with a maximum bed thickness of 5.1cm and a minimum bed thickness of .6cm. The bed was traced for about 6.1m at which point the limestone outcrop decrepitates. Because chert can be found in the float it is most likely that this bed is continuous, to what extent is not known. Three samples were collected from this location (91G20D, E, F) and cored.

Gonzales Prospect

Two samples of hydrothermal silica were collected from the Gonzales Prospect; from the Gonzales fault zone (91e21c) and from the central silicified zone (91e21a). Sample 91e21c shows at least four stages of brecciation which are most likely related to movement along the Gonzales fault (Fig. 31). During each stage of brecciation, the jasperoid was fragmented and recemented with microcrystalline silica. In figure 31, the progressive stages are labeled A, B, C, and D, from older to younger.

X-ray Analysis

Temperatures calculated for the 212 and 104 peaks plus the composition of the sample are given in table 4; crystallite size can be found in Appendix A. Because of the greater sensitivity of the [212] calibration data, these temperatures are considered to be more reliable and so the [104] will not be included in the statitical analysis or discussion.

The means calculated from each sample (Table 5) were compared using a student t-test (evaluated using the computer software "EPISTAT") and results are listed in table 6 and 8. The variables in these tables are: T is the number of standard errors required to reach a given confidence level based on normal deviates (Arkin and Colton, 1971); p is the probability; and the **degrees of freedom** is the number of observations in a sample minus the number of parameters estimated from the sample (Davis, 1986). The mean temperature for all but one of the Pennsylvanian cherts are significantly different, which indicates that the observed differences are not an accident of sampling (Arkin and Colton, 1971). The observed differences between the mean temperatures of the hydrothermal silica (Table 7) are not significantly different (difference is an accident of sampling) so both samples probably experienced the same thermal episode.

Table 4. Temperatures (°C) calculated for sedimentary chert and hydrothermal silica in the Cerros de Amado area.

SAMPLE	T_{212}	T_{104}	COMPOSITION [1]
Coan-Adobe Member (Madera Fm.)			
91c23b2	265	352	α-quartz
91c23c1	255	B.D.[2]	α-quartz
91c23c2	263	B.D.	α-quartz
91c23c3	247	312	α-quartz
Council Springs Member (Madera Fm.)			
91g20d1	204	262	— [3]
91g20d2	198	257	—
91g20d3	191	—	—
91g20e1	204	273	—
91g20e2	207	276	—
91g20e3	194	278	—
91g20f1	245	317	—
91g20f2	211	258	—
91g20f3	230	289	—
91g20f4	235	303	—
Pre-Cambrian Gonzales Prospect			
Central Silicified zone			
91e21a1	273	326	—
91e21a3	264	327	α-quartz
Gonzales Fault			
91e21c1	298	363	α-quartz, cristobalite, fluorite
91e21c2	293	444	α-quartz, fluorite
91e21c3	368	351	α-quartz, cristobalite
91e21c4	336	321	α-quartz
91e21c5	288	393	α-quartz

[1] X-ray diffraction, standard scan, 3° to 90° 2θ

[2] Bad Data

[3] Not determined

Table 5. Statistical data (212 peak) for Pennsylvanian cherts collected in the Cerros de Amado area.

SAMPLE	SAMPLE #	n	MEAN	MEDIAN	σ_{n-1}	VARIANCE
91C23B	1	1	—	—	—	—
91C23C	2	3	255	255	8.00	64.00
91G20D	3	3	198	198	6.51	42.33
91G20E	4	3	202	204	6.81	46.35
91G20F	5	4	230	233	14.27	203.58

Table 6. Results from a student t-test (two-tailed) performed on Pennsylvanian cherts from the Cerros de Amado area.

PAIR	T	DEGREES OF FREEDOM	p	MEANS SIGNF DIFFERENT	CONFIDENCE LIMIT
2↦3	9.63	4	6.50×10^{-4}	yes	57.33 ± 57.30
2↦4	8.79	4	9.22×10^{-4}	yes	57.33 ± 53.36
2↦5	2.67	5	4.46×10^{-2}	yes	24.75 ± 24.78
3↦4	0.74	4	0.50×10^{0}	no	4.00 ± 4.03
3↦5	3.62	5	1.52×10^{-2}	yes	32.58 ± 32.62

Table 7. Statistical data (212 peak) for hydrothermal silica collected from the Gonzales Prospect in the Cerros de Amado area.

SAMPLE	SAMPLE #	n	MEAN	MEDIAN	σ_{n-1}	VARIANCE
91E21A	1	2	268.5	268.5	6.36	40.5
91E21C	2	5	316.6	298.0	34.42	1184.8

Table 8. Results from a t-test (two-tailed) performed on hydrothermal silica from the Gonzales Prospect.

PAIR	T	DEGREES OF FREEDOM	p	MEANS SIGN. DIFFERENT	CONFIDENCE LIMIT
1↔2	1.86	5	0.12	no	48.1 ± 48.1

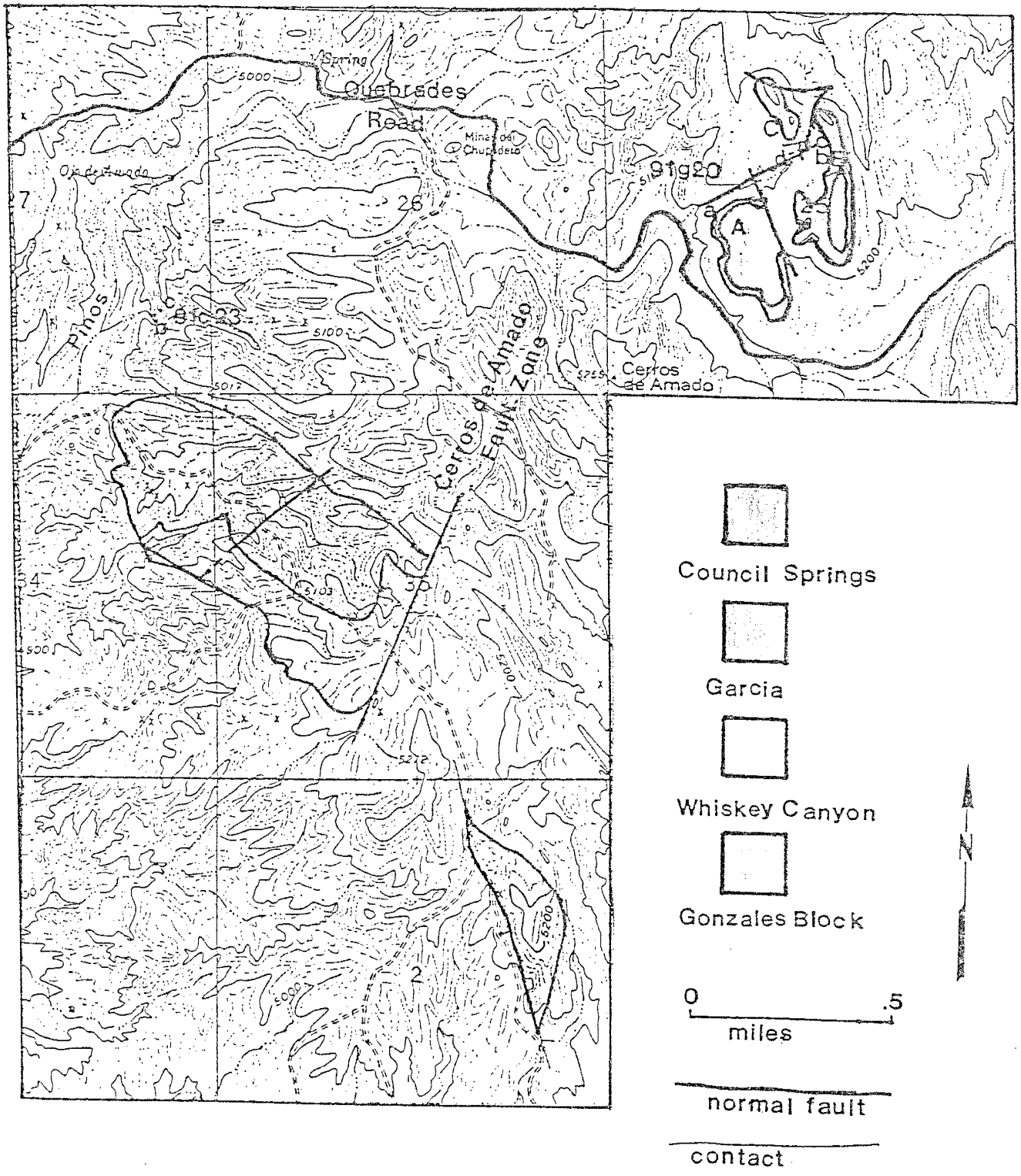

Figure 30. Map of the Cerros de Amado area showing sample locations (Geology after Rejas (1965)).

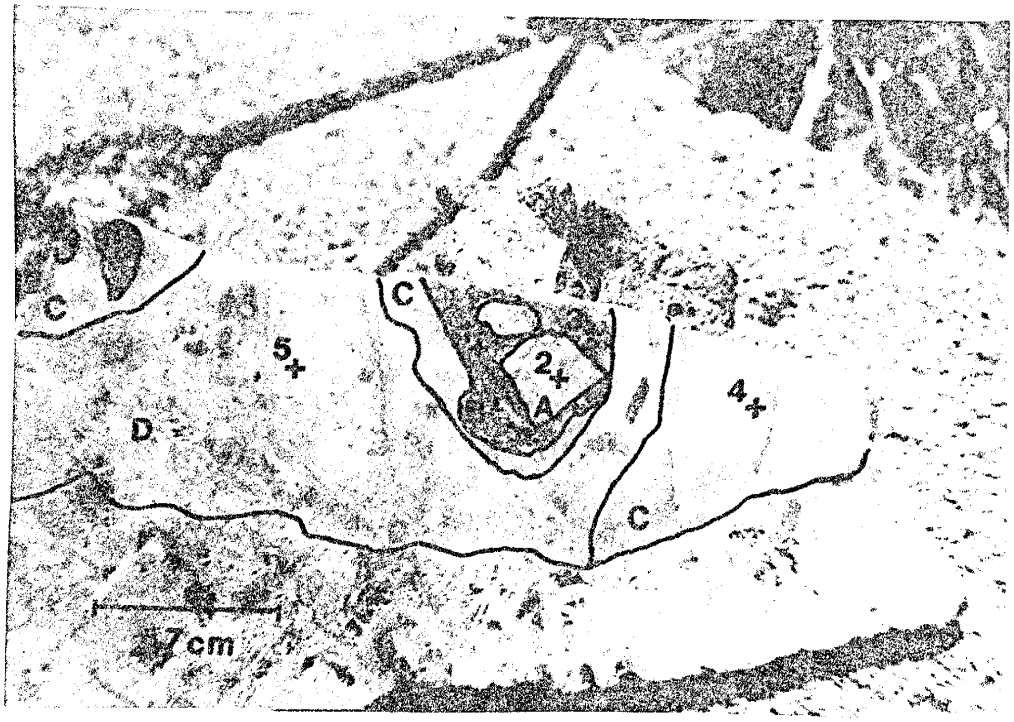

Figure 31. Photograph of slab cut from sample 91e21c showing stages of brecciation (A - earliest to D - latest) and location of cores (labelled 1-5). Bar is 1.7 cm long.

Area south of Arroyo de las Cañas

Detailed mapping of the area was first done by Fagrelius (1982) and is currently being updated by the writer. Within the area a near complete Permian section is exposed (see Fig. 29). Limestones asigned to the Pennsylvanian Madera Group (Fagrelius, 1982) crop out in the NW$\frac{1}{4}$ Sec. 17, NE$\frac{1}{4}$ Sec. 18, and the SW$\frac{1}{4}$ Sec. 7, T. 4 S., R. 2 E., of the San Antonio 7.5 min. quadrangle (Fig. 32). Which formation these limestones belong to is not known at this time; lithology suggests the Moya and Del Cuerto Formations. The Pennsylvanian section conformably underlies the Bursum Formation indicating that the top of the section is complete. There are two prominant lithologies: a thick upper carbonate sequence underlain by a thick clastic sequence. Based on measured thicknesses (Rejas, 1965), the carbonate sequence can be subdivided into the Moya and Del Cuerto, however a contact cannot be drawn without the identification of fusilinids. Because the Del Cuerto contains a relatively small amount of basal clastics (5 m; Rejas, 1965) a contact can be drawn at the base of the last limestone unit.

The structure of this area is very complex. High-angle normal faults can be divided into three categories based on orientation (Smith, 1983): (1) N-S trending, (2) NE trending, and (3) NW trending; low-angle faulting also occurrs (see Fig. 32). Chert was found in the Moya and Del Cuerto Formations of Pennsylvanian age and the Permian San Andres Limestone.

Madera Limestone

Samples from the basal limestone of the Del Cuerto Formation were taken from a single bed along a N–S traverse (location A, Fig. 32); this bed is cut by a high-angle group three normal fault at the southern terminus . Here the chert occurrs as lenses and nodules (Fig. 33), in some cases the nodules appear to have formed from a puddle of silica (Fig. 34).

San Andres Formation

The area were the formation was sampled (Fig. 32) is a block bounded by a high-angle fault on the west, a low-angle normal fault on the southeast, and the remaining block rests allochthonously on Torres Limestone of the Yeso Formation. Due to the high permiability of the San Andres it may have been affected by fluids migrating along these faults. Nodular chert (Fig. 35) found near a fault has a grainy texture while further away it is typically microcrystalline and shows a peculiar banding (Figs. 36 & 37) which could indicate either formation from a puddle of silica or could simply be diffusion bands. Samples were collected near the base of the formation.

X-ray Analysis

Temperatures calculated for the 212 and the 104 peaks plus the composition of the sample are given in table 9; crystallite size can be found in Appendix A. The [104] temperatures are not included in the discussion or statistical analysis of tables 10 – 12 for the same reasons mentioned in the previous section. The statistical parameters presented are also the same as previously mentioned.

The mean temperatures were compared using a student t-test (two-tested) with the results listed in table 12. As usual, all but one of the pairs is not significantly different. The observed differences can be interpreted as an accident of sampling.

Table 9. Temperatures (°C) of sedimentary chert in the area south of Arroyo de las Cañas.

SAMPLE	T_{212}	T_{104}	COMPOSITION [1]
Del Cuerto Member (Madera Fm.)			
91e24a1	189	289	α-quartz
91e24c1	224	292	α-quartz, calcite
91e24c2	206	B.D.[2]	α-quartz
91e24d1	210	270	α-quartz, calcite
91e24d2	203	270	α-quartz
91e24e2	245	276	α-quartz, calcite
91e24e3	224	B.D.	α-quartz
91e24f1	231	289	α-quartz, calcite
91e24f3	206	276	α-quartz
91e24h1	206	B.D.	α-quartz
91e24h2	203	258	α-quartz
91e24h3	203	290	α-quartz, calcite
San Andres Formation			
91f07b1	351	356	α-quartz
91f07b2	431	346	α-quartz
91f07b3	423	352	α-quartz
91f07b4	324	319	α-quartz
91f07c1	366	—	α-quartz
91f07c2	427	—	α-quartz
91f07c3	375	353	α-quartz
91f07c4	312	348	α-quartz

[1] X-ray diffraction, standard scan, 3° to 90° 2θ

[2] Bad Data

Table 10. Statistical data (212 peak) for Pennsylvanian cherts collected south of Arroyo de las Cañas.

SAMPLE	SAMPLE #	n	MEAN	MEDIAN	σ_{n-1}	VARIANCE
91E24A	6	1	—	—	—	—
91E24C	7	2	215.0	215.0	12.73	162.0
91E24D	8	2	206.5	206.5	5.00	24.50
91E24E	9	2	234.5	234.5	14.85	220.5
91E24F	10	2	218.5	218.5	17.68	312.5
91E24H	11	3	204.0	203.0	1.73	3.00

Table 11. Statistical data (212 peak) for Permian San Andres cherts collected south of Arroyo de las Cañas.

SAMPLE	SAMPLE #	n	MEAN	MEDIAN	σ_{n-1}	VARIANCE
91F07B	12	4	382	387.0	53.0	2802
91F07C	13	4	370	370.5	47.1	2218

Table 12. Results from a t-test (two-tailed) performed on cherts south of Arroyo de las Cañas.

PAIR	T	DEGREES OF FREEDOM	p	MEANS SIGNI. DIFFERENT	CONFIDENCE LIMIT
7↦8	0.88	2	0.47	no	8.5 ± 8.5
7↦9	1.41	2	0.29	no	19.5 ± 19.5
7↦10	0.23	2	0.84	no	3.5 ± 3.54
7↦11	1.61	3	0.21	no	11 ± 11
8↦9	2.53	2	0.13	no	28 ± 28
8↦10	0.92	2	0.45	no	12 ± 11.9
8↦11	0.86	3	0.45	no	2.5 ± 2.5
9↦10	0.98	2	0.43	no	16 ± 16
9↦11	3.85	3	3.1×10^{-2}	yes	30.5 ± 30.5
12↦13	0.35	6	0.74	no	12.25 ± 12.4

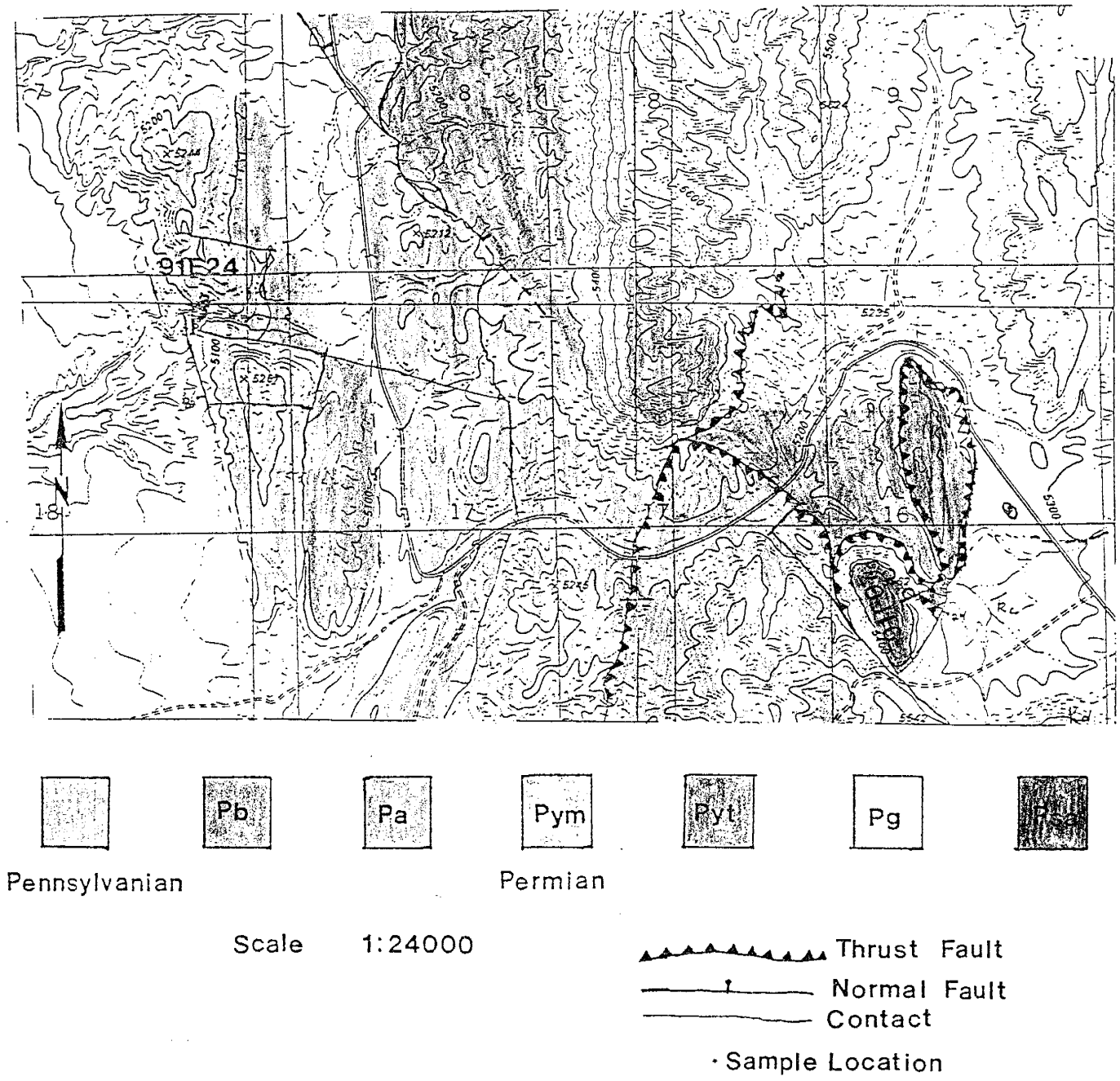

Figure 32. Map of area south of Arroyo de las Canas showing sample locations.

Figure 33. Photograph showing the occurrance of chert in the Madera Group, possibly Del Cuerto Member (Pennsylvanian). Hammer is approx. 15cm long.

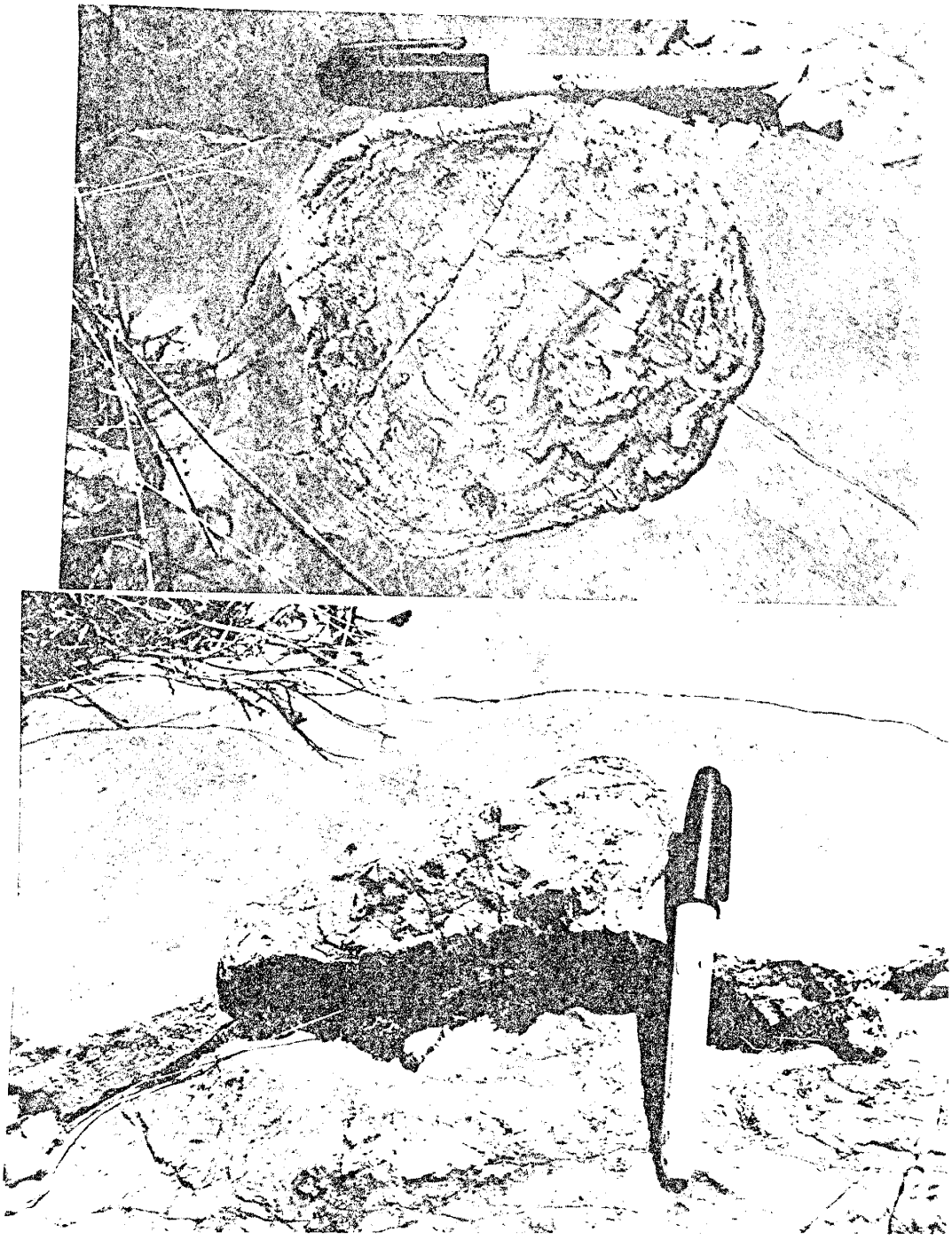

Figure 34. Photograph of chert nodule with concentric banding (a) and Cross-section (b).

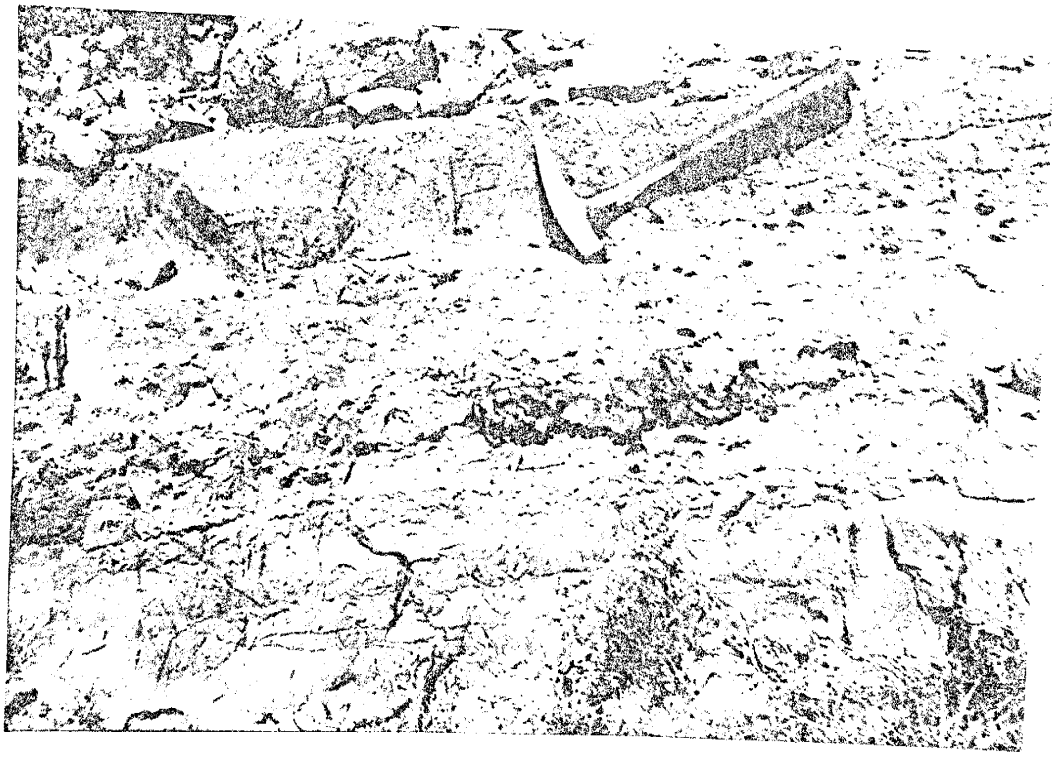

Figure 35. Photograph of nodular chert flattened in the plane of bedding (San Andres Formation).

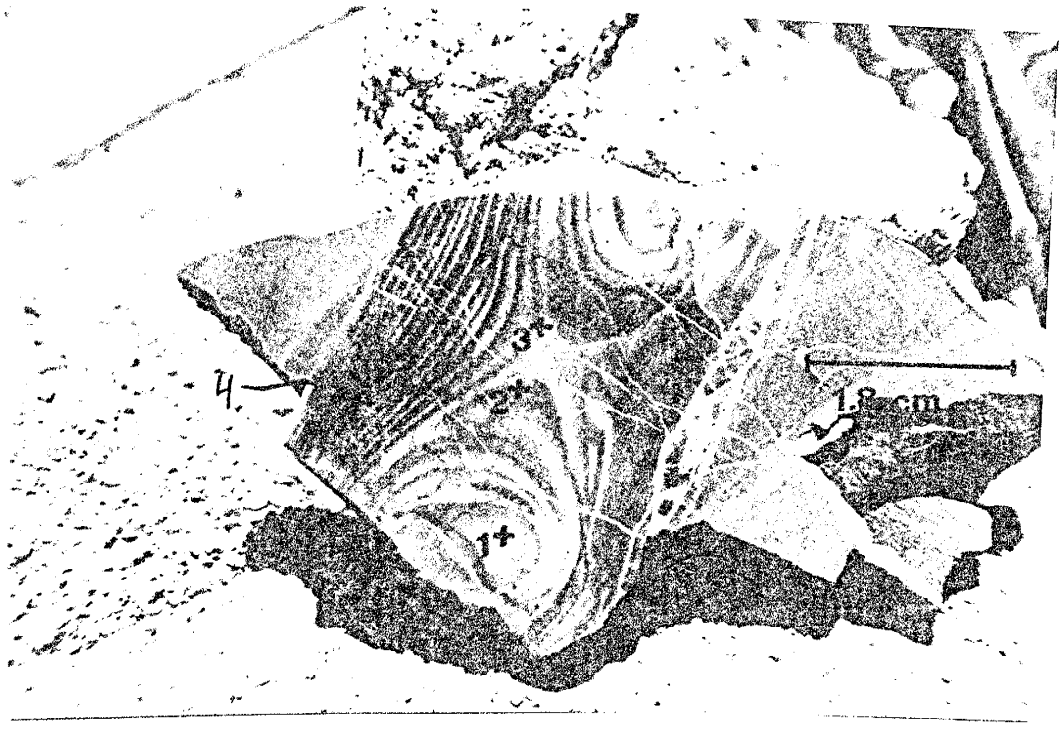

Figure 36. Photograph of a slab cut from sample 91f07b showing the banded structure. Also shown are core locations (labelled 1-4). Bar is 1.8 cm long.

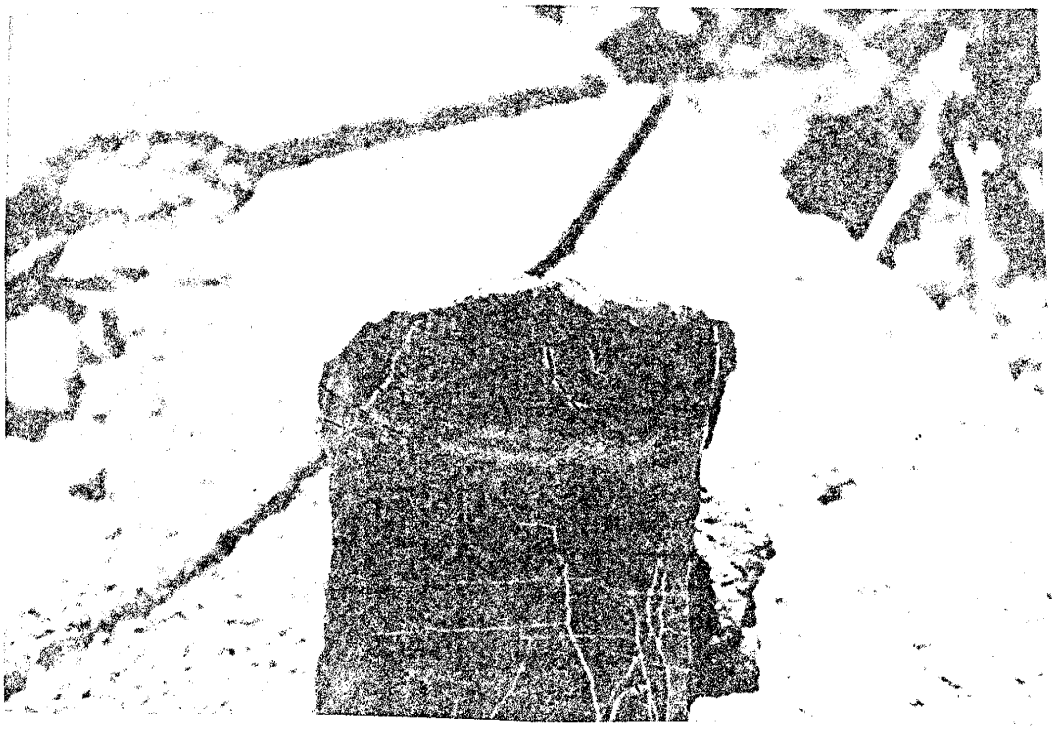

Figure 37. Photograph of slab cut from sample 91f07c showing the banded structure. Also shown are core locations (labelled 1-4). Bar is 1.3 cm long.

CHAPTER 4: Discussion

Paleogeothermal Gradient Determination

Before a geothermal gradient can be estimated the burial history of the Pennsylvanian section must be determined. A burial curve for the top of the Moya member of the Madera Formation is diagramatically illustrated in plate 1 and is based on formation thicknesses given in table 13 and the following geologic history.

Chert collected from limestones in the Cerros de Amado area and south of Arroyo de las Cañas were analyzed to determine burial temperatures. Temperatures calculated for the Pennsylvanian section, although possibly a little high, are consistant with the idea of increasing temperature with depth of burial. On the other hand, chert collected from Permian San Andres Formation give much higher temperatures than the Pennsylvanian Del Cuerto Formation. Because of the extensive faulting in the area, there is a high probability that these cherts were altered by hydrothermal solutions and therefore will not be used in this application. However, the origin of these samples deserves attention and will be discussed later.

Table 13. Maximum thickness of units in the Socorro region.

Formation	Thickness (km)	Symbol	Source
Tertiary			
Santa Fe Group	2.286	Tsf	1
La Jara Peak Basaltic Andesite	0.335	Tba	2
La Jencia Tuff	0.100	Tj	3
Hells Mesa Tuff	0.050	Thm	3
Datil Group	1.033	Td	4
Baca	0.315	Tb	2

Table 13. Cont.

Formation	Thickness (km)	Symbol	Source
Cretaceous			
Crevasse Canyon	0.024	Kcc	5
Gallup Sandstone	0.014	Kg	5
D-cross Tongue (Mancos)	0.117	Kmd	5
Tres Hermanos	0.071	Kth	5
Lower Shale Tongue (Mancos)	0.138	Kml	7
Dakota Sandstone	0.061	Kd	7
Triassic			
Chinle	0.165	c	6
Santa Rosa	0.072	s	6
Permian			
Bernal	0.030	Pb	6
San Andres	0.244	Psa	8
Glorieta	0.041	Pg	6
Yeso	0.442	Py	8
Abo	0.213	Pa	8
Bursum	0.053	Pbu	8
Pennsylvanian			
Moya	0.024	m	1
Del Cuerto	0.017	dc	1
Story	0.012	st	1
Burrego	0.026	b	1
Council Springs	0.006	c	1
Coan-Adobe	0.091	c-a	1
Amado	0.011	a	1
Bartolo	0.067	ba	1
Garcia	0.061	g	1
Whiskey Canyon	0.033	w	1
Elephant Butte	0.057	e	1
Sandia	0.177	s	1

1- Rejas (1965)
2- S. M. Cather (personal communication, 1991)
3- Measured in Joyita Hills
4- Cather and Chapin (1989)
5- Hook (1983)
6- Fagrelius (1982)
7- Tabet (1979)
8- R. M. Colpitts (personal comunication, 1991)

At the end of the Pennsylvanian the epeirec sea, from which platform carbonates of the Madera Foramtion were deposited, withdrew from the continent. During this regression, transitional units of the Permian Bursum Formation were conformably deposited on top of the Madera Formation. Continental deposits of the Abo formation and Maseta Blanca Member of the Yeso Formation rest conformably on top of the Bursum Formation. Deposition of the remaining Yeso Formation marks the beginning of the Permian transgression (Cabezas, 1991). The Glorieta Formation conformably overlies the Yeso Formation and represents a beach sand. Deposition of the San Andres Limestone occured at the maximum extent of the transgression, after which the sea withdrew. This regression is documented by a karst surface on top of the San Andres (Cabezas, 1991).

After deposition of the upper Permain Bernal Formation the area experienced a short hiatus of non deposition and erosion during the lower and middle Triassic. The upper Triassic is represented by the continental clastic deposits of the Santa Rosa and Chinle Formations (Fig. 38). During this hiatus it is not known how much material was eroded but at least 30 m of the Bernal Formation persisted into the lower Triassic (Fagrellius, 1982).

After a long hiatus of erosion and peneplanation (Cabezas, 1991), New Mexico was invaded one last time by an epicontinental sea. This transgression resulted in deposition of upper Cretaceous Dakota Sandstone to the D-Cross Tongue of the Mancos Shale. Onset of Gallup deposition marks the final withdraw of the epicontintal sea.

With the close of the Cretaceous comes the beginning of Laramide deformation. The Laramide Orogeny occurred about 80 to 40 m.y. ago and resulted in the creation of numerous basins and uplifts in the western North American foreland (Cather and Johnson, 1984). The distribution of these basins and uplifts in western New Mexico are shown in figure 39. Although the exact sequence of events are obscurred by later rift tectonism, it can be inferred from sedimentological evidence (Cather and Johnson, 1984) that uplift was occurring west of the Loma de las Cañas region (Sierra Uplift, Fig. 39). Emplacement of the large allochthons

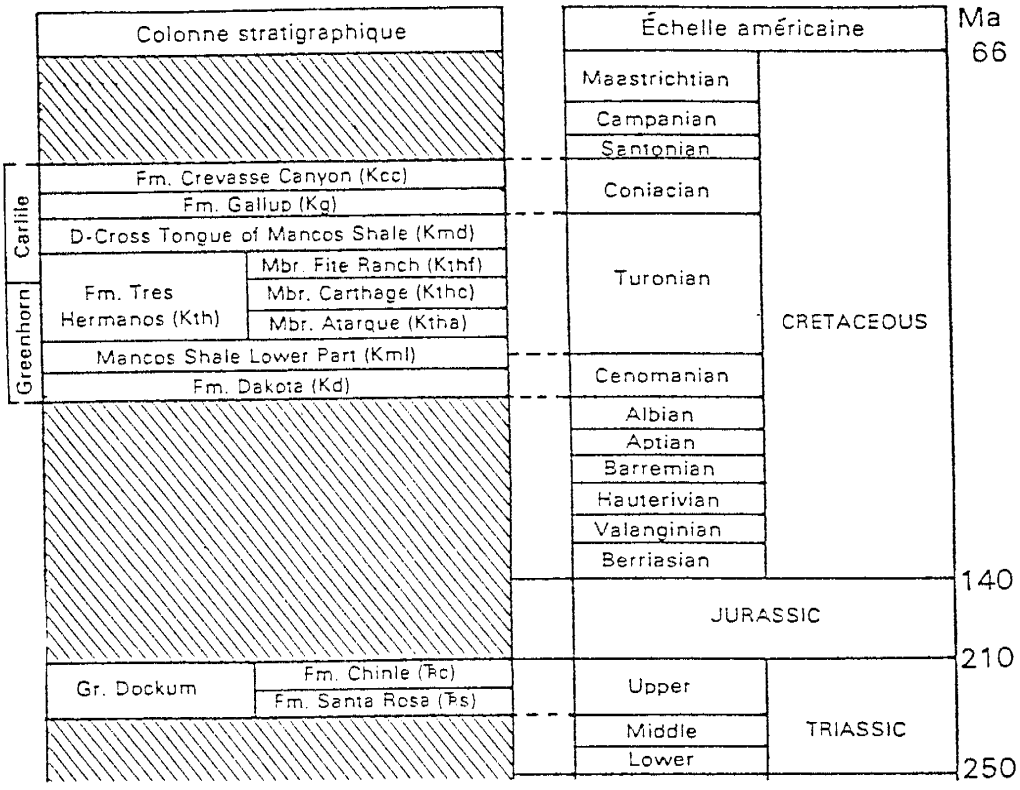

Figure 38. Mesozoic stratigraphic chart for the Socorro region (after Cabezas, 1991).

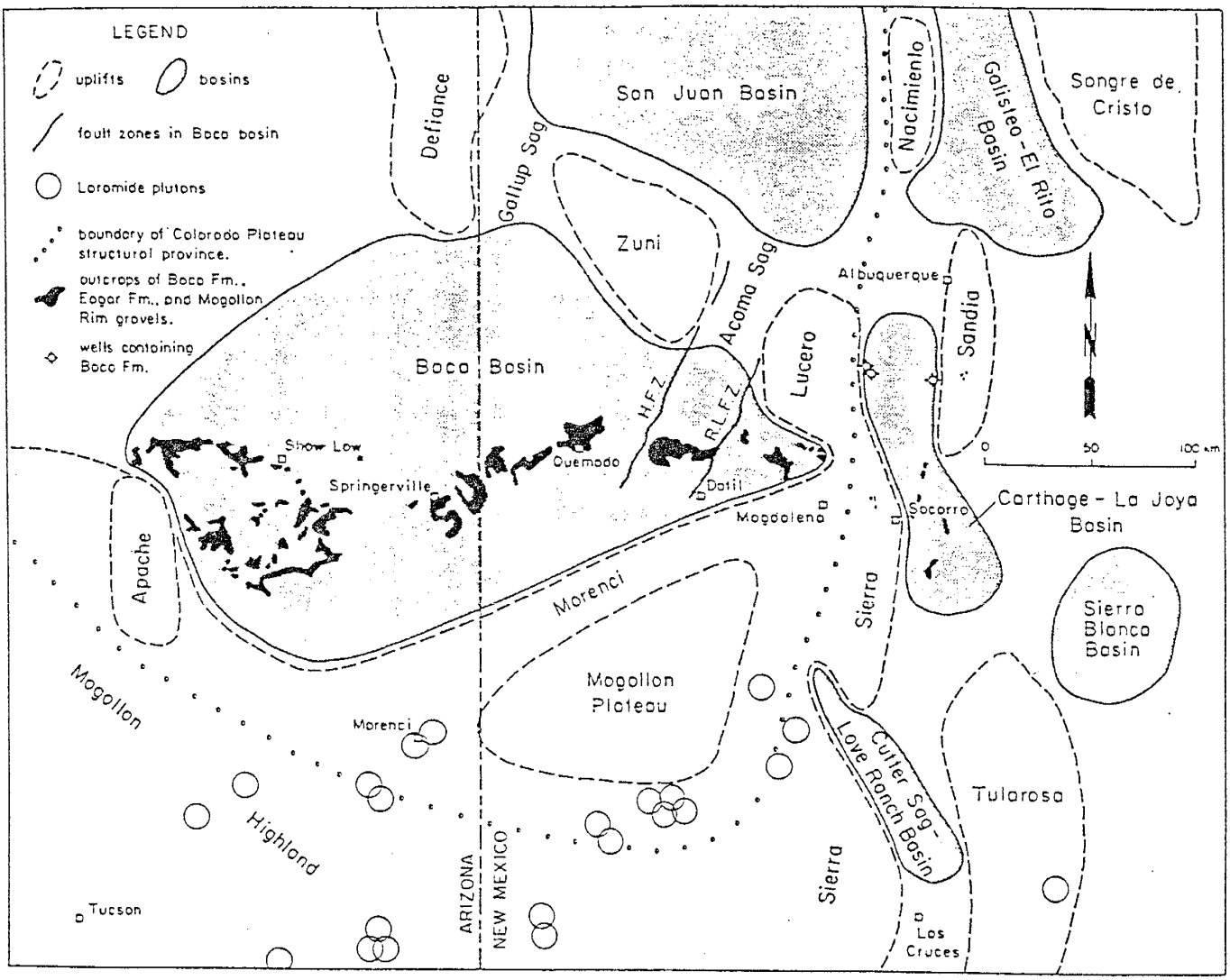

Figure 39. Map showing distribution of Eocene uplifts and basins in western New Mexico and Eastern Arizona (after Cather and Johnson, 1984).

is believed to have occurred during the Paleocene Epoch (Linden, 1990). Detachment occurred within the Permian Yeso Formation resulting in the repetition of Permian Glorieta through Cretaceous Tres Hermanos Formations (about 662 m; Linden, 1990).

The Sierra Uplift reached its maximum elevation during the mid Eocene at about the same time maximum strain rates for the Laramide are recorded (Cather and Johnson, 1984). Erosion of the eastern side of this uplift provided the sediments (Baca Formation) deposited in the Carthage-La Joya basin (Fig. 39). The Baca Formation overlies erosional remanents of the Crevasse Canyon Formation in the Carthage area (Fig. 40) which suggests that either the relative position of this formation was not affected by uplifting or may have been buried by Santonian to Maastrichtian sediments and then uplifted to the surface during the late Paleocene and early Eocene.

Sedimentary and volcanic sequences related to the extension of the Rio Grande rift were deposited in the Loma de las Cañas region but due to erosion true thicknesses cannot be measured. For this reason, thicknesses for these units were obtained from locations elsewhere in Socorro County. It is possible that these thicknesses may be greater, or less, than what was deposited in the Loma de las Cañas area but no other course is open. Faulting associated with extension from late Miocene to early Pliocene established the modern geometry of the rift basins. Displacements along these faults can attain several thousand meters (Cabezas, 1991).

The temperatures calculated for each member of the Madera Formation were averaged and are listed in table 14. The means were compared using a studentt t-test (two-tailed) to determine if they are significantly different. The means between the Coan-Adobe and Council Springs, and Coan-Adobe and Del Cuerto are significantly different. The means between the Del Cuerto and Council Springs are not significantly different, however, the results from a one-way analysis of variance ("EPISTAT" spftware package) shows that the means from all three members are signficantly different. These mean temperatures were

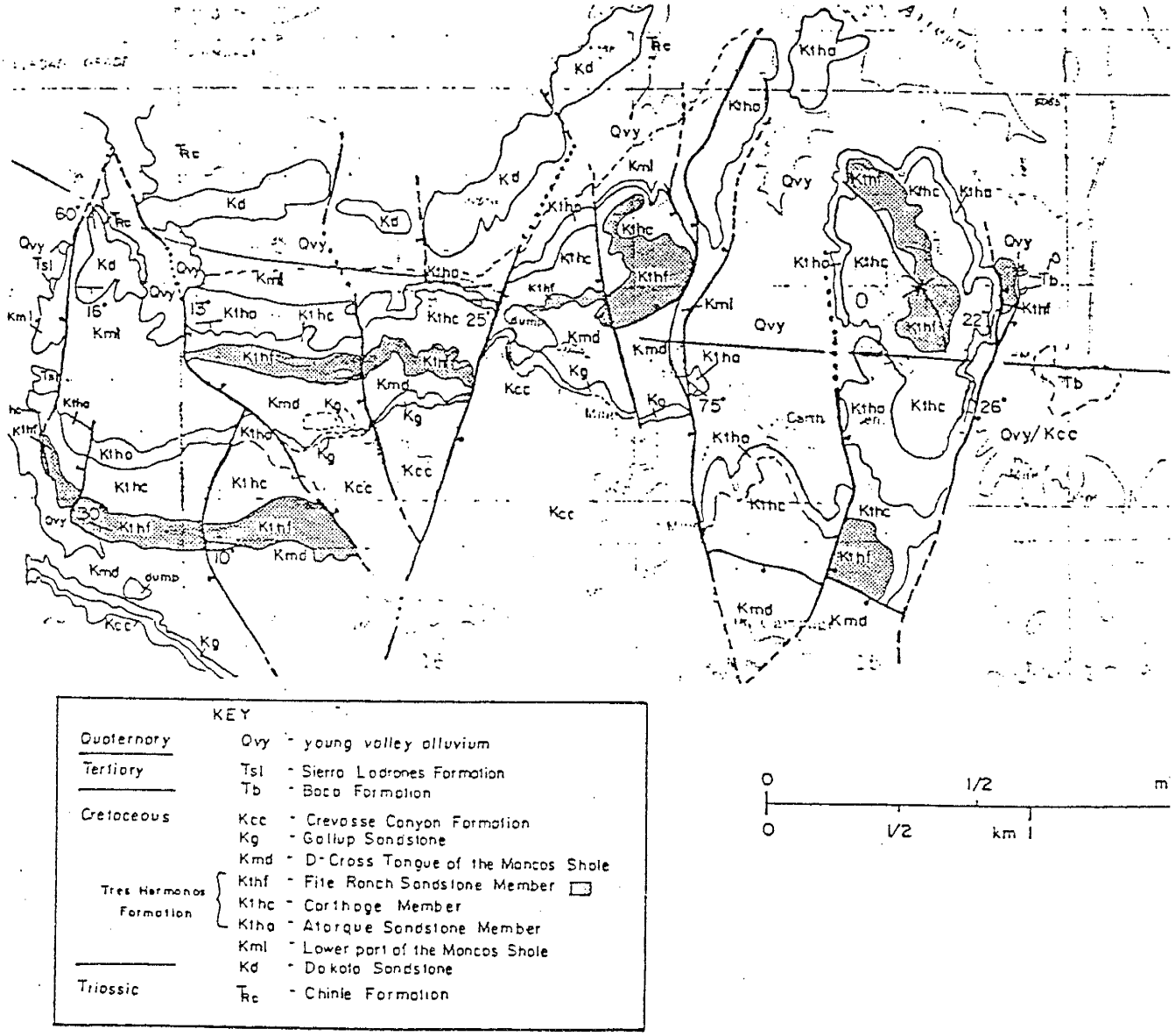

Figure 40. Geologic map of Cretaceous rocks along and south of U.S. 380 in the vicinity of Carthage, New Mexico (after Smith et. al., 1983).

plotted against burial depth (Fig. 41) using a maximum depth of 5812 meters (from Plate 1) for the top of the Pennsylvanian section and anchored at 20 °C (surface temperature). The resulting gradient is 34 $\pm$ 2.4 °C/km and represents a paleogeothermal gradient for the late Tertiary; crystallites record the maximum temperature and late Tertiary was the maximum burial depth.

Table 14. Statistical data for cherts collected from individual members of the Madera Formation.

FORMA.	FORMA. #	n	MEAN	MEDIAN	σ_{n-1}	VARIANCE
Coan-Adobe	1	4	257.5	259.0	8.23	67.67
Council Springs	2	10	211.9	205.5	18.43	339.66
Del Cuerto	3	12	212.5	206.0	15.43	238.09

Table 15. Results from a t-test (two-tailed) performed on individual members of the Madera Formation.

PAIR	T	DEGREES OF FREEDOM	p	MEANS SIGNI. DIFFERENT	CONFIDENCE LIMIT
1$\mapsto$2	4.68	12	5.36×10^{-4}	yes	45.6 $\pm$ 45.63
1$\mapsto$3	5.49	14	7.95×10^{-5}	yes	45 $\pm$ 45
2$\mapsto$3	0.08	20	0.93	no	0.6 $\pm$ 0.58

Gonzales Prospect

If each stage of brecciation in 91e21c (Fig. 31) was cemented at progressively shallower depths (upward motion along the fault) then a decrease in temperature from the first stage to the last stage might be recorded, presuming the offset during subsequent motion along the fault was enough to significantly alter temperatures. Of the five subsamples from 91e21c

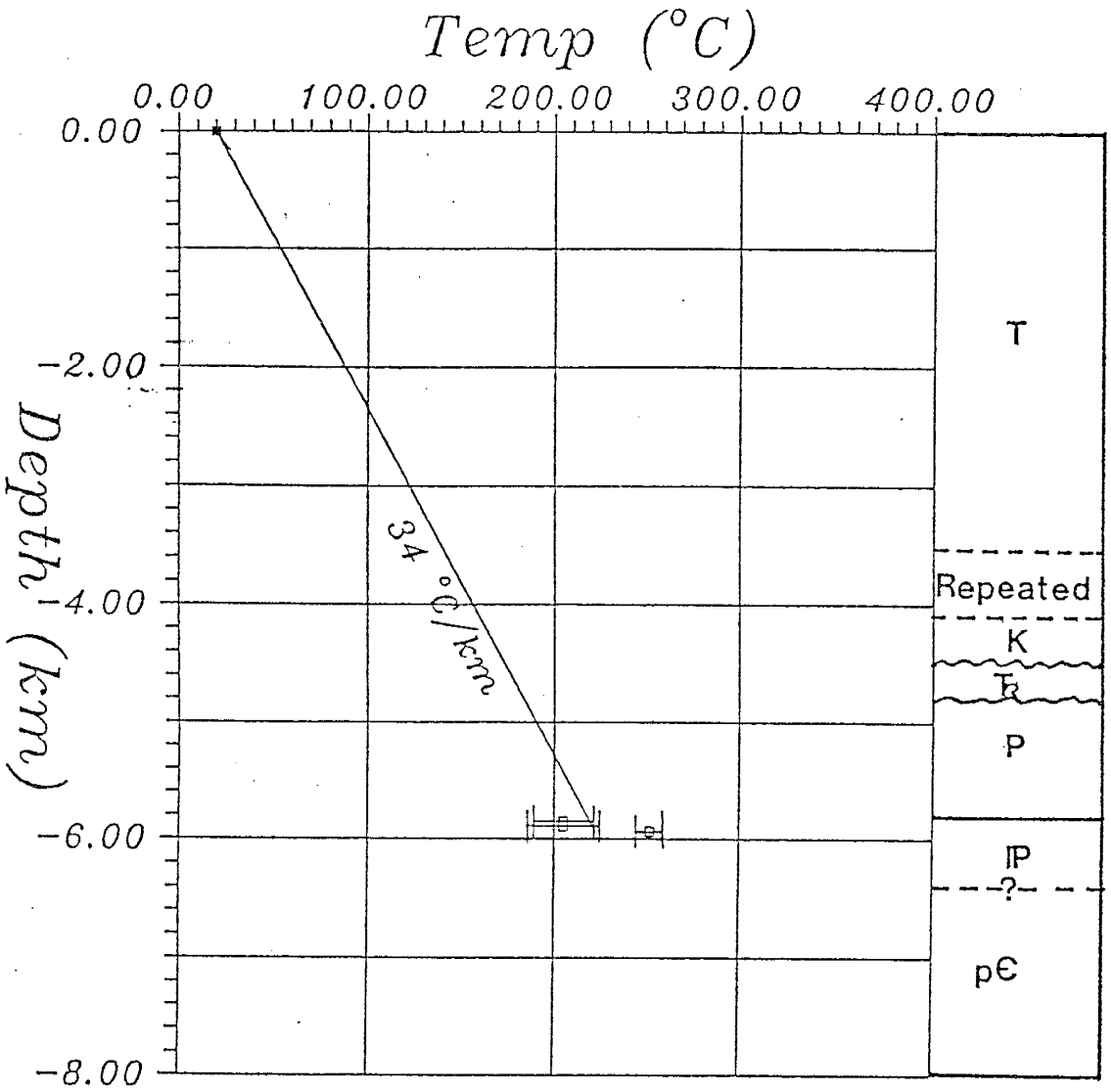

Figure 41. Plot of burial depth vs. temperature based on burial history in plate 1. Open squares and solid line represent [212] data.

(Fig. 31), two were taken from stage B because of the presence of a minute amount of chalcedonic silica (subsample 1; Fig. 31). However, the chalcedony only constituted approximately 25% of the subsample. The chalcedonic silica was still utilized but because of the small amount it had to be combined with the second type of silica present. Combination of the two types might be responsible for the temperature discrepency between subsamples 1 & 3 (Table 4) and will not be considered. Temperatures calculated from the 212 peak (Table 4) were plotted against the stage of brecciation and are shown in figure 42. The T_{212} of 91e21c2 is definitely out of sequence but this can be explained by contamination. The low temperature of this sample is close to that of 91e21c5 which suggests that the sample could have contained veins or vugs of material precipitated by fluids from which stage D was precipitated.

Two subsamples from 91e21a were analyzed. Temperatures calculated from the 212 peak are lower than those for 91e21c but the difference is not significant and probably both samples experienced the same thermal pulse. This is supported by the fact that the mineralization has not been brecciated which means that the plumbing for the entire system had to be in place prior to mineralization (W. X. Chavez, personal communication, 1991) which occured at about 45 Ma (the age of the fluorite was determined by Vicky Harden to be 44 Ma, W. X. Chavez, personal communication, 1991).

San Andres Formation

The peculiar banding of samples from the San Andres Formation indicate that either precipitation occurred from a puddle of silica or that they are simply diffusion bands. Thin section analysis of sample 91f07b shows a jigsaw puzzel texture (Iovenitti, 1977) which is continuous across the bands (banding isn't even apparent) indicating that these are diffusion bands rather than discrete boundries. Study of sample 91f07c shows the same, however, the area where subsample four was cored is coarser than the rest of the sample. The break

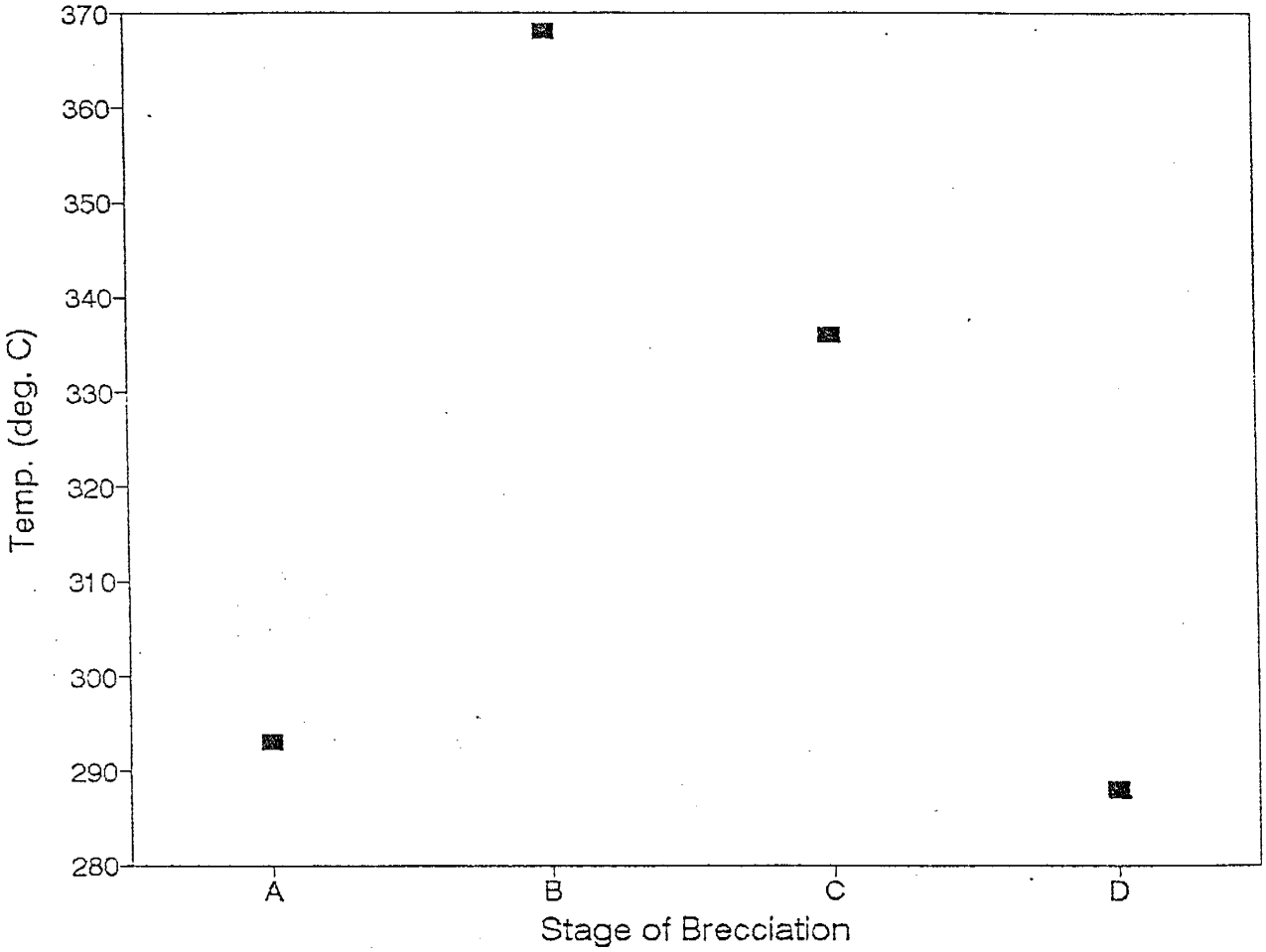

Figure 42. Stage of brecciation vs temperature for 91e21c showing a general trend of decreasing temperature with time.

between the two textures is a broad zone which doesn't reveal much about the transition. This texture contrast indicates that the area where 91f07c4 was obtained precipitated at a later time. This can also be concluded from the way this area truncates the diffusion bands (Fig. 37).

Sample 91f07c is presumed to have formed in the same manner as 91f07b, however, this sample appears to have undergone redissolution. The layer where subsample 4 was taken (Fig. 37) truncates the banding. Temperatures calculated from the 212 peak were plotted against sample location (Fig. 37) and shown in figure 43. Temperatures from the 212 peak show that, except for 91f07c2, the temperature remained more or less constant. Sample 91f07b has two temperatures that are out of sequence (91f07b1 & 2). These samples were analyzed under a petrographic microscope. All of the samples contain 3 size fractions: $<< 2$ μm, 2 to 8 μm , and 20 to 30 μm. The larger fraction could have had a significant effect on the temperature. Sample 91f07c4 gives a much lower temperature indicating that it could have precipitated from a cooler solution or at a shallower depth.

The high temperatures obtained from both samples (Table 9) (much higher than the underlying Pennsylvanian chert) coupled with field observations suggest that these cherts may have been affected by one of the following: (1) hydrothermal alteration, (2) tectonic heating, or (3) thermal pulse related to dike emplacement (or other igneous body). Since there is no mineralization along any of the faults in the area, alteration by hydrothermal fluids can be ruled out. Although andesitic dikes are present in the area (Fagrelius, 1982) the distance of the sample location from the closest dike (0.65 miles) is too great to explain the high temperatures. This leaves tectonic heating, which can be accomplished by either folding or frictional heating along fault zones, or, in this area, probably both.

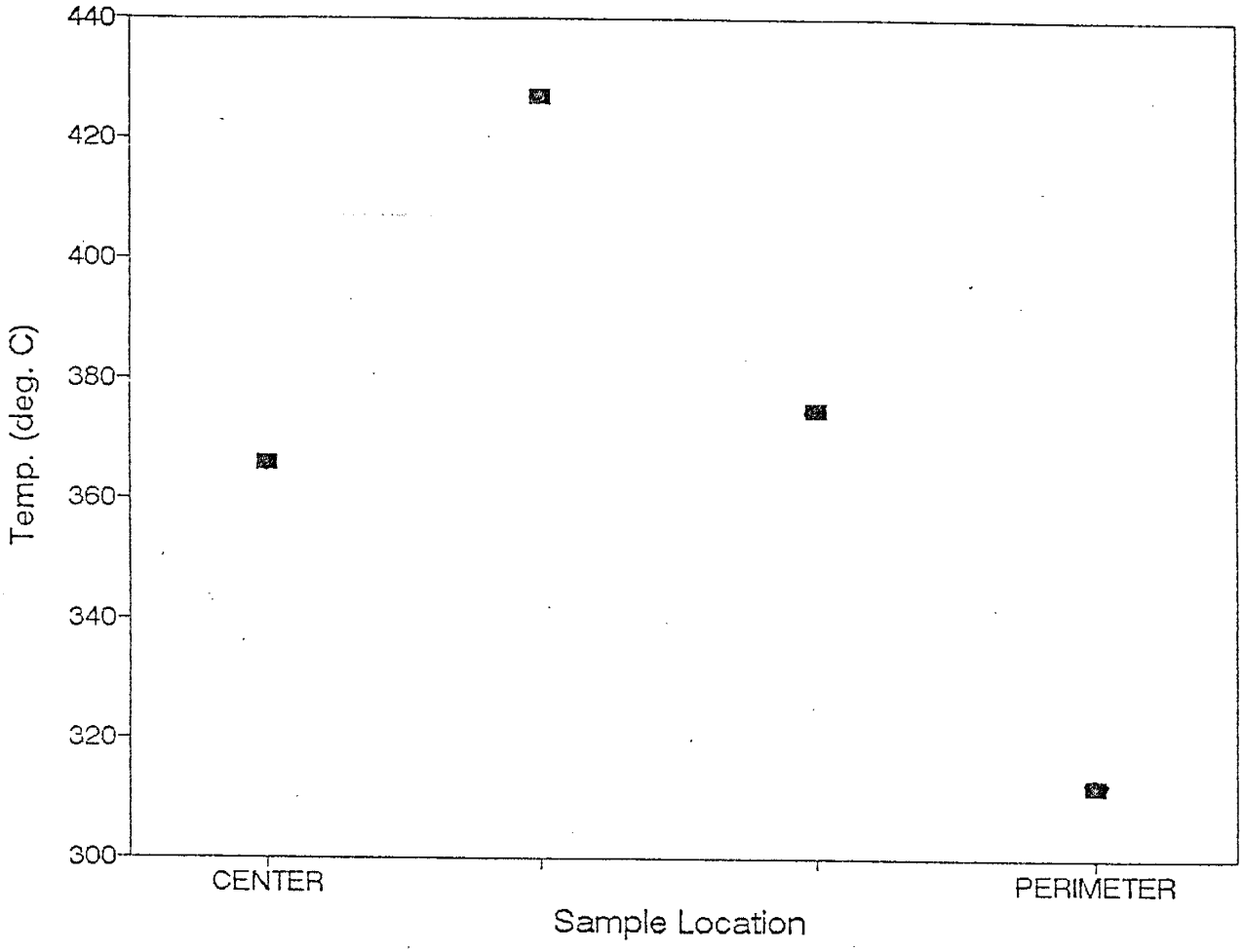

Figure 43. Sample location vs temperature for 91f07c. Filled squares represent [212] data. See text for discussion.

Permian Basin

Pieces of core from the Sun Oil # 3 well in Lea County near Carlsbad, New Mexico (Sec. 20, T25S, R37E) were obtained from the N M Bureau of Mines and Mineral Resources collection. Chert was sampled at depths of 2674 m (91e23a) and 2684 m (91e23b) (Devonian limestone). Slabs approximately 6.4 mm thick were cut and the remaining core returned. Three subsamples from each slab were cut and prepared for x-ray diffraction.

The average temperatures calculated from the 212 peak and other statistical data are given in table 16. The means of the samples were compared using a t-test and found not to be significantly different, so the two temperatures are treated as one: 202 $\pm$ 8.2 °C. The maximum thickness of the overburden in the area is 4.435 km (Grant and Foster,1989) giving a paleogeothermal gradient of 39.5 $\pm$ 2.6 °C/km.

Table 16. Statistical data (212 peak) for cherts from the Permian Basin, Carlsbad, New Mexico.

SAMPLE	n	Mean	Median	σ_{n-1}	Variance
91E23A	3	204.7	205	6.5	42.3
91E23B	3	199.3	202	10.3	105.3

CONCLUSION

Results from geothermometry on Pennsylvanian cherts give a gradient of 34 °C/km; this would be a paleogeothermal gradient for the late Tertiary since that was when the Pennsylvanian section reached its maximum burial depth. This gradient is also higher than the commonly cited gradient of 25 °C/km, which can be explained the level of tectonic activity in the area.

Results from the Gonzales Prospect show that precipitation of microcrystalline silica occurred during a single thermal episode. Analysis of the breccia found along the Gonzales fault zone shows a decrease in temperature with later stages of brecciation. However, the sample taken from the earliest stage is not consistant with the hypothesis presented. This sample gives a temperature in the vicinity of stage D, so it is possible that stage A may contain veins precipitated from stage D fluids.

Temperatures obtained from Permian cherts found in the San Andres Limestone are much higher than those obtained from Pennsylvanian cherts (by a factor of approximately 2). These cherts have obviously experienced a thermal event not related to burial. The fact that the temperatures are higher than those for hydrothermal silica from the Gonzales Prospect combined with the absence of mineralization along fault zones within the area is good evidence that these cherts were not altered by circulation of hydrothermal fluids. The thermal effects of igneous intrusions can also ce ruled out because of the distance between the sample location and nearest dike. These high temperatures have been explained by tectonic heating.

Temperatures from the Permian Basin basin give a paleothermal gradient very similar to the Loma de las Cañas region. This probably means that the rifting has had an affect on this area also. The gradient is much higher than the average of 23 °C (Schlumberger, 1989) which, if the temperatures are correct, corresponds to a depth of about 8 km. The

maximum possible overburden is only 4.5 km, so a high heat flow is indicated.

REFERENCES

Allaby, A. and M. Allaby, eds. 1990, The concise Oxford Dictionary of the Earth Sciences: New York, Oxford University Press, p. 340

Arkin, H. and R. R. Colton, 1971, Statistical Methods: New York, Barnes and Noble, Inc., p. 150 - 154

Bauch, J. H. A., 1982, Geology of the central area of the Loma de las Canas Quadrangle, Socorro County, New Mexico [MS thesis]: Socorro, New Mexico Institute of Mining and Technology, 115 pp.

Barroll, M. W. and M. Reiter, 1990, Analysis of the Socorro hydrothermal system: central New Mexico: Jour. Geoph. Res., v. 95, No. B13, p. 21,949 - 21,963.

Budding, A. J. and R. F. Broadhead, 1977, Igneous and metamorphic petrology of drill cuttings from the KCM No. 1 Forest Federal Well, Hidalgo County: New Mexico Bureau of Mines and Mineral Resources Circ. 152, p. 29 - 35.

Cabezas, P., 1991, The Southern Rocky Mountains in west-central New Mexico - Laramide structures and their impact on the Rio Grande rift extension: New Mexico Geology, v. 13, No. 2, p. 25 - 37.

Calvert, S. E., 1971, Composition and origin of North Atlantic deep sea cherts: Contri. Mineral. and Petrol., v. 33, p. 273 - 288

Cather, S. M. and B. D. Johnson, 1984, Eocene tectonics and depositional setting of west-central New Mexico and eastern Arizona: New Mexico Bureau of Mines and Mineral Resources, Circ. 192, 33 pp.

Cather, S. M. and C. E. Chapin, 1987, Day 2: Field guide to upper Eocene and lower Oligocene volcaniclastics rocks of the northern Mogollen-Datil volcanic field, in, Chapin, C. E. and J. Zidek, eds., Field excursions to volcanic terranes in the western United States, Volume I: Southern Rocky Mountain region: New Mexico Bureau of Mines and Mineral Resources Memoir 46, p. 60 - 68.

Chapin, C. E., 1971, The Rio Grande rift, Part I: Modifications and additions: New Mexico Geological Society, Guidebook 22, p. 191 - 201.

Colpitts, R. M. Jr., 1986, Geology of the Sierra de la Cruz area, Socorro County, New Mexico [MS thesis]: Socorro, New Mexico Institute of Mining and Technology, 141 pp.

Cullity, B. D., 1978, Elements of x-ray diffraction: Massachusetts, Addison-Wesely Publishing Company Inc., p. 3 - 31, 81 - 148, 188- 232.

Davis, J. C., 1986, Statistics and Data Analysis in geology: New York, John Wiley and Sons, p. 59 - 66.

Ernst, W. G. and S. E. Calvert, An experimental study of the recrystallization of porcelanite and its bearing on the origen of some bedded cherts: Amer. Jour. Science, v. 267-A, p. 114 - 133.

Ewing, R. C. and S. Thompson III, 1977, Thermal metamorphism of organic matter in drill cuttings from KCM No. 1 Forest Federal Well: New Mexico Bureau of Mines and Mineral Resources Circ. 152, p. 49 - 51.

Fagrelius, K. H., 1982, Geology of the Cerro del Viboro area, Socorro County, New Mexico [MS thesis]: Socorro, New Mexico Institute of Mining and Technology, 138 pp.

Folk, R. L., 1973, Evidence for peritidal deposition of Devonian Caballos Novaculite, Marathon Basin, Texas: Bull. Amer. Assoc. Petrol. Geologists, V. 57, p. 702 - 725

Folk, R. L. and E. F. McBride, 1976, The Caballos Novaculite revisited: Part I: origin of novaculite members: Jour. Sed. Pet., v. 46, p. 659 - 669

Grant, P. R., Jr. and Foster, R. W., 1989, Future petroleum provinces in New Mexico - discovering new resources: New Mexico Bureau of Mines and Mineral Resources, p. 5 - 22.

Grechin, V. I., K. A. Pisciotto, J. J. Mahoney and S. N. Gordeeva, 1980, Neogene siliceous sediments and rocks off southern California and Baja California, Deep Sea Drilling Project leg 63, in, Initial Reports of the Deep Sea Drilling Project, v. 63, Washington (U. S. Government Printing Office), p. 579 - 593

Heath, G. R. and R. Moberly, Jr., 1971, Cherts from the western Pacific, leg 7, Deep Sea Drilling Project, in, Winterer, E. L., et. al., eds, Initial Reports of the Deep Sea Drilling Project, v. 7, part 2, Washington (U. S. Government Printing Office) p. 991 - 1007

Heath, G. R., 1973, Cherts from the Eastern Pacific, leg 16, Deep Sea Drilling Project, in, Kaneps, A. G., ed., Initial Reports of the Deep Sea Drilling Project, v. 16, Washington (U. S. Goverment Printing Office), p. 609 - 613

Hein, J. R., D. W. Scholl, J. A. Barron, M. G. Jones and J. Miller, 1978, Diagenesis of late Cenezoic diatomaceos deposits and formation of the bottom simulating reflector in the southern Bering Sea: Sedimentology, v. 25, p. 155 - 181.

Hesse, R., 1990a, Origin of chert: Diagenesis of biogenic siliceous sediments, in, McIlreath, I. A. and D. W. Morrow, eds., Diagenesis: Geoscience Canada Reprint Series 4, p. 227 - 251

Hesse, R., 1990b, Silica Diagenesis: Origin of inorganic and replacement cherts, in, McIlreath, I. A. and D. W. Morrow, eds., Diagenesis: Geoscience Canada Reprint Series 4, p. 253 - 275

Hoersch, A. L., 1981, Progressive metamorphism of the chert-bearing Durness Limestone in the Beinn and Dubhaich aureole, Isle of Skye, Scotland: A reexamination: Amer. Mineralogist, v. 66, p. 491 - 506.

Holdsworth, B. K. and B. M. Harker, 1975, Possible indicators of degree of radiolaria dissolution in calcareous sediments of the Ontong-Java Plateau, in, Andrews, J. E., G. Packham and J. Herring, eds., Initial Reports of the Deep Sea Drilling Project, v. 30, Washington (U. S. Government Printing Office), p.489 - 497

Hook, S. C., 1983, Stratigraphy, paleontology, depositional framework, and nomenclature of marine upper Cretaceous rocks, Socorro County, New Mexico, in, Chapin, C. E., ed., Socorro Region II: New Mexico Geological Society, Guidebook 34, p. 165 - 172

Iler, R. K., 1979, The chemistry of silica: Solubility, Polymerization, Colloid and Surface Properties, and Biochemestry: New York, John Wiley and Sons, p. 48.

Iovenitti, J., 1977, A reconnaissance study of jasperoid in the Kelly Limestone, Kelly Mining District, New Mexico [MS thesis]: Socorro, New Mexico Institute of Mining and Technology, 200 pp.

Isaacs, C. M., 1982, Influence of rock composition on kinetics of silica phase changes in the Monterey Formation, Santa Barbara area, California: Geology, V. 10, p. 304 - 308

Jenkyns, H. C., 1986, Pelagic environments, in, Reading, H. G., ed., Sedimentary environments and facies: Boston, Blackwell Scientific Publications, p. 343 - 397

Jenkyns, H. C. and E. L. Winterer, 1982, Palaeoceanography of Mesozoic ribbon radiolarites: Earth and Planetary Sci. Letters, v. 60, p. 351 - 375

Kastner, M., J. B. Keene and J. M. Gieskes, 1977, Diagenesis of siliceous oozes - I. Chemical controls on the rate of opal-A to opal-CT transformation - an experimental study: Geoch. et Cosmoch. Acta, v. 41, p. 1041 - 1059

Keene, J. B., 1975, Cherts and porcellanites from the North Pacific, DSDP leg 32, in, Gardner, J. V., ed., Initial Reports of the Deep Sea Drilling Project, v. 32, Washington (U. S. Government Printing Office), p. 429 - 507

Keller, W. D., C. G. Stone and A. L. Hoersch, 1985, Textures of Palaeozoic chert and novaculite in the Ouachita Mountains of Arkansas and Oklahoma and their geologic significance: Geol. Soc. Amer. Bull., v. 96, p. 1353 - 1363

Kelley, V. C., 1982, The right-relayed Rio Grande Rift, Taos to Hatch: New Mexico Geological Society, Guidebook 33, p. 147 - 151.

Kelts, K., 1976, Summary of chert occurrances from Line Islands sites 314, 315, 316 DSDP leg 33, in, Kaneps, A. G., ed., Initial Reports of the Deep Sea Drilling Project, v. 33, Washington (U. S. Government Printing Office), p. 855 - 865

Klein, C. and C. S. Hurlbut, Jr., 1985, Manual of Mineralogy (after J. D. Dana), 20th ed.: New York, John Wiley and Sons, p. 440.

Klug, H. P. and L. E. Alexander, 1974, X-ray diffraction procedures: New York, John Wiley and sons, 966 pp.

Kolodny, Y., A. Taraboulos and U. Frieslander, 1980, Participation of fresh water in chert diagenesis: Evidence from oxygen isotopes and boron -track mapping: Sedimentology, v. 27, p. 305 - 316

Krauskopf, K. B., 1959, The geochemistry of silica in sedimentary environments, in, Ireland, H. A., ed., Silica in sediments: S.E.P.M. Spec. Publ. 7, p. 4 - 19

Lancelot, Y., 1973, Chert and silica diagenesis in sediments from the Central Pacific, in, Roth, P. H. and J. R. Herring, eds., Initial Reports of the Deep Sea Drilling Project, v. 17, Washington (U. S. Government Printing Office), p. 377 - 405

Land, L. S., 1976, Early dissolution of sponge spicules from reef sediments, North Jamaica: Jour. Sed. Pet., v. 46, p. 967 - 969

Linden, R. M., 1990, Allochthonous Permian rocks in the Socorro Region, central New Mexico: A structural analysis of emplacement and deformation [Ph.D. dissertation]: Socorro, New Mexico Institute of Mining and Technology, 104 pp.

Loope, D. B. and D. K. Watkins, 1989, Pennsylvanian fossils replaced by red chert: early oxidation of pyritic precursors: Jour. Sed. Pet., v. 59, p. 375 - 386

Maliva, R. G. and R. Siever, 1989, Chertification histories of some Late Mesozoic and Middle Palaeozoic platform carbonates: Sedimentology, v. 36, p. 907 - 926

Maulsby, J., 1981, Geology of the Rancho de Lopez area east of Socorro County, New Mexico [MS thesis]: Socorro, New Mexico Institute of Mining and Technology, 85 pp.

McBride, E. F. and R. L. Folk, 1977, The Caballos Novaculite revisited: Part II: chert and shale members and synthesis: Jour. Sed. Pet., v. 47, p. 1261 - 1286

Meyers, W. J., 1977, Chertification in the Mississippian Lake Valley Formation, Sacramento Mountains, New Mexico: Sedimentology, V. 24, p. 75 - 105

Mizutani, S., 1975, Silica minerals in the early stages of diagenesis: Sedimentology, v. 15, p. 419 - 436

Mizutani, S., 1977, Progressive ordering of cristobolitic silica in the early stage of diagenesis: Contrib. Mineral. and Petrol., v. 61, p. 129 - 140

Osburn, G. R. and C. Lochman-Balk, 1983, Stratigraphic nomenclature chart, in, Chapin, C. E., ed, Socorro Region II: New Mexico Geological Society, Guidebook 34, p. 99.

Parker, S. P., chief ed., 1986, McGraw-Hill encyclopedia of the geological sciences, 2nd ed.: New York, McGraw-Hill Book Company, p. 604

Rejas, A., 1965, Geology of the Cerros de Amado area, Socorro County, New Mexico [MS thesis]: Socorro, New Mexico Institute of Mining and Technology, 128 pp.

Reiter, M. and M. W Barroll, 1990, High heat flow in the Jornada del Muerto: a region of crustal thinning in the Rio Grande rift without upper crustal extension: Tectonophysics, v. 174, p. 183 - 195.

Renault, J., 1980, Application of crystallite size variation in cherts to petroleum exploration: New Mexico Institute of Mining and Technology, Final Report for Grant NO. 78-3315, 22 pp.

Riech, V., 1979, Diagenesis of silica, zeolites, and phyllosilicates at sites 397 and 398, in, Laughter, F. H. and E. M. Fagerberg, eds., Initial Reports of the Deep Sea Drilling Project, v. 47, part 1, Washington (U. S. Government Printing Office), p. 741 - 759

Riech, V., 1981, Siliceous sediments from the Nauru Basin: Diagenetic alteration of biogenic opal and authigenesis of silica and silicates, in, Shambach, J. and L. N. Stout, eds., Initial Reports of the Deep Sea Drilling Project, v. 61, Washington (U. S. Government Printing Office), p. 523 - 531

Robertson, A. H. F., 1977, The origin and diagenesis of cherts from Cyprus: Sedimentology, v. 24, p. 11 - 30

Schlimberger, 1989, Log interpretation charts: Schlumberger Educational Services, p. 2

Smith, C. T., 1983, Structural problems along the east side of the Socorro constriction, Rio Grande rift, in, Chapin, C. E., ed., Socorro Region II: New Mexico Geological Society, Guidebook 34, p. 103 - 109.

Smith, C. T., G. R. Osburn, C. E. Chapin, J. C. Osburn, O. J. Anderson, S. D. Rosen, T. L. Eggleston, and S. M. Cather, 1983, Road Log from Socorro to Mesa del Yeso, Joyita Hills, Johnson Hill, Cerros de Amado, Loma de las Canas, Jornado del Muerto, Carthage, and return to Socorro, in, C. E. Chapin, ed, New Mexico Geological Society, Guidebook 34, p. 1 - 28.

Smith, C. T., R. M. Colpitts and W. Gage, 1991, Structural geology of the Gonzales Precambrian Block, east of Socorro, New Mexico: A new look [abs.]: NMGS Abstracts, v. ##, p. 16.

Stein, C. L. and R. J. Kirkpatrick, 1976, Experimental porcelanite recrystallization kinetics: A nucleation and growth model: Jour. Sed. Pet., v. 46, p. 430 - 435

Tabet, D. E., 1979, Geology of the Jornado del Muerto coal field, Socorro County, New Mexico: New Mexico Bureau of Mines and Mineral Resources Circ. 168, 19 pp.

Thompson, M. L., 1942, Pennsylvanian system in New Mexico: N. M. Bureau of Mines and Mineral Resources Bull. 17, 91 pp.

Wiedmann, K. E., J. Unnam, and R. K. Clark, 1987, Computer program for deconvoluting powder diffraction spectra: Powder Diffraction, v. 2, p. 137 - 145

Williams, L. A., G. A. Parks and D. A. Crerar, 1985, Silica diagenesis, I. Solubility controls: Jour. Sed. Pet., v. 55, p. 301 - 311

Williams, L. A. and D. A. Crerar, 1985, Silica diagenesis, II. General Mechanisms: Jour. Sed. Pet., v. 55, p. 312 - 321

von Rad, U., V. Riech and H. Rosch, 1977, Silica diagenesis in continental margin sediments off Northwest Africa, in, Gardner, J. and J. Herring, eds., Initial Reports of the Deep Sea Drilling Project, v. 41, Washington (U. S. Government Printing Office), p. 879 - 905

APPENDIX A: X-RAY DATA

Table A1. Summary of x-ray data for the 212 peak.

SAMPLE	FILE	B	β	TEMP. (°C)	SIZE (Å)
91c23b2	z02732	.1300	.0884	265	1204
91c23c1	z02733	.1375	.0976	255	1091
91c23c2	z02735	.1320	.0898	263	1186
91c23c3	z02736	.1425	.1055	247	1009
91e21a1	z03298	.1170	.0813	273	1310
91e21a3	z03299	.1230	.0886	264	1202
91e21c1	z03211	.1150	.0653	298	1628
91e21c2	z03212	.1170	.0677	293	1571
91e21c3	z03213	.0925	.0382	368	2785
91e21c4	z03214	.1005	.0479	336	2219
91e21c5	z03297	.1060	.0710	288	1500
91e23a1	z03037	.2150	.1860	198	572
91e23a2	z03038	.2025	.1723	205	617
91e23a3	z03039	.1890	.1575	211	675
91e23b1	z03040	.2080	.1783	202	596
91e23b2	z03041	.1985	.1680	208	633
91e23b3	z03042	.2365	.2092	188	508
91e24a1	z03000	.2365	.2063	189	515
91e24c1	z03001	.1965	.1626	224	786
91e24c2	z03002	.2000	.1665	206	639

Table A1. Cont.

SAMPLE	FILE	B	β	TEMP. (°C)	SIZE (Å)
91e24d1	z03003	.1925	.1582	210	672
91e24d2	z03004	.2055	.1725	203	616
91e24e1	z03005	.1015	.0537	326	1978 (xlln)
91e24e2	z03006	.1475	.1076	245	988
91e24e3	z03007	.1720	.1353	224	786
91e24f1	z03008	.1620	.1240	231	857
91e24f3	z03009	.1995	.1659	206	641
91e24h1	z03034	.1975	.1669	206	637
91e24h2	z03035	.2025	.1723	203	617
91e24h3	z03036	.2025	.1723	203	617
91f07b1	z03203	.0965	.0430	351	2470
91f07b2	z03204	.0825	.0258	431	4124
91f07b3	z03205	.0835	.0270	423	3933
91f07b4	z03206	.1045	.0527	324	2016
91f07c1	z03207	.0930	.0388	366	2742
91f07c2	z03208	.0830	.0264	427	4026
91f07c3	z03209	.0910	.0363	375	2927
91f07c4	z03210	.1090	.0581	308	1829
91g20d1	z03443	.1990	.1711	204	622
91g20d2	z03444	.2240	.1994	198	534
91g20d3	z03445	.2275	.2025	191	526

Table A1. Cont.

SAMPLE	FILE	B	β	TEMP. (°C)	SIZE (Å)
91g20e1	z03446	.1985	.1707	204	624
91g20e2	z03447	.1920	.1651	207	645
91g20e3	z03448	.2200	.1936	194	550
91g20f1	z03199	.1510	.1074	245	990
91g20f2	z03200	.1943	.1563	211	680
91g20f3	z03201	.1673	.1260	230	844
91g20f4	z03202	.1620	.1200	235	886

Table A2. Summary of x-ray data for the 104 peak.

SAMPLE	FILE	β	TEMP (°C)	SIZE (Å)	COMMENTS
91c23b2	z02788	.108	352	1022	
91c23c1	z02727	.111	347	995	Bad Data
91c23c2	z02728	.042	575	2613	Bad Data
91c23c3	z02729	.137	312	802	
91e21a1	z03267	.126	326	874	
91e21a3	z03268	.125	327	880	
91e21c1	z03273	.102	363	1085	
91e21c2	z03274	.068	444	1618	
91e21c3	z03275	.108	351	1019	
91e21c4	z03276	.130	321	848	
91e21c5	z03281	.086	393	1274	
91e23a1	z03282	.145	—	—	Bad Data
91e23a2	z03283	.179	274	615	
91e23a4	z03284	.184	270	598	
91e23b1	z03286	.173	279	638	
91e23b2	z03287	.090	386	1229	
91e23b3	z03288	.135	—	—	Bad Data
91e24a1	z03060	.161	289	686	
91e24c1	z03061	.158	292	698	
91e24c2	z03063	.165	218	670	Bad Data
91e24d1	z03065	.185	270	597	
91e24d2	z03066	.185	270	597	

Table A2. Cont.

SAMPLE	FILE	β	TEMP. (°C)	SIZE (Å)	COMMENTS
91e24e1	z03067	.110	348	999	xlln qtz
91e24e2	z03068	.176	276	625	
91e24e3	z03069	.184	271	599	Bad Data
91e24f1	z03077	.161	289	684	
91e24f3	z03078	.176	276	625	
91e24h1	z03079	.145	228	758	Bad Data
91e24h2	z03080	.203	258	543	
91e24h3	z03099	.160	290	690	
91f07b1	z03228	.105	356	1048	
91f07b2	z03229	.112	346	985	
91f07b3	z03230	.108	352	1019	
91f07b4	z03231	.131	319	839	
91f07c3	z03261	.107	353	1026	
91f07c4	z03262	.110	348	1000	
91g20d1	z03400	.196	262	562	
91g20d2	z03407	.205	257	538	
91g20e1	z03408	.180	273	612	
91g20e2	z03409	.177	276	623	
91g20e3	z03410	.175	278	631	

Table **A2.** Cont.

SAMPLE	FILE	β	Temp. (°C)	SIZE (Å)	COMMENTS
91g20f1	z03263	.134	317	825	
91g20f2	z03264	.202	258	545	
91g20f3	z03265	.161	289	686	
91g20f4	z03266	.146	303	754	